Radiocarbon in an Earth System Model (CESM 2)

Master thesis
Faculty of Science, University of Bern

handed in by

Tobias Rolf Frischknecht

2020

Supervisor

Prof. Dr. F. Joos

Abstract

The distribution of radiocarbon in the Earth System provides insights into the processes and timescales governing the global carbon cycle. In this thesis, the capability of modeling carbon isotopes in the earth system is discussed. Results from isotope-enabled simulations with the Community Earth System Model (CESM2) are presented. I set up six simulations on the computer of the Swiss National Supercomputing Centre: a spin up, a control, and an industrial period simulations for both the data-driven land (CLM5) and ocean (POP) components of CESM2. The results for the preindustrial state, the industrial period, and the redistribution of bomb-produced radiocarbon are compared to observation-based estimates. The model is representing well the observation-based preindustrial surface distribution of radiocarbon in the ocean, but large model-to-observation differences are found in the deep ocean, in particular in the deep Pacific. The model underestimates the total bomb-produced radiocarbon inventory by 9% compared to estimates from ^{14}C production data. One of the main reasons identified for this underestimation is a slightly too slow gas exchange rate between the ocean and the atmosphere.

Contents

1 Introduction

1.1 Overview of the global carbon cycle

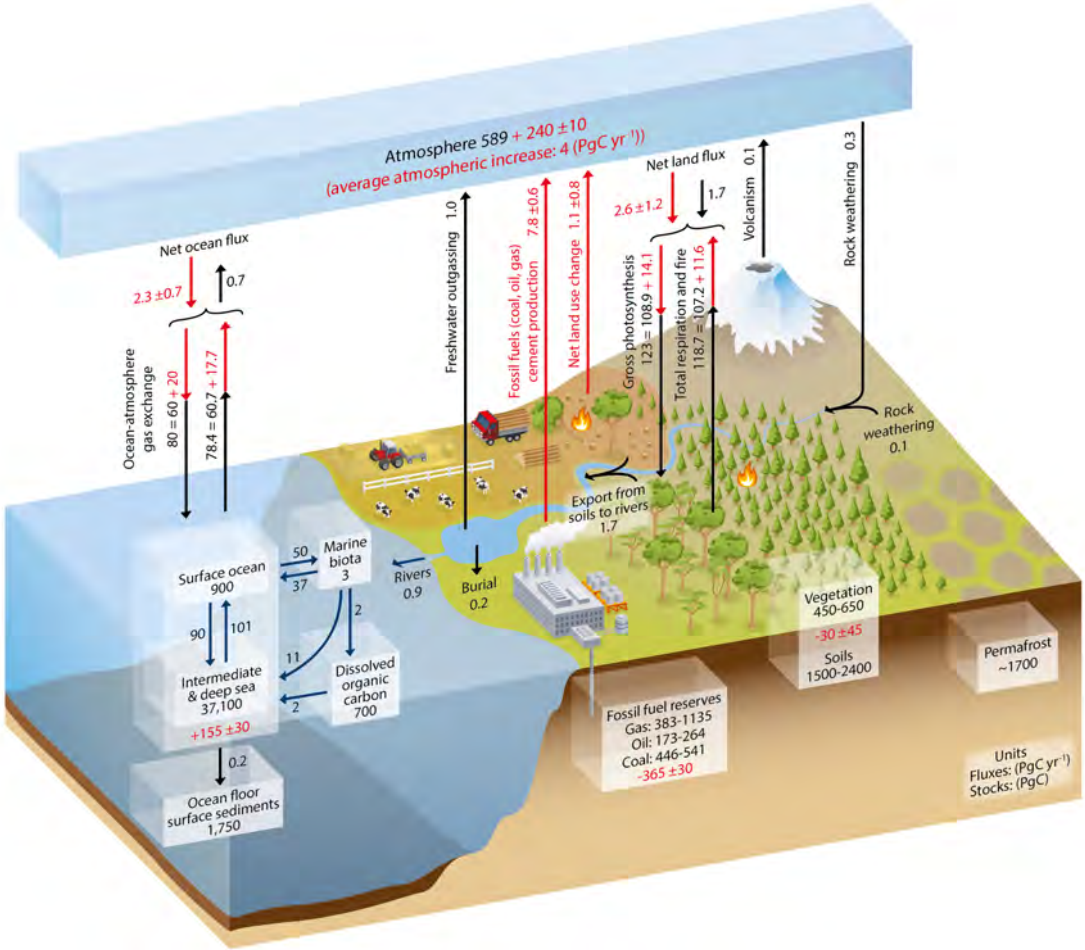

Figure 1: The major carbon reservoirs of the earth and exchange fluxes between them. Black numbers show preindustrial conditions, while red numbers indicate anthropogenic changes (Ciais et al. (2013)).

The carbon cycle describes the flow of carbon through the components of the earth system. Three major reservoirs contribute to the *fast*(<1000 yr) carbon cycle: the atmosphere, the ocean and the land biosphere. On longer timescales, the exchange fluxes with rocks and sediments also contribute to the carbon cycle. In the following, the preindustrial carbon cycle is discussed, before turning to the anthropogenic influence on the carbon cycle.

Figure 1 gives an overview of the carbon cycle. Of the ocean, atmosphere and land reservoir, the largest reservoir is the ocean. Roughly 38'000 PgC is stored in the ocean. Only a small part, of these 38 000, is stored in the living oceanic biota. Most of the carbon is stored in the form of dissolved inorganic carbon in the intermediate and deep ocean.

The land reservoir contains roughly 2000 PgC. In the land vegetation 450 - 600 PgC are stored. Most vegetation is located in the northern hemisphere. About 1500 to 2400 PgC is stored as organic matter in soils. In addition to the land vegetation and soil carbon, roughly 1700 PgC is stored in permafrost.

The atmosphere, the smallest of the fast exchanging reservoirs stores roughly the same amount as the land vegetation, about 600 PgC. In the atmosphere the CO_2 content is often given in units ppm (parts per million 1 ppm = 2.12 PgC).

At the preindustrial state, the fluxes between the three fast reservoirs were approximately balanced, as indicated by the near-constant CO_2 concentrations in ice cores. The largest global

gross fluxes (about 100 PgC yr^{-1}) are found between the land and the atmosphere. The flux between the land and the atmosphere is dominated by photosynthesis and plant respiration. As a result of the flux being dominated by photosynthesis, it is highly seasonal. In the winter season, there is almost no photosynthesis, while respiration continues. This leads to seasonality in the atmospheric CO_2 content. The amplitude of this seasonality is larger in the northern hemisphere than in the southern hemisphere.

Atmosphere - ocean flux through the gas exchange is the second-largest global exchange flux between reservoirs. The global gross exchange was roughly 60 PgC per year at preindustrial. The air-sea gas exchange is driven by the supersaturation or undersaturation of CO_2 in the ocean relative to the atmosphere, with the wind speed over the ocean determining how efficiently such a non-equilibrium is resolved (Sarmiento and Gruber (2006)).

Fluxes between the land and the ocean through rivers are very small, and on the bigger scheme not so relevant. At preindustrial, the net exchange fluxes between the three fast reservoirs and the slower sediment/rock reservoir were small. Atmospheric CO_2 was relatively constant over the last millennium, before the onset of the industrialization (Ciais et al. (2013)).

1.2 Anthropogenic perturbation

Human activities such as the burning of fossil fuels, cement production and land-use changes add an additional carbon flux into the cycle. Unlike the other exchange fluxes between the ocean, atmosphere and land, this carbon represents an "external" perturbation. The addition of fossil carbon into the system increases the carbon content of the atmosphere, ocean and land biosphere.

The major source of the carbon introduced to the cycle by human activity is the fossil fuel carbon reservoir. In total, roughly 365 PgC were released, over the whole industrial period until 2011. An additional source of anthropogenic carbon to the atmosphere is land-use change. It contributes another 180 PgC to the anthropogenic emissions until 2011.

These emissions accumulate in the reservoirs. Of the 545 PgC totally emitted through human activities, 240 PgC is in the atmosphere, 155 PgC is in the ocean and the rest is in the land biosphere (170 PgC). This means the atmosphere has taken up about 44% of the anthropogenic emissions. Over the industrial period, the net global change in the carbon inventory of the land biosphere is close to zero. The emissions caused by land-use and land-use changes were almost balanced through the carbon uptake elsewhere. The mechanisms driving the land biosphere carbon sink are not well understood, but CO_2 fertilization under raising atmospheric CO_2 likely contributed to stimulate plant growth (Ciais et al. (2013)).

Yearly emissions have been steadily rising since 1850. While land-use emissions remained roughly at the same level of 1.5 PgC per year since then, fossil fuel emissions rose from practically 0 in 1850 to 3 PgC per year in the 1960s to 9.5 PgC per year over the last decade (2009-2018) (Friedlingstein et al. (2019)) In 2018, around 11.5 PgC were emitted by fossil fuel emission and cement production (10 PgC) and land-use change (1.5 PgC). Of these 11.5 PgC, 5.1 PgC were stored in the atmosphere, 2.6 PgC in the ocean and 3.5 PgC in the land biosphere (Friedlingstein et al. (2019)). Note that these numbers are imbalanced due to a likely overestimation or underestimation of some sources or sinks.

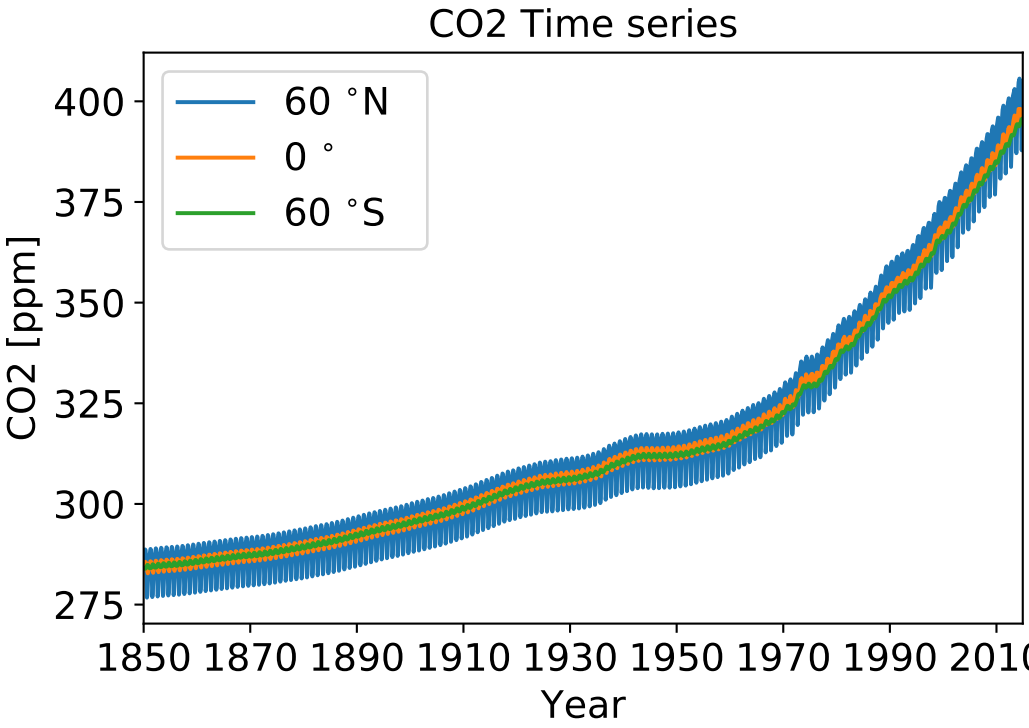

Figure 2: Atmospheric CO_2 history as compiled by Meinshausen et al. (2016). CO_2 mixing ratios are shown for three different latitudes. Seasonal variations are largest at high northern latitudes (blue).

For atmospheric CO_2, Meinshausen et al. (2016) compiled global time series from 1850 - 2015 (figure 2). Direct measurement of atmospheric CO_2 started in the 1950s, the data for the earlier periods are derived from ice core measurements. The CO_2 mixing ratio increased from 284 ppm in 1850 to over 400 ppm in the 2010s. The increase accelerates in the 1950s when atmospheric CO_2 levels were at 320 ppm. During the 100 year period from 1850 to 1950 CO_2 increased by 40 ppm only.

1.3 The marine carbon cycle

1.3.1 Air-sea gas exchange

The ocean and the atmosphere exchange gases through the air-sea interface. Net air-sea exchange is determined by how much the concentrations are in disequilibrium. Henry's law states that the equilibrium or saturation concentration of a substance A ($[A]_{sat}$) in water is linearly dependent on the partial pressure of A in the air(p^A) (Sarmiento and Gruber (2006)). The constant in that law is called the solubility. (S_A).

$$[A]_{sat} = S_A \cdot p^A \tag{1}$$

Solubility describes how much of a substance can be dissolved in water. Generally, solubility decreases with rising temperatures. Besides this temperature dependence, solubility also depends on the salinity of the ocean water and, even more importantly, on the gas considered. (Sarmiento and Gruber (2006))

Wherever the water is supersaturated or undersaturated, with respect to the equilibrium concentration with the atmosphere, net air-sea gas exchange occurs. The strength of this exchange is parameterized by the strength of the disequilibrium and a gas exchange velocity also called piston velocity. The net flux is calculated as:

$$F(\vec{x}, t) = PV(\vec{x}, t) \cdot (C_{sat}(\vec{x}, t) - C_{surface}(\vec{x}, t)) \tag{2}$$

Where F is the net flux, from the atmosphere into the ocean, PV is the piston velocity. C_{sat} is the saturation concentration of dissolved CO_2 in surface water for a given atmospheric partial pressure. C_{surf} is the concentration of dissolved CO_2 in surface water. (Jahn et al. (2015))

The gas exchange velocity or piston velocity is usually parameterized as a function of wind speed. As it encompasses many different process, the way to parameterize the piston velocity is not straight forward (Sarmiento and Gruber (2006)). One often used parametrization is the one given by Wanninkhof (1992):

$$PV = 0.251\text{cm h}^{-1} \cdot U^2 \cdot (Sc/660)^{-0.5} \tag{3}$$

PV being the piston velocity, U is the wind speed measured at 10m above sea level, and Sc is the gas-dependent Schmidt number. Note that the coefficient 0.251 cm h^{-1}, given here is from Wanninkhof (2014). Wanninkhof (1992) gave 0.31 cm h^{-1} which is now consider to be too high (Wanninkhof (2014)).

Other parameterizations exist. In some of these parameterizations, the functional form depends on the wind speed. Liss and Merlivat (1986) use a piece-wise linear function, with totally three different slopes. This approach reflects that at different wind speeds different processess dominate the air-sea gas exchange.

1.3.2 Dissolved inorganic carbon

Carbon is mostly stored in the form of dissolved inorganic carbon(DIC) in the ocean. DIC is the sum of the concentrations of dissolved CO_2, HCO_3^- (bicarbonate) and CO_3^{-2} (carbonate). CO_2 reacts with water to form H_2CO_3, but as this is hard to distinguish from dissolved CO_2, CO_2^* is introduced defined as:

$$[CO_2^*] = [CO_2] + [H_2CO_3] \tag{4}$$

The relative concentrations of the three species (CO_2^*, HCO_3^- and CO_3^{-2}) depend on the pH. At a typical seawater pH of 8 most (90 %) of the inorganic carbon is in the form of HCO_3^- (Schulte et al. (2011)).

1.3.3 Ocean circulation

Driven by winds and the rotation of the earth, a gyre circulation is induced into the top 500m of the world's oceans. Near the equator, the horizontal circulation diverges leading to upwelling in the equatorial regions, especially in the Atlantic and the Pacific Ocean. Additionally along the eastern coast of continents wind forcing causes strong upwelling. (Sarmiento and Gruber (2006))

The deep water circulation features two major deep water sources, one in the North Atlantic (called North Atlantic Deep water(NADW)) one in the Wendell Sea (called Antarctic Bottom Water (AABW)). (Sarmiento and Gruber (2006)). From the North Atlantic water flows southward, in the Southern Ocean where it mixes with the Southern Ocean deep water. The Indian and the Pacific Ocean are filled from the relatively well-mixed Southern Ocean water. The water flows along the ocean bottom and upwells into intermediate depth in the Indian and Pacific Ocean. (Sarmiento and Gruber (2006))

1.3.4 Marine biological cycle

Marine phytoplankton builds up the organic matter through photosynthesis. The photosynthesis needs light and dissolved carbon, most organisms also require many other nutrients. Light becomes a limiting factor for photosynthesis in the deeper ocean, constraining the photosynthesis roughly to the top 100m (Sarmiento and Gruber (2006)).

The organic matter in the ocean has almost fixed stoichiometric ratios between the nutrients C:N:P and the oxygen (O_2) released in the processes. The C:N:P:O_2 ratio is 106:16:1:-150, meaning organic matter contains 106 mols of carbon for every mol phosphorus. 150 mol of O_2 is released in the process of creating organic matter containing one mol of phosphorus. (Sarmiento and Gruber (2006))

In the upper ocean there exists a loop in which the organic matter is recycled by various organisms. Some of the organic matter sinks below the regions of this loop. (Sarmiento and Gruber (2006))

Remineralization is the process of breaking up organic compounds into their original constituents. The pool of dissolved organic carbon is correspondingly divided into dissolved organic matter (DOM) and particulate organic matter (POM). The main difference between the two is their respective size, this size difference leads to DOM being transported predominately by mixing

and circulation while particles in the POM pool are sinking gravitationally on its own. (Sarmiento and Gruber (2006)). For the loop to be closed, nutrients from the deep ocean are brought up to the surface by upwelling.

1.3.5 Distribution Of DIC and PO_4

DIC is not uniformly distributed in the ocean. There are horizontal and vertical gradients in the DIC concentrations. To assess the DIC distribution, the Global Ocean Data Analysis Project (GLODAP) gridded product by Key et al. (2004) is used.

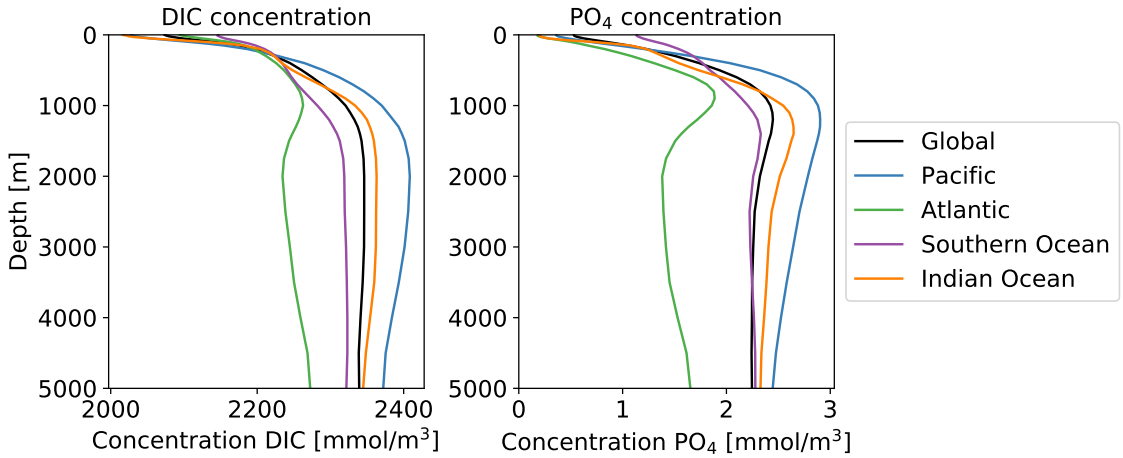

Figure 3: Observational DIC and PO_4 depth profiles (GLODAP Key et al. (2004))

The DIC concentration is lower at the surface than in the deep ocean. This is the result of the marine biological cycle (1.3.4). The formation of organic matter in the surface ocean utilizes DIC, therefore, reducing its concentration. Remineralization in the deeper ocean releases DIC into the ocean. The combination of the surface usage and deeper ocean release creates the surface to deep ocean gradient, seen in figure 3. The higher the gradient the more efficient the biological pump is (Sarmiento and Gruber (2006)).

Solubility and therefore gas exchange also influence the distribution. Gases are more soluble in cold water than in warm water (section 1.3.1). This would lead to CO_2 outgassing in the warm equatorial regions and ingassing in higher latitudes (Sarmiento and Gruber (2006)) in a uniformly distributed ocean. However, the southern ocean and some parts of the North Atlantic and Pacific still show outgassing (figure 5), this is likely due to strong upwelling, incomplete biological utilization and too weak cooling (Gloor et al. (2003)).

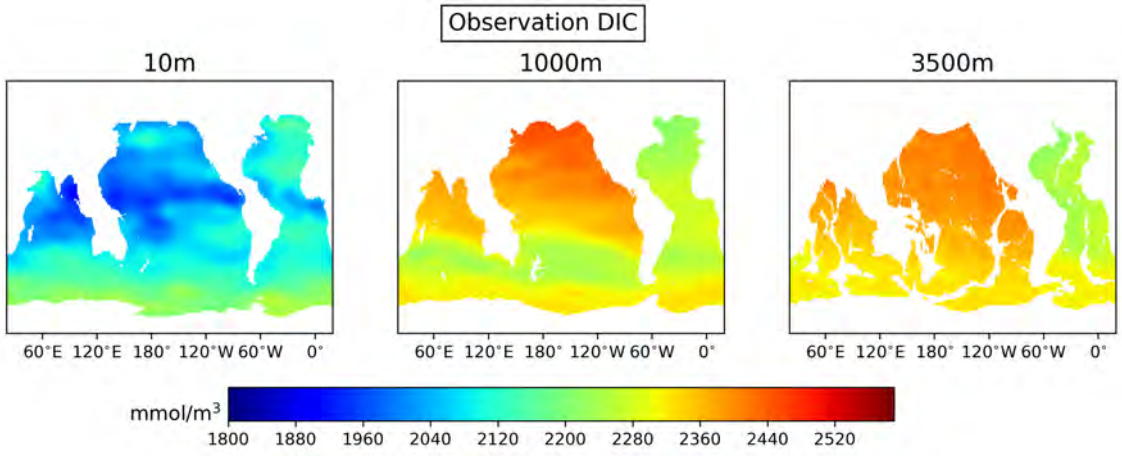

Figure 4: Observational DIC distribution of the world ocean (GLODAP Key et al. (2004))

DIC is only depleted by around 10%, relative to its mean oceanic concentration, at the surface.

DIC is typically not considered a limiting nutrient for biological growth. Other nutrients such as P are almost completely depleted at the surface and these are then considered limiting for further biological growth. Broecker et al. (1982) called nutrients such as P which are completely depleted at the surface *biolimiting*. Partially depleted nutrients are called *biointermediate*.

Besides this vertical gradient, there exist also horizontal gradients. These are induced by a combination of circulation effects and biological effects. Note that Sarmiento and Gruber (2006) mention that without biology P would be almost uniformly distributed.

Horizontally, DIC varies between 1800 mmol/m^3 and 2300 mmol/m^3 (see figure 4). Low values are found around the tropics and the subtropics but not around the equator. In the Southern Ocean, the Northern Atlantic, Northern Pacific and equatorial regions higher concentrations are found. The Southern Ocean and North Atlantic/Pacific have higher concentration because biology is not efficient enough due to iron and light limitation(Sarmiento and Gruber (2006)). While in equatorial regions upwelling brings DIC rich water back to the surface(Sarmiento and Gruber (2006)).

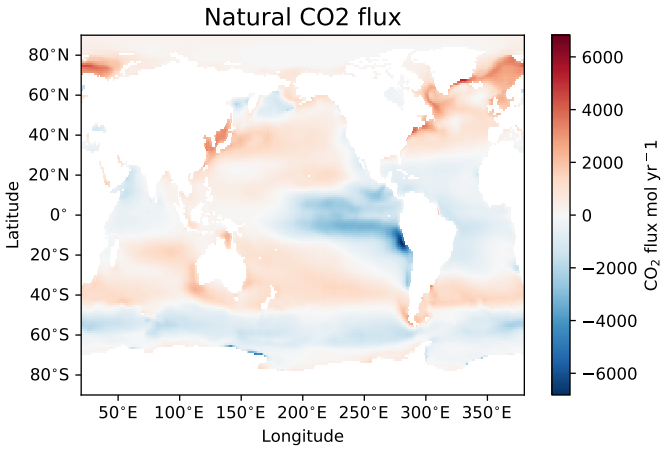

Figure 5: Natural modeled CO_2 flux, negative values indicate a flux into the ocean.

1.4 Motivation

The anthropogenic changes to the global carbon cycle and the resulting changes to the earth's climate pose a serious challenge. To assess the impact of further carbon emissions, it is important to know how much of the released carbon will stay in the atmosphere.

Understanding the cycling of the carbon isotopes can be a further tool to constrain the ocean uptake of anthropogenic carbon. With additional constraints, it should be possible to reduce model uncertainty. However, as a first step, it is necessary to develop and test model capabilities to simulate the global distribution of these carbon isotopes. If the models are not appropriately tested future predictions from such models will be less reliable.

Some work has already been done on this topic, for example by Naegler and Levin (2006), Jahn et al. (2015) and Dentith et al. (2019). Naegler and Levin (2006) used the GRACE model to assess, how much radiocarbon was produced by bomb tests in the 1950s and 60s, the so-called radiocarbon budget. Additionally, they looked at how this 'bomb' radiocarbon distributes to the different reservoirs. Jahn et al. (2015) implemented carbon isotopes into the ocean component of the CESM (Community Earth System Model). They tested how well their implementation represents the observed distributions of carbon isotopes in the ocean. Dentith et al. (2019) tested the implementation of the carbon isotopes in the FAMOUS GCM against radiocarbon data obtained from corals. With these coral data, they tested the ability of the FAMOUS GCM to represent the spatial and temporal evolution of the radiocarbon content in the ocean during the industrial period.

In this thesis, the CESM model with isotopes enabled is applied. While the work of Jahn et al. (2015) was limited to the ocean component, we will also analyze isotopes in the land component, although the main focus is on the ocean. Since the Jahn et al. (2015) paper the CESM model has evolved. Where appropriate, we will mention changes to the CESM model that made our results differ from theirs. We define now three questions that are relevant to this thesis:

- How well can the CESM model represent the distributions of carbon isotopes at preindustrial?
- Can the CESM model faithfully represent the radiocarbon uptake by the ocean during the industrial period?
- Can separately run ocean and land-only simulations be combined to reasonably represent the evolution of the total radiocarbon budget?

1.5 Outline

The outline of this thesis is as follows: Section 2 focus on the isotopes of carbon. The concept of isotopes and the most important differences between isotopes are explained. The isotopic notation is introduced, as well as the concept of fractionation, followed by a description of the natural cycle and distribution in the ocean of the carbon isotopes. The section ends with a brief discussion on the capabilities of using radiocarbon to determine the water age.

Section 3 gives a brief description of the CESM, and explanations of some basic concepts of the model and a few added details on the land and ocean components.

In section 4, definitions used for the data analysis are given. We also discuss how results from the ocean and land runs are compared in a consistent way.

Section 5 discusses the setup of the six simulations performed. Three simulations were performed with the land component and three simulations with the ocean component of CESM. These two sets include a spin-up under preindustrial (1850 AD) conditions, a historical period simulation from 1850 - 2012 and a corresponding control run.

In section 6, the so-called drift in the ocean-only spin-up is discussed. This is necessary to determine whether the spin-up is reasonably close to equilibrium.

Section 7 compares ocean spin-up results to observational data. The focus will mostly lie on variables related to carbon isotopes.

The industrial period simulation will be analysed in section 8. Both the final state and the transition from the preindustrial state into this final state will be discussed. Additionally, the total uptake of radiocarbon due to human activity is calculated.

In section 9, the three land runs are analysed. As for the ocean, a drift analysis for the spin-up is done and the total radiocarbon uptake and its spatial variations are investigated. However, no comparison of the spin-up to observational data is done.

In section 10, we combine the results of the land and ocean run, to see how well they represent the total budget of bomb-produced radiocarbon. And finally, in the last section (section 11), we try to answer the three questions mentioned above and reflect on the results obtained and their implications.

2 Carbon isotopes in the climate system

Carbon(C) occurs in three different isotopes. Isotopes are atoms with the same number of protons but a different number of neutrons. The three carbon isotopes are ^{12}C, ^{13}C and ^{14}C. These isotopes have six protons and six, seven and eight neutrons respectively. ^{12}C is the predominant isotope with 98.9 % of all carbon being ^{12}C, ^{13}C makes up most of the remaining 1.1%, while only $1{\cdot}10^{-10}$% of carbon is ^{14}C. (Jahn et al. (2015))

The different number of neutrons in isotopes changes two important properties: mass and stability of the atom. For carbon, this means ^{12}C is the lightest followed by ^{13}C and ^{14}C is the heaviest. ^{12}C and ^{13}C are stable. ^{14}C on the other hand is not. It decays radioactively, hence it is also called radiocarbon. This decay happens with a half-life of 5700±30 years (Audi et al. (2003)). After this time of 5700 years, half of the original amount of ^{14}C has decayed. Sometimes instead of half-life the lifetime is given, the lifetime of radionuclide is the half-time divided by the natural logarithm of two. For ^{14}C the lifetime is $5700/\ln(2) = 8223$ years.

In the following three sections, special notation when dealing with isotopes and isotopic ratio is introduced and discussed, followed by an introduction to isotopic fractionation. The natural cycle of ^{14}C is discussed, describing where and how ^{14}C is produced and how it enters the different carbon pools. Finally, the ability to use ^{14}C through its radioactive decay as an age tracer for the ocean circulation is explored.

2.1 Isotopic notation

Isotopes are typically discussed in terms of their relative abundance to the total amount of the atom in question. For this purpose, the following ratio is defined: (Here for the example ^{14}C to C)

$$^{14}R = \frac{^{14}\mathrm{C}}{\mathrm{C}} \tag{5}$$

The typical ratio changes little between different pools. Nevertheless there are processes that do change the ratio. Changing isotopic ratios is called fractionation and is the topic of the next section. To accommodate the fact that the ratio changes are small, one often uses the so-called δ-notation defined as follows (Hayes (2004)):

$$\delta^{14}\mathrm{C} = \left(\frac{^{14}R_{sample}}{^{14}R_{standard}} - 1 \right) \cdot 1000 \tag{6}$$

In this formula $^{14}R_{sample}$ is the ^{14}C ratio of the pool, one is interested in, while $^{14}R_{standard}$ is the ratio of a standard, that has to stay the same across different calculations to ensure stability. The result of the formula is given in the permil unit (symbol ‰). +1‰ means 1/1000 higher ratio of ^{14}C to C in the sample than in the standard. The factor 1000 is sometimes omitted in equation 6, as it is implicitly contained in the permil unit (Hayes (2004)). When the δ-value of a pool is positive, it is said that this pool is enriched in that isotope. If the value is negative it is called depleted.

2.2 Isotopic fractionation

Isotopic fractionation means that the standard abundance ratio of isotopes is changed by a process. The main reason fractionation occurs is the different mass of the isotopes (Dauphas and Schauble (2016)).

In processes that do fractionate, one often express the fractionation in terms of the fractionation factor α and the isotopic fractionation ϵ. While α is the actual ratio at which a process prefers to use one isotope over the others, ϵ shows how much a particular process changes the δ value. These two are related to each other through the following equation (Jahn et al. (2015)):

$$\alpha = 1 + \epsilon/1000 \tag{7}$$

An α value smaller than one or a negative ϵ value usually means that the more common isotope (which is usually the lighter one), is preferred over, by this process, the rarer one. The opposite is true for α values larger than one and ϵ positive.

α and ϵ are process dependent. Not only are they process dependent, but they can also heavily depend on the conditions under which a process occurs.

The fractionation depends on the mass difference between two isotopes. The mass difference between ^{12}C and ^{13}C is roughly 1 atomic mass unit while it is 2 between ^{12}C and ^{14}C. Since the mass difference to ^{12}C for ^{14}C is double that of ^{13}C the fractionation is also assumed to be doubled(Dauphas and Schauble (2016)).

$$^{14}\epsilon = 2 \cdot ^{13}\epsilon \tag{8}$$

^{14}C is typically given as Δ^{14}C which is defined as (Stuiver and Polach (1977)):

$$\Delta^{14}\mathrm{C} = \delta^{14}\mathrm{C} - 2\left(\delta^{13}\mathrm{C} + 25\right)\left(1 + \frac{\delta^{14}\mathrm{C}}{1000}\right) \tag{9}$$

This removes the fractionation effects on radiocarbon under the assumption that all fractionation that occured is exactly doubled for ^{14}C compared to ^{13}C. The Δ^{14}C distribution is basically only affected by radioactive decay.

In the following, the major fractionating processes are discussed. All fractionation factors are given for ^{13}C.

2.2.1 Ocean gas exchange

During the exchange of gases between the atmosphere and the ocean, fractionation occurs. There are two kinds of fractionation, equilibrium fractionation and kinetic fraction. Equilibrium fractionation happens when two substance are in equilibrium and can exchange isotopes. Kinetic fraction occurs during a reaction, the rate constant therefore the reaction likeliness changes depending on the isotope. Usually, the lighter isotope can react easier than the heavier isotope Tiwari et al. (2015).

The net ^{13}C flux can be calculated in a similar manner as the net CO_2 gas exchange (2), according to Zhang et al. (1995), in the formulation of Jahn et al. (2015):

$$F^{13} = PV \cdot \alpha_{aq_g} \cdot \alpha_k (R^{13}C_{atm} \cdot C_{sat} - R^{13}C_{DIC} \cdot C_{Surf}/\alpha_{DIC_g}) \tag{10}$$

With α_k being the kinetic fractionation factor, and α_{aq_g},α_{DIC_g} are the equilibrium fractionation factors for CO_2 gas dissolution and between DIC and gaseous CO_2 respectively.

Zhang et al. (1995) give formula to calculate these fractionation factors (in the formulation of Jahn et al. (2015)):

$$\alpha_k = -0.99919 \tag{11}$$

$$\epsilon_{aq_g} = -0.0049 \cdot \mathrm{T} - 1.31 \tag{12}$$

$$\epsilon_{DIC_g} = -0.014 \cdot \mathrm{T} \cdot f_{\mathrm{CO_3}} - 0.105 \cdot \mathrm{T} + 10.53 \tag{13}$$

$f_{\mathrm{CO_3}}$ is the fraction of carbonate in the oceanic DIC (see section 1.3.2 for the DIC composition). The temperature T has to be taken in °C instead of the usual SI-unit (K).

The isotopic fractionation ϵ can be converted to the fractionation factor α using equation 7.

2.2.2 Organic matter production

In the ocean two biological processes which fractionate carbon isotopes, are of relevance for this thesis: Photosynthesis and calcium carbonate formation($CaCO_3$). Fractionation is larger for photosynthesis than for $CaCO_3$ formation. (Jahn et al. (2015))

In the photosynthesis reaction the ratio of ^{13}C to ^{12}C used can be calculated by

$$R_p = R_{CO_2^*}/(\alpha_p) \tag{14}$$

or equivalently

$$R_p = 1000 \cdot R_{CO_2^*}/(\epsilon_p + 1000) \tag{15}$$

(Jahn et al. (2015)), where R_p is the isotopic ratio of the product of photosynthesis and $R_{CO_2^*}$ is the isotopic ratio of CO_2^*. As Jahn et al. (2015) write, there are multiple different approaches to calculate the fractionation factor ϵ_p. Laws et al. (1995) postulated that only CO_2^* is relevant for the photosynthesis reaction. CO_2 enters the cell through diffusion. Additionally they assume an influence of the growth rate μ (measured in d^{-1}) on the fractionation factor. These assumption lead to the equation:

$$\epsilon_p = (\mu/CO_2^* - 0.371)/(-0.015) \tag{16}$$

With 0.371 and -0.015 being fit parameters.

Keller et al. (1999) stated that the model by Laws et al. (1995) is too simplistic and does not match observational values. Therefore they propose a more complex model. It incorporates terms regarding fractionation during active CO_2 uptake and HCO_3^- usage. Their final formula is also published in Jahn et al. (2015).

Calcium carbonate fractionation is small. Ziveri et al. (2003) experimentally found isotopic fractionations of 3‰ to -2‰, the exact value depends on the species forming the calcium carbonate.

2.2.3 Photosynthesis

In the land-atmosphere carbon cycle, the photosynthesis process is one of the most important processes in terms of fractionation. There are multiple different ways the photosynthesis process works exactly within the plants. The two most important ones are so-called C3 and C4 pathways performed by so-called C3 and C4 plants. The difference in how the photosynthesis process is performed result in different fractionation factors. These different fractionation factors cause the signature of the C3 and C4 plants to be considerably different ($\delta^{13}C \approx$ -28‰ for C3 and $\approx$ -14‰ for C4 plants,Melzer and OLeary (1987).

2.3 Natural cycle of ^{14}C

If ^{14}C was just brought to earth billions of years ago when the earth formed, there would be no ^{14}C left. This implies that there must be some form of a radiocarbon source on earth. This source of radiocarbon is the production through high energy cosmic rays. These cosmic rays interact with the abundant nitrogen in the air and form radiocarbon. (Choppin et al. (2002))

The production of radiocarbon in the earth's atmosphere is about $(2.2 \pm 0.6) \cdot 10^{26}$atoms ^{14}C yr^{-1} (Choppin et al. (2002)) or 365 mol. This production is modulated over long and short terms by the earth's and sun's magnetic fields (Castagnoli and Lal (1980)).

Through the air-sea interface, the radiocarbon enters the ocean by gas exchange. ^{14}C is brought into the interior of the ocean by ocean circulation and export production (Sarmiento and Gruber (2006)). In the interior of the ocean with no contact to the atmosphere, the radiocarbon decays back into nitrogen.

Inside the ocean, no new radiocarbon is created. With no new radiocarbon being created and all the existing one decaying, an equilibrium criteria can be formulated. For the ocean to be in equilibrium, in terms of radiocarbon, the uptake of radiocarbon by gas exchange must equal the interior decay. Similarly, the land takes up radiocarbon through the photosynthesis process and a similar equilibrium criteria applies.

2.4 Anthropogenic perturbation of isotopic ratios

As with the general carbon budget of the earth system, carbon isotopes are also influenced by human activities. The most relevant are the fossil fuel emissions and the nuclear weapon tests conducted in the middle of the last century. These perturbations first affected the atmosphere. Through the exchange fluxes of the carbon cycle, the perturbations entered the other carbon reservoirs.

2.4.1 Atmospheric impact

The radiocarbon signature of carbon from fossil fuels is -1000‰. -1000 ‰ means no radiocarbon is found in the sample. Fossil fuels contain no radiocarbon because the organic carbon was formed millions of years ago and all radiocarbon decayed. The -1000‰ signature means if carbon from

fossil fuels is released into the atmosphere the atmospheric $\Delta^{14}C$ value decreases. This depletion due to fossil fuel emissions is called the Suess-effect (Suess (1955)).

The term Suess-effect is also used to describe the decrease in atmospheric $\delta^{13}C$ due to fossil fuel emissions. During the creation of fossil fuels fractionation lead to fossil fuels having a clear negative $\delta^{13}C$. On average roughly -25‰ but this value is dependent on the fuel mix (Andres et al. (2000)). If these fuels are now burned the released carbon has the same isotopic signature (Keeling (1979)). Since the atmospheric preindustrial $\delta^{13}C$ is -6.6 ‰, these emissions lead to a decrease of the atmospheric $\delta^{13}C$.

In addition to the Suess effect, radiocarbon is also influenced by the nuclear weapon tests mainly conducted in the 1950s and 60s. Neutrons created by the nuclear tests reacted with nitrogen in the environment to form radiocarbon. This is the same reaction that also forms natural radiocarbon. Radiocarbon formed during these bomb tests is often referred to as bomb radiocarbon. There are large uncertainties in how much bomb radiocarbon was produced (Naegler and Levin (2006)), the uncertainties stemming from a lack of clear knowledge on the actual neutron yield of such bomb tests. The neutron yield means the number of neutrons produced per explosive unit.

There are also other human activities contributing to the atmospheric $\delta^{13}C$ and $\Delta^{14}C$ changes. These include nuclear power plants producing radiocarbon and other carbon emissions not from fossil fuels having their own isotopic signature. These effects play a minor role for $\Delta^{14}C$ compared to the Suess effect and nuclear weapon tests (Naegler and Levin (2006)).

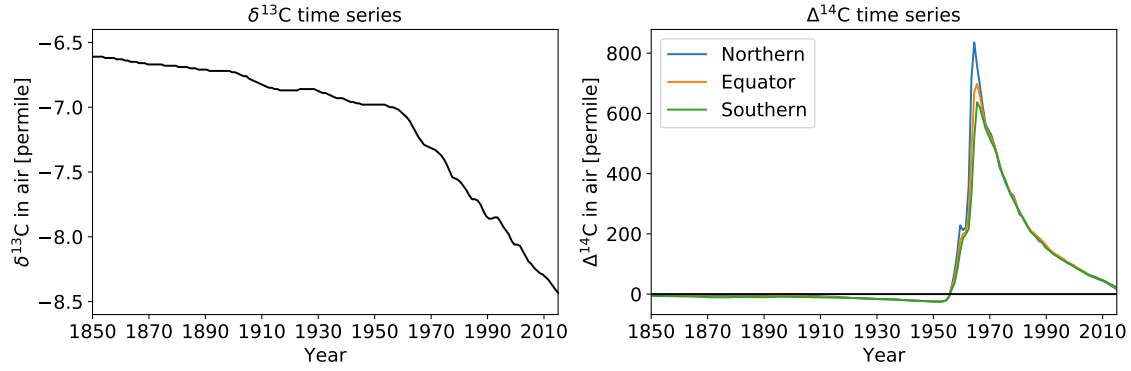

Figure 6: Atmospheric ^{13}C and $\Delta^{14}C$ (Graven et al. (2017)).

Figure 6 displays the atmospheric $\delta^{13}C$ and $\Delta^{14}C$ time series compiled by Graven et al. (2017). $\delta^{13}C$ is given as one global value, while $\Delta^{14}C$ is given for three latitudinal bands of 60° each. These values are, similarly to the CO_2 record, compiled from direct measurements and ice core measurements.

δ^{13} decreases from -6.61‰ in 1850 to -8.42‰ in 2014. In the 1960s the decrease is accelerating, this coincides with the acceleration of the CO_2 emissions. This decrease is mainly caused by the Suess effect for ^{13}C. From 1850 to the mid-1950s, the Suess effect caused a $\Delta^{14}C$ decrease from roughly 0‰ to around -25‰. Starting in 1954, a rapid increase in atmospheric $\Delta^{14}C$ is visible, with the nuclear weapon test being the main cause. This leads to a $\Delta^{14}C$ value of almost +800‰ in the northern hemisphere. This spike is short-lived and by 2015 preindustrial values are almost reached once again. The reasons for the decrease of atmospheric $\Delta^{14}C$ after 1965 are both the Suess effect and the redistribution of the extra radiocarbon to other inventories. The decay of bomb radiocarbon, in the 60 years passed since the tests, is of minor relevance. In 60 years only around 10‰ of an initial amount of radiocarbon decays. Most nuclear weapon test were conducted in the northern hemisphere. This caused a large inter-hemispheric $\Delta^{14}C$ gradient of over 200‰ in 1965, which decreased rapidly back to the preindustrial gradient of only a few permil.

2.4.2 Oceanic impact

It is to be expected that the ocean lags the atmosphere in response to the nuclear bomb test. As the mixing time of the ocean is in the hundreds of years or more Matsumoto (2007). Only 50 years after the tests, one would not assume to find a well-mixed ocean. Therefore the effect of the bombs will be limited to the surface and upper ocean. The effect of the bomb radiocarbon in the surface

ocean was a massive enrichment in $\Delta^{14}C$. For $\delta^{13}C$ only the Suess-effect matters, hence the surface ocean is depleting in $\delta^{13}C$ due to the anthropogenic influence.

For the ocean, one of the main issues in quantifying the anthropogenic impact is the lack of measurements prior to the bomb test in the 1950s. Therefore techniques have to be used to separate the anthropogenic and the natural part of any radiocarbon signal currently measured in the ocean.

To separate natural and bomb produced $\Delta^{14}C$, relationships of natural radiocarbon to other oceanic tracers were exploited. Broecker et al. (1995) showed a method using the correlation between natural radiocarbon and dissolved silica to split measurements into natural and bomb radiocarbon. A similar method, using so-called potential alkalinity instead of dissolved silica was developed by Rubin and Key (2002). The GLODAP dataset by (previously shown in section 1.3) Key et al. (2004) used the potential alkalinity method by Rubin and Key (2002) to calculate the natural radiocarbon distribution in the upper ocean.

For ^{13}C the same problem existed. Eide et al. (2017) provide a dataset of ^{13}C preindustrial values. The dataset is vertically and spatially resolved on a global scale. However, no preindustrial data is available for the top 200m. The method used to calculate the preindustrial values from the measured values was not good enough to give usable result for the top 200m.

One measure of the anthropogenic influence on the oceanic radiocarbon content is the so-called bomb radiocarbon inventory. This refers to the amount of extra radiocarbon stored in the ocean since 1945. This means the bomb inventory is the total radiocarbon content of the ocean in a specific year minus the oceanic radiocarbon content in the year 1945.

A current year - fix year definition accounts for other effects, in addition to the uptake of bomb-produced ^{14}C. The atmospheric radiocarbon was not only changed through nuclear weapon test but also through the Suess effect (compare section 2.4). Further, the atmospheric total carbon content changed which also affects the radiocarbon flux into the ocean. Note that for these reasons Naegler and Levin (2006) used the term *excess* radiocarbon instead of *bomb* radiocarbon.

1945 is the starting year chosen under the assumption that no relevant bomb tests happened prior (Naegler and Levin (2006)). Choosing a different reference year has an influence. A later year reference year might miss early bomb tests, while an earlier year is more influenced by the Suess effect, which was more relevant before the bomb tests.

Naegler and Levin (2006) compiled different observation-based estimates of the oceanic bomb budget. These estimates range from 35.7 - 58.0 kmol in 1975 and 54 - 59 kmol in 1995. Most of these estimates themselves give errors of up to roughly 10 kmol. The range for the bomb budget in 1975 is larger because more estimates were considered. Some of the higher estimates were later questioned.

2.5 Natural isotopic distribution in the ocean

$\delta^{13}C$ and $\Delta^{14}C$ distributions both show large vertical and horizontal gradients in the ocean. While $\delta^{13}C$ ranges from 0.5 to 2.6 ‰, $\Delta^{14}C$ has a considerably larger range from -30 ‰ to -270‰

^{13}C is enriched throughout the ocean because of the fractionation during gas exchange. Vertical and horizontal δ^{13} gradient are anti-correlated to those in the DIC distribution. The DIC distribution is shown in section 1.3. Fractionation during organic matter production is the main cause for this anti-correlation, as organic matter production favors ^{12}C over ^{13}C. Therefore ^{13}C is enriched at the surface and less so in the deep ocean.

^{14}C experience the same fractionation and transport processes that lead to the horizontal and vertical gradients in $\delta^{13}C$. However $\Delta^{14}C$ is corrected for fractionation. $\Delta^{14}C$ only reflects the influence of radioactive decay and transport processes. Thereby the $\Delta^{14}C$ distribution might be used as an age tracer (see section 2.6).

At the surface of the ocean radiocarbon is already heavily depleted. This surface depletion ranges from -30‰ in mid latitudes to -130‰ in the Southern Ocean. This constant disequilibrium of the surface ocean with the atmosphere results from old water upwelling to the surface. At the surface, the water remains shorter than the five years that would be needed to reach equilibrium with the atmosphere (Matsumoto (2007)).

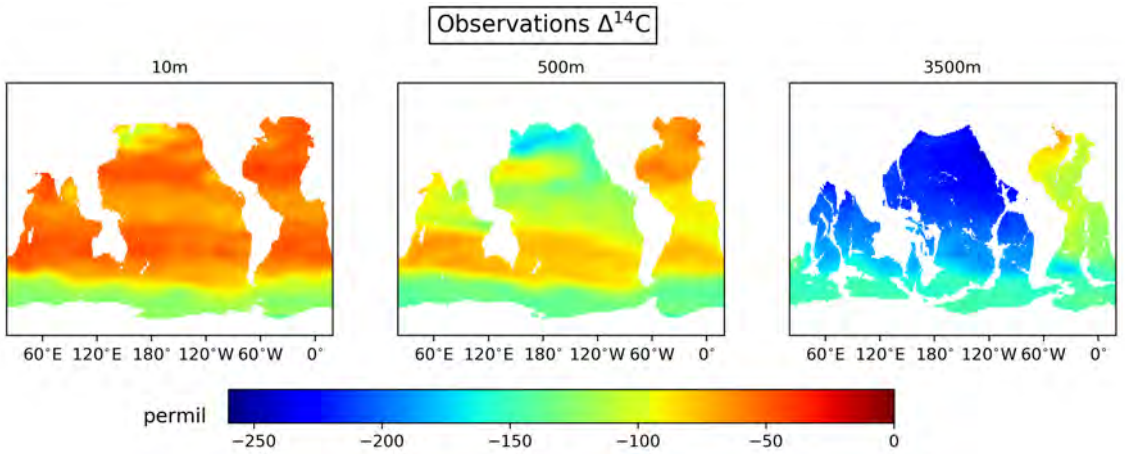

Figure 7: Natural radiocarbon distribution (GLODAP data (Key et al. (2004)). Note that GLODAP does not contain $\Delta^{14}C$ values for the ocean north of 60°N

The deep water circulation is the dominating factor governing the deep water $\Delta^{14}C$ distribution (see section 1.3.3). ^{14}C decays while water is transported by the deep water circulation. $\Delta^{14}C$ is relatively high in the North Atlantic, with values ranging from -60 to -80‰. The southward flow in the deep Atlantic leads to ^{14}C depletion. The Southern Ocean is highly depleted about -130‰. The northern Atlantic deep water arriving in the Southern Ocean is strongly depleted due to the long transport path. When this ^{14}C depleted water flows from the Southern Ocean into the deep and intermediate Pacific and Indian Ocean radiocarbon continues to decay. This results in the deep and intermediate Pacific showing the strongest depletion. Lowest $\Delta^{14}C$ values are found in the deep North Pacific with values of less than -230‰. This means the North Pacific deep water has roughly one quarter less radiocarbon per carbon than the surface waters.

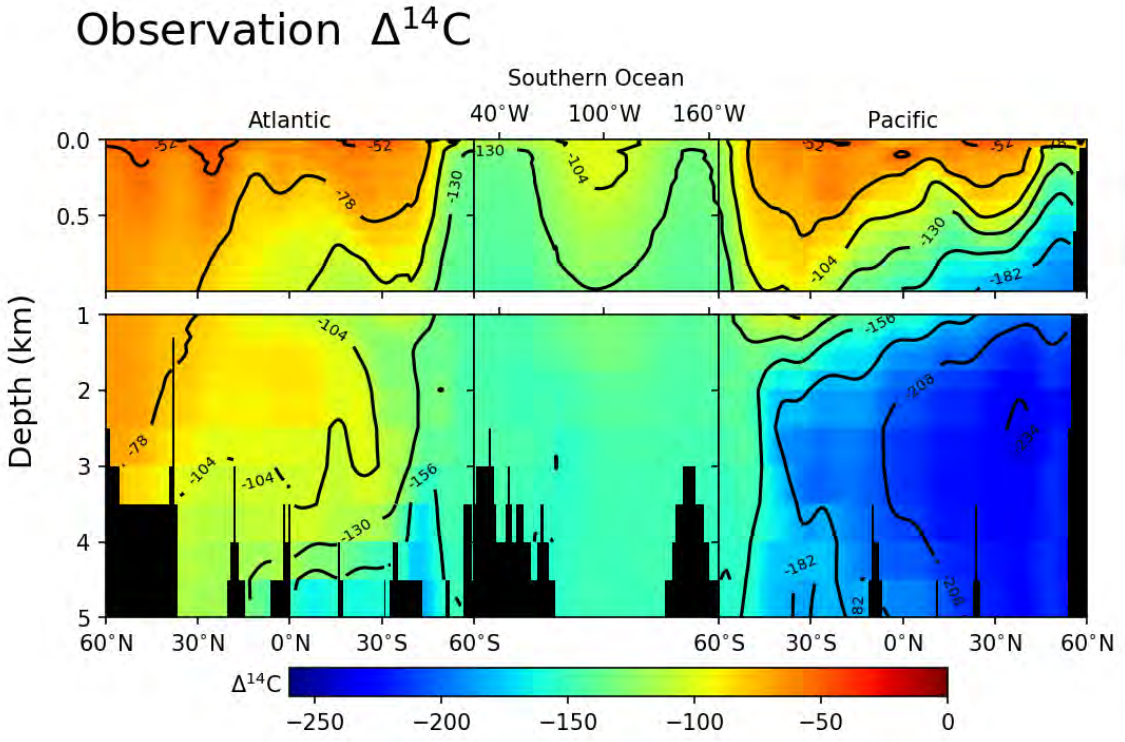

Figure 8: Natural radiocarbon distribution along a vertical transect from the North Atlantic, around Antarctica into the North Pacific (GLODAP data (Key et al. (2004)). This transect is shown in figure 11.

This flow also dominates the vertical profiles, as can be seen in figure 8. The Atlantic water

gets more depleted, further south and further downward. When it mixes with the Southern Ocean deep water a relatively uniform distribution of Δ^{14}C is created. In the Pacific Ocean the influx of highly depleted water at the bottom combined with the relatively low surface depletion creates a large surface to deep gradient. Δ^{14}C in the north Pacific changes by roughly 200‰ within just 2000m of depth.

2.6 ^{14}C as an age tracer

The age of a water parcel can be defined as the time elapsed since it was last in contact with the surface. In a model, this age can be calculated by caring an additional tracer called ideal age. However in reality no such ideal age tracer exists (Hall and Haine (2002)).

^{14}C possess three properties similar to an ideal age tracer. The first being it 'ages' at a well-defined rate, by decaying radioactively. The second being it exchanges with the atmosphere at the surface, which resets the age. Finally, there are no internal sources of radiocarbon in the ocean, changing the age.

With the radioactive decay, the radiocarbon age of any water sample can be calculated as:

$$\theta = 8267 yrs \cdot \ln(1 + \Delta^{14}\text{C}/1000) \tag{17}$$

θ is the age of the water in yr. 8267 yrs is the life time of ^{14}C and ln represent the natural logarithm.

The problem in using ^{14}C comes from the second property, the air-sea gas exchange. As seen before, the water at the surface is depleted in Δ^{14}C relative to the atmosphere. This depletion arises as the resident time of water in the surface layer is typically substantially shorter than the time needed to bring this water in equilibrium with the atmosphere by gas exchange. This means when calculating the age, ages greater than 0 would be calculated for the surface water. The age calculated for surface waters is also called reservoir age. Unless the reservoir age of the last point of contact with the atmosphere is known, it is impossible to calculate the water age through Δ^{14}C precisely.

As mentioned in section 2.5, there are two major deep water sources. Broecker et al. (1998) used a tracer, PO_4^*, to determine the fraction of North Atlantic Deep Water and southern sourced deep water in the Atlantic. Using this method Matsumoto (2007) calculated radiocarbon based circulation ages, that agreed with other assessments of deep water ages.

It is possible to use ^{14}C as an age tracer. However, due to the reservoir age, it is not as straight forward as perhaps envisioned at first sight. Using more or less sophisticated methods to subtract the reservoir age, one can achieve good results with ^{14}C as an age tracer.

3 Isotope-enabled CESM2

The Community Earth System Model version 2 (CESM2) is a coupled earth system model developed by the National Center for Atmospheric Research and other institutions. It is capable of simulating the climate of the earth at the present state, predict future states and hindcast past states (Danabasoglu et al. (2020))

3.1 General model description

The CESM consist of seven different components: ocean, land, atmosphere, sea-ice, land-ice, wave and river runoff. These seven components do not communicate directly to each other, instead, communication is handled by a so-called coupler. This coupler takes input from each component and communicates the appropriate data to the other components. (Danabasoglu et al. (2020))

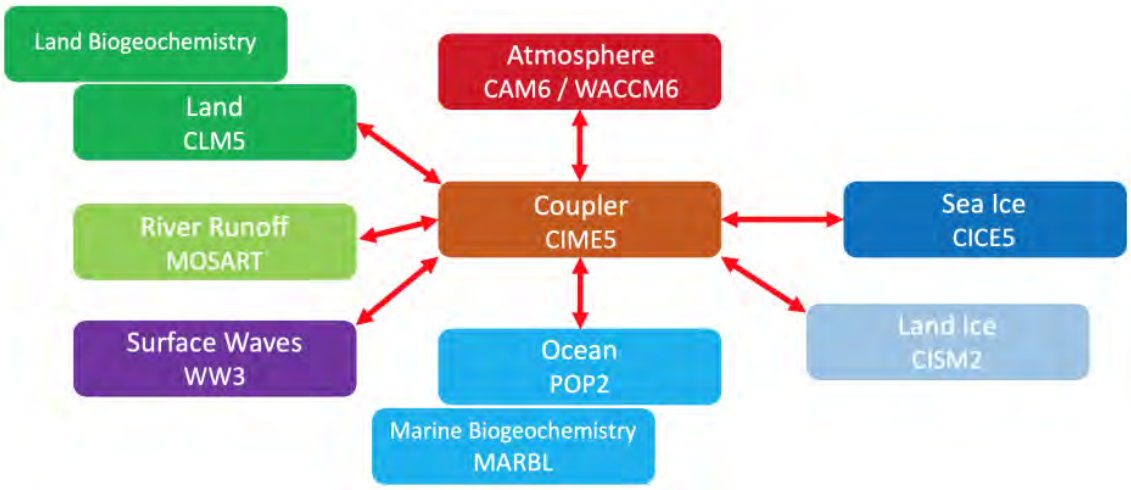

Figure 9: The components of the CESM model and the central communication through the coupler (Danabasoglu et al. (2020)).

With this setup, it is possible in CESM to replace components. One replacement that exists for all components is the so-called data models. Passive components that read fixed values from some files and send these to coupler. CESM allows the user to decide which components should be active components and which ones inactive (Danabasoglu et al. (2020))

3.2 Ocean component

The active ocean model used in CESM is POP2, standing for Parallel Ocean Program version 2. POP is a general ocean circulation model, capable of running both in a stand-alone mode coupled to the sea ice module, and driven by an atmospheric data model or fully coupled with an interactive atmosphere. General circulation models such as POP solve the primitive fluid equations on a sphere. Processes operating on scales too small to be fully resolved by the model are parameterized (Kerbyson and Jones (2005))

As the name implies POP is able to be run in parallel for increased efficiency. Various options for parameterizations, grids and other features can be customized. These options and the amount of parallelization determine the performance of the model (Kerbyson and Jones (2005)).

POP runs together with the sea-ice model to which it communicates features such as salinity depending freezing points. Additionally, these two components are always run on the same grid.

For more information and a more technical description of the POP model, the reader is referred to the POP manual (Smith and Gent (2002)).

3.2.1 Grid

The primary ocean grid used is the so-called gx1v7 grid. This grid is a displaced pole grid with a resolution of roughly 1 °. There are 384 latitudinal bands, 320 longitudinal bands and 60 depth

levels. The grid stops at 80°S and the north pole is displaced to Greenland. The horizontal grid is a regular latitudinal/longitudinal grid from 80°S to the equator. In the northern hemisphere, the grid shifts into a displaced pole grid. Grid spacing is smaller around the equator. Numerical problems are caused by the polar grid singularity. The gx1v7 grid resolves these problems with the displacement of the northern pole to Greenland (see Murray (1996); Madec and Imbard (1996)). This solves the problem as both poles are then overland.

The 60 vertical levels expand from the ocean surface to a depth of 5500 m. The layers differ in thickness. The first 15 layers are 10 m thick. The layers 15 - 50 then increase in thickness from 10 m to 250 m. The last 10 layers are all 250 m deep. Therefore surface processes such as most biological processes are represented at a higher resolution.

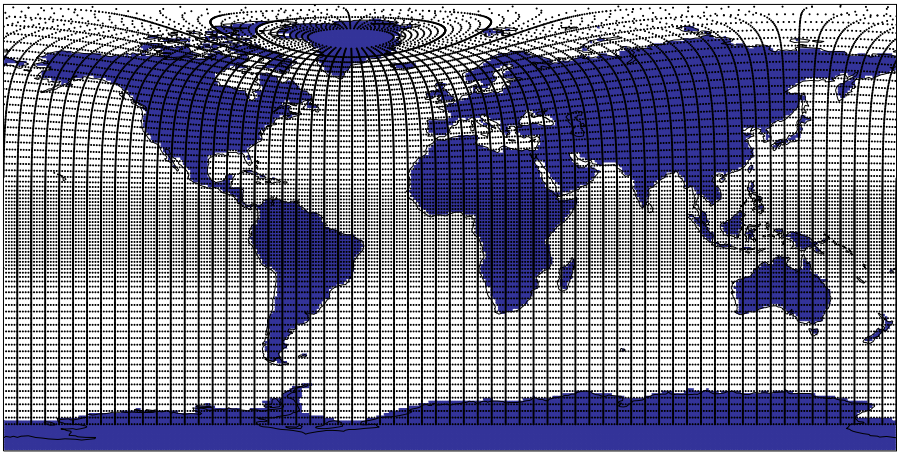

Figure 10: The gx1v7 grid used for the ocean-sea ice component. Every 5th grid line is shown. In the projection used in the figure, a regular latitude/longitude grid would result in quadratic cells of the same size everywhere. Colored in blue is the land area in the model

3.2.2 Marine biogeochemistry - MARBL

In CESM ocean biogeochemistry is not directly handled by the oceanic component POP2 but is instead handed off to the so-called Marine Biogeochemistry library MARBL. Biogeochemical cycles of key elements are implemented. These include C and its isotopes ^{13}C,^{14}C, N, P, Fe, Si, O, and alkalinity. (Mar)

The model features seven different tracers containing carbon: dissolved inorganic carbon, dissolved organic carbon, $CaCO_3$, three different phytoplankton pools (diazotrophs, diatoms, small phytoplankton) and one zooplankton pool. (Jahn et al. (2015)). The growth of these groups is limited by multiple nutrients (nitrate, ammonium, phosphate, silicate, and iron) (Mar). Additionally, the model features variable N/P ratios depending on which species dominate, however, the ratio is fixed for any particular species (Mar).

Carbon isotopes in the ocean are handled by MARBL. For numerical reasons, the two isotopes are scaled. This means $^{13}R_{std} = 1$ and $^{14}R_{std} = 1$. Jahn et al. (2015) implemented the carbon isotopes into the ocean component of the CESM.

Fractionation of the carbon isotopes works as described in section 2.2. This means for the air-sea gas exchange the fractionation factor is calculated as described in Zhang et al. (1995). For the photosynthesis fractionation, the scheme by Laws et al. (1995) is used. This scheme was used based on an assessment by Jahn et al. (2015) weighing the factors of computational complexity and ability to represent observational data. A small fractionation factor of 2‰ is used for calcium carbonate formation (^{13}C). In the model $^{14}\epsilon = 2 \cdot^{13} \epsilon$ for all types of fractionation. (Jahn et al. (2015)).

^{14}C decays in the model with a half-life of 5730 years. This is an older number by Godwin (1962). Orr et al. (2017) recommend using the updated value of 5700 years as a half-life.

The atmospheric values for the carbon isotopes are not read in through the coupler. Instead, the isotopic values are read in from either a file or a constant value is used. One can either provide one uniform global value or three values for three latitudinal bands. This also means that at the current state of the model it is not possible, to perform a fully coupled isotopes enabled run

with freely evolving atmospheric $\delta^{13}C$ and $\Delta^{14}C$ values. For this, it would be necessary to receive isotopic values from the atmosphere.

For the air-sea gas exchange MARBL uses equation 2 with:

$$PV = (1 - aice) \cdot a \cdot u_{10}^2 \cdot (660.0/S_{C_{CO_2}})^{-1/2} \tag{18}$$

In this equation: aice is the fraction of a grid cell covered by ice, u_{10} is the wind speed at 10m above sea level, $S_{C_{CO_2}}$ is the Schmidt number for CO_2 (Jahn et al. (2015)). The coefficient a is taken according to Wanninkhof (2014) as 0.251 cm h^{-1}. The value of $a = 0.251$ cm h^{-1} does not comply with the recommendation of the Ocean Model Intercomparison Project (OMIP), where a is set to 0.337 cm h^{-1} (Orr et al. (2017)). $a = 0.251$ cm h^{-1} is also substantially lower than it was in earlier versions of the model, in the Jahn et al. (2015) study it was set to $a = 0.31$ cm h^{-1} .

In addition to the carbon isotopes described above, the model can also simulate so-called abiotic ^{14}C. Abiotic ^{14}C decays like regular ^{14}C, but as the name implies it is unaffected by biotic processes. Additionally, abiotic ^{14}C is not fractionated, which implies values can be directly interpreted as $\Delta^{14}C$. To differentiate the regular ^{14}C from the abiotic ^{14}C it is also referred to as biotic ^{14}C. The abiotic ^{14}C tracer is not handled by MARBL but instead directly by the ocean component POP.

3.3 Land component

The active land component of CESM is called the Community Land Model (CLM). It models the different physical, chemical and biological process that ultimately determine the effect of the land surface and the land biosphere on the climate system. The model deals among other things with the land heterogeneity, the different plant types and the reflective and absorption properties of the land surfaces. (CLM)

The standard grid has a resolution of $0.9° \times 1.25°$. Unlike the ocean, the land is much more heterogenic, within a few kilometers land structure can change. Forests, cities, lakes, glaciers and crop fields can be found within a few kilometer. These structures behave very differently in terms of physical properties. As these structures can be finer than the grid resolution, the model allows each grid cell to have multiple so-called land units. These land units model the vertical flexibility with columns containing 25 layers and up to five snow layers (CLM) .

Vegetation is modelled by so-called plant functional types. A total of 15 different plant functional types are represented in the CLM. These plant functional types represent different kinds of plants, grouping together plants that work similarly under external conditions rather than modelling individual species (CLM).

3.3.1 Carbon isotopes

^{14}C decays, as in the ocean component, with a half life of 5730. The standard ratios are different than in the ocean model. While in the ocean model works with $^{13}C/C$ and $^{14}C/C$ are set to 1, in the land model they are $^{13}C/C = 0.0112372$ and $^{14}C/C = 10^{-12}$. Especially for the radiocarbon, this ratio is problematic as the real ratio is $1.176 \cdot 10^{-12}$. (CLM)

Fractionation solely occurs during the photosynthesis step. The fractionation factors are as discussed in section 2.2.3 for ^{13}C. However for ^{14}C, there is no fractionation, the reason given is that the ^{14}C should be independent of ^{13}C calculations. Also, measurements are often reported as $\Delta^{14}C$. In terms of atmospheric carbon isotopic input, the land works similar to the ocean. It reads the atmospheric values not through the coupler but from a specified file or value. Again three latitudinal band values for $\Delta^{14}C$ and one global value for $\delta^{13}C$ are considered. (CLM)

4 Data-analysis

^{14}C and other variables of interest are three-dimensional fields within the ocean. As such visualizing the distribution in a way that makes a comparison between model and observational data possible can be approached by many different ways, from averaging to section to single-cell comparisons.

We used the climate data operators (CDO) to regrid the model to the observational grid. The regridding is not conservative and does change some results when averages over the entire globe are computed. However, the effect is very small.

The grid used for both the model and the observations has grid cells with different area and volume. Grid cell area or volume are used as weights when calculating horizontal or vertical averages. For data - model comparison, averages are only taken over regions where both the observations and the model results are defined.

Vertical transect through the ocean are plotted in this thesis along the path shown in figure 11 (red line). This transect is similar to that used by Sarmiento and Gruber (2006). It goes from the northern Atlantic, through a sector of the Southern Ocean and finally to the northern Pacific. Thereby this transect covers the main water masses in the Atlantic, the Pacific and the Southern Ocean. It does not cover the Indian ocean in any way. In this thesis the Southern Ocean is defined as the region south of 35 °S. The extent of the Atlantic, Pacific and Indian Ocean are as indicated in figure 11

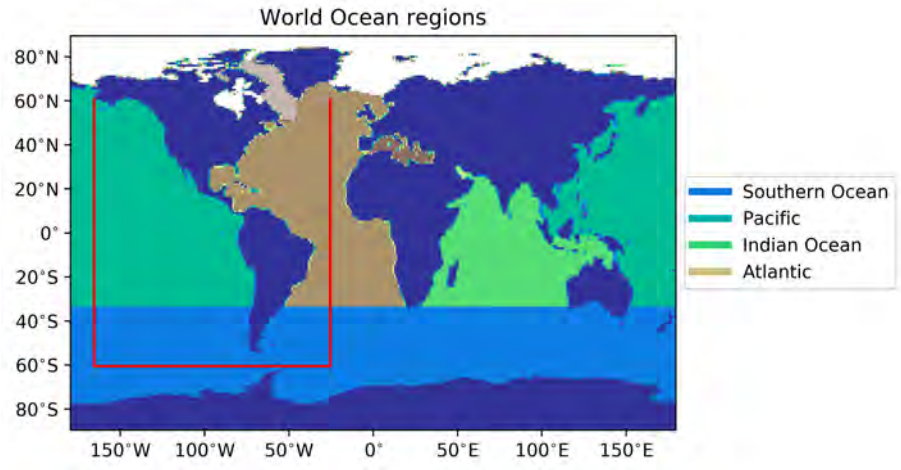

Figure 11: Different region as used in this thesis and based on region definitions used in CESM are indicated by colors. Vertical transects are plotted along the path indicated by the red line.

For the data analysis, we face another problem. As previously mentioned the land and ocean model components do not use the same ratios of ^{14}C/C. To determine the absolute number of ^{14}C atoms in the two model components, we adjust results to the correct ratio of $1.176 \cdot 10^{-12}$. Ocean results are multiplied by $1.176 \cdot 10^{-12}$, while land results are multiplied by 1.3707 (see below for an explanation why not 1.176). All results presented will always be adjusted by these factors.

A second problem in the combination of the results of the two models is that the ocean model outputs data in mmol/m^3, while the land model uses units of g/m^2. In this thesis, all results are converted to mol. To convert to mol, we use the molecular weight of 14 g/mol for ^{14}C. Keep in mind that the ratio $1.176 \cdot 10^{-12}$ is the particle ratio of ^{14}C/C, not their mass ratio, to get to the mass ratio we multiply:

$$1.176 \cdot 10^{-12} \frac{14}{12.011} = 1.3707 \cdot 10^{-12} \tag{19}$$

with $1.3707 \cdot 10^{-12}$ being the mass ratio. Because $1.3707 \cdot 10^{-12}$, is the mass ratio and the land results are given in g/m^2, we multiply land results with 1.3707 instead of 1.176.

5 Setup of the simulations

A total of six model runs are performed. All runs have either the land or the ocean component active, while the rest of the components remain as inactive data components. For both land and ocean, a spin-up is performed. This spin-up is then used as a starting point for both an industrial period simulation from 1850 - 2015 as well as a control run of the same length using mostly the same boundary conditions as the spin-up.

Table 1 gives an overview of the simulations performed. Listed are the run length and some basic facts about the boundary and starting conditions. The rest of this section will focus on examining the setup of the individual runs in more detail.

Name	Short Name	Duration	Setup
Ocean only; Spin - up	SPIN_OC	1350 years	CORE2 - NYF, preindustrial CO_2, $\delta^{13}C$, $\Delta^{14}C$, start from NCAR Spin up, C-isotopes initialized by Eide et al. (2017) and abiotic ^{14}C
Ocean only; Control	Ctrl_OC	165 years	JRA55 (1958-1977), preindustrial CO_2, $\delta^{13}C$, $\Delta^{14}C$, start from SPIN_OC
Ocean only; Industrial Period Simulation	IND_OC	165 years	JRA55, transient CO_2, $\delta^{13}C$, $\Delta^{14}C$ (1850-2015), start from SPIN_OC
Land only; Spin - up	SPIN_LND	750 years	GSWP3(1901-1920), preindustrial CO_2, $\delta^{13}C$, $\Delta^{14}C$, start from NCAR spin-up
Land only; Control Period Simulation	Ctrl_LN	165 years	GSWP3(1901-1920), preindustrial CO_2 , $\delta^{13}C$, $\Delta^{14}C$ (1850-2015), start from SPIN_LND
Land only; Industrial Period Simulation	IND_LN	165 years	GSWP3(1901-2016), transient CO_2, $\delta^{13}C$, $\Delta^{14}C$ (1850-2015), start from SPIN_LND

Table 1: Runs performed with the CESM.

We ran the model at CSCS (Centro Svizzero di Calcolo Scientifico; Swiss National Supercomputing Centre). Performance of 13 model years per day was achieved for an isotope enabled ocean-sea ice only model setup and using twelve computing nodes. The model crashed when trying to use more than twelve nodes for the ocean - sea-ice only simulation. For less than twelve nodes the speed downgrade was linear with the number of nodes used. For the land model, using 30 computing nodes, a performance of 85 model years per day was achieved. Thus the throughput is 1.1 model years per node per day for the ocean and 2.8 model years per node for land.

5.1 Spin-up and control

The purpose of the ocean only spin-up is to bring the ocean into equilibrium with the atmospheric boundary conditions. Having an ocean in equilibrium, it is then possible to see how such an ocean reacts to changes. Therefore this spin-up is the basis for future runs such as the industrial period simulation.

5.1.1 Boundary conditions

The ocean only simulation needs atmospheric boundary information. The main difference to a coupled simulation is that these boundary conditions are read from prescribed files instead of being dynamically calculated.

For the atmospheric temperature and wind fields, the CORE2-NYF (Coordinated Ocean-Ice Reference Experiment 2 normal year forcing) (Yeager and Large (2004)) is used. The normal year forcing does not represent one specific year of the past. Instead, it is compiled from the CORE2 years (1948-2009) to best represent an average year. The normal year forcing is additionally

designed to be continuous from December to January to avoid having a jump at the end of every year.

During the spin-up CO_2, $\delta^{13}C$ and $\Delta^{14}C$ in the atmosphere are held constant. One globally uniform value is prescribed for CO_2 and $\delta^{13}C$, while $\Delta^{14}C$ is given for three latitudinal bands. The values are representative of preindustrial conditions around 1850. For $\delta^{13}C$ and $\Delta^{14}C$ the values given by Graven et al. (2017) for 1850 are used. While for CO_2 the global average value for 1850 in the Meinshausen et al. (2016) dataset is used (Table 2).

Variable	Value
CO_2	284.7 ppm
$\Delta^{14}C$ 90° N - 30° N	-2.3 ‰
$\Delta^{14}C$ 30° N - 30° S	-4.0 ‰
$\Delta^{14}C$ 30° S - 90° S	-5.8 ‰
$\delta^{13}C$	-6.61 ‰

Table 2: Atmospheric CO_2, $\Delta^{14}C$ and $\delta^{13}C$ prescribed in the spin-up and control simulations

5.1.2 Setup

The starting fields for the spin-up were prescribed from files downloaded from NCAR (the b.e21.B1850.f09_g17.CMIP6-piControl.001 case files). These files contained the results from a spin-up CESM ocean-only model run under preindustrial atmospheric conditions. However, no initial data for biotic ^{14}C and $\delta^{13}C$ are provided. Therefore, a new spin-up had to be performed to create equilibrated isotopic distributions with the preindustrial atmosphere.

To have the model reach an equilibrium as fast as possible it is necessary to initialize the isotope fields as close to the expected outcome as possible. The Eide et al. (2017) preindustrial dataset is used. This dataset, however, contains no data for the top 200m. We used the values from 200 m depth for the layers above 200 m. This means, at the start, $\delta^{13}C$ is vertically constant over the first 200 m.

For initializing $\Delta^{14}C_{biotic}$, the $\delta^{14}C_{abiotic}$ contained in the files from NCAR was used. The following equation is used:

$$\Delta^{14}C_{biotic} = (\delta^{14}C_{abiotic} + 50) \cdot 1.052 \tag{20}$$

This equation is derived from the fact that abiotic ^{14}C does not fractionate and therefore directly represents $\Delta^{14}C$. As biotic ^{14}C does fractionate a similar conversion as from $\delta^{14}C$ to $\Delta^{14}C$ had to be performed.

The spin-up was run for a total of 1350 model years. There were two stops necessary during that 1350 year run, one to extrapolate the trend and speed up the equilibration process, the other to correct a mistake. These two stops will be discussed in the next section.

A spin-up duration of 1350 years is considerably shorter than used in other similar studies. Jahn et al. (2015) ran an older, coarse resoultion version of the model for 6000 years for their spin-up. With another model, Dentith et al. (2019) made a 10 000 year spin-up. For the OMIP (Ocean Model Intercomparison Project) (Orr et al. (2017)) it is suggested that models with isotopes enabled should have a spin-up of a least 2000 years.

5.1.3 Corrections

Within the 1350 year run of the spin-up two adjustments were made. One at the model year 675 and the second one at the model year 1250.

The spin-up was first stopped in model year 675. To speed up the process isotopic carbon pools were adjusted using the trends from the previous 200 model years.

$$C_{675new} = C_{675old} + (C_{675old} - C_{475}) \tag{21}$$

Where C_{675new} is the content of variable C after the correction, C_{675old} is the value at year 675 prior to the correction and C_{475} is the value at model year 475. Afterwards, the model run was continued with the new adjusted variables. The $DI^{14}C$,$DO^{14}C$, $DI^{13}C$ and $DO^{13}C$ pools were adjusted. Note that the effect of this stop is basically putting the model 200 years forward in time under the assumption that the trends stayed the same.

Originally it was planned to only run 1250 years of spin-up, but analysing the results from 1250, it became apparent that it was necessary to adjust the radiocarbon pools. Radiocarbon content was too low throughout the entire ocean when compared to observations. Meaning the ocean showed low surface concentrations as well as low deep ocean concentrations. Through air-sea gas exchange, a low surface concentration should lead to a large flux, which in turn should lead to a large total ocean inventory. If the flux is large, the inventory has to be large, since in equilibrium the internal decay has to match the flux into the ocean.

The problem was that CESM was expecting $\delta^{14}C$ as atmospheric input. The values provided in table 2 are $\Delta^{14}C$. The two are related through equation 9. $\delta^{14}C$ is always larger than $\Delta^{14}C$. This means that if $\Delta^{14}C$ is treated as $\delta^{14}C$ the atmospheric radiocarbon content was perceived too low. A low atmospheric radiocarbon content leads to a low surface ocean flux, explaining the apparent contradiction discussed above.

To solve this problem, we need to convert $\Delta^{14}C$ to $\delta^{14}C$. Using equations 6 and 9, one can show that:

$$\delta^{14}C = \left(k\left(1 + \frac{\Delta^{14}C}{1000}\right) - 1\right) * 1000 \tag{22}$$

with

$$k = \frac{1 + \frac{\delta^{14}C}{1000}}{1 + \frac{\Delta^{14}C}{1000}} = \frac{500}{475 - \delta^{13}C} \tag{23}$$

Therefore we used equation 22 to correct the atmospheric input values at model year 1250 to:

Variable	Value
$\delta^{14}C$ 90° N - 30° N	35.796 ‰
$\delta^{14}C$ 30° N - 30° S	34.031 ‰
$\delta^{14}C$ 30° S - 90° S	32.163 ‰

Table 3: Corrected $\delta^{14}C$ values for the atmosphere

The above-mentioned correction only changes the atmospheric radiocarbon signature to a realistic value. Meaning an adjustment to the ocean is still necessary. Assuming the oceanic ^{14}C inventory scales linearly with the atmospheric one, all seven radiocarbon pools in the model were multiplied by the factor k from equation 23. Given $\delta^{13}C = -6.61‰ \Rightarrow k = 1.038$.

This correction is an approximation as $\delta^{13}C$ and carbon are not uniformly distributed in the ocean. Therefore, the spin-up was continued for another 100 years, to ensure the changes have time to affect the ocean correctly. The oceanic abiotic radiocarbon reads from the same source. But since abiotic radiocarbon needs $\Delta^{14}C$ instead of $\delta^{14}C$ since it does not fractionation, abiotic radiocarbon read in the wrong atmospheric values after 1250 making it unusable afterwards.

5.2 Industrial period simulation

The industrial period simulation simulates the changes in the ocean due to the changing atmospheric conditions from 1850 to 2015. The run should capture the changes in oceanic carbon isotopic composition due to the rising atmospheric CO_2 level and changing $\Delta^{14}C$ and $\delta^{13}C$. To this end, atmospheric boundary conditions, that adequately represent the atmospheric changes, need to be used.

There does not exist an adequate observation-based data set containing the necessary climatic boundary conditions from 1850 to 2015. Such a data set would need to contain information on the temporal and spatial evolution of the surface air temperature, wind speed and precipitation.

There exist forcing sets such as CORE2 (Yeager and Large (2004)) covering the period from 1948 to 2009 or JRA55 (Japanese reanalysis (Kobayashi et al. (2015))) covering the period from 1958 to 2016 (Kobayashi et al. (2015)). These two datasets cover the entire surface atmosphere and are typically used to force for ocean models. The usual solution to circumvent the lack of a complete temporal data set is to repeat cycles of a limited data set such as JRA or CORE2. A problem is that the global surface air temperature differs by about 0.8 degrees between the starting years of these time-series and the end year. This temperature jump lead Jahn et al. (2015) to stick to CORE2-NYF (normal year forcing) for their industrial period run. They note that having a huge temperature jump close to the large $\Delta^{14}C$ change could affect the ^{14}C uptake of the ocean.

We decided to use JRA55 for climatic boundary condition. However, instead of repeated full cycles, five cycles of the first twenty years of time series (1958-1977) are used from 1850 to 1949. For 1950 - 1957 the years 1958 - 1965 in the time series are used. Starting from 1958 one full cycle is used until the end of the run. This solution has both inter-annual variability and relatively small temperature jumps compared to repeated full cycles (see figure 12)

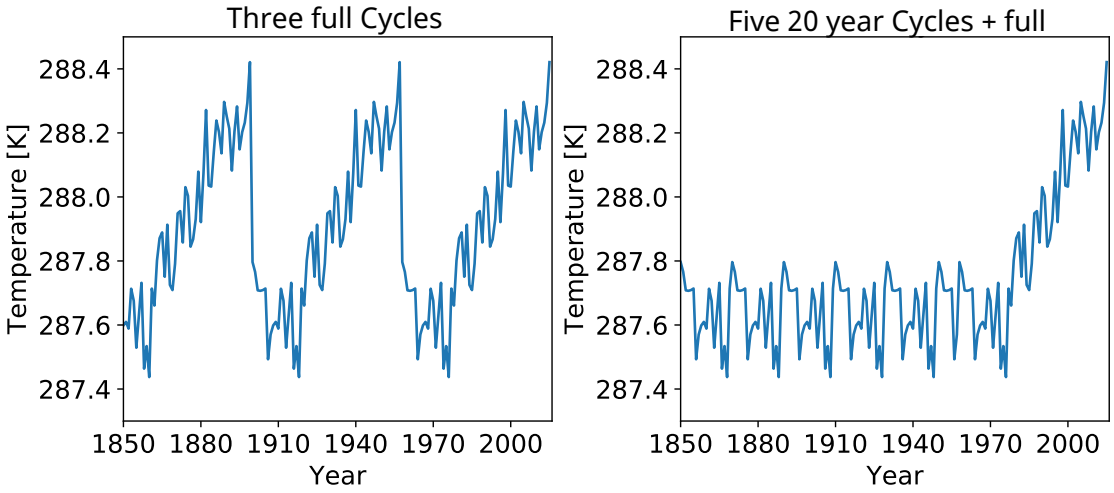

Figure 12: Comparing global annual surface air mean temperature for three full cycles of JRA (left side) to the option we used: five 20 years cycles + one full cycle (right side)

For the isotopic boundary condition, the time series described in section 2 are used. These time series by Graven et al. (2017) start in 1850. The isotopic files contain $\Delta^{14}C$, as mentioned in section 5.1.3, the model expects $\delta^{14}C$. Therefore the time series was adjusted, using equation 22 to calculate $\delta^{14}C$ from $\Delta^{14}C$ and $\delta^{13}C$. The transient $\delta^{13}C$ values from the Graven et al. (2017) time series were used in this calculation.

All oceanic variables are initialized by using the model output from the end of the spin-up (year 1350). Using the spin-up conditions as a starting point also implies that all the drift remains in the system. The drift or trend still in the system at the end of the spin-up therefore influences the industrial period simulation. To correct for this drift the control run described in section 5.2.1 is used.

5.2.1 Control

To analyse the industrial period simulation, discussed later (in section 5.2), a control run is helpful. The control run can be used to differentiate between changes induced by the remaining trend from the spin-up (section 6) or changes induced by the changing atmospheric conditions. Note that a control run does not eliminate the need for a spin-up that is almost in equilibrium.

The control run continues from the end of the ocean-only spin-up. It is run for 165 years. This is the same length as the industrial period simulation. Compared to the spin-up, it uses the same $\Delta^{14}C$, ^{13}C and CO_2, while it uses different climatic forcing. It uses between 1850 - 1958 JRA forcing as the industrial run. After 1958, further 20 year (forcing year 1958-1977) forcing cycles are used.

5.3 Land only spin-up

The land-only spin-up is performed for similar purposes as the ocean only simulation. The land needs to be in equilibrium with the atmospheric boundary conditions. This spin-up is the basis for future runs such as the industrial period simulation.

5.3.1 Boundary conditions

The values used for CO_2, $\delta^{13}C$, and $\Delta^{14}C$ are given in table 2. They are the same as the uncorrected ocean values. The land model expects $\Delta^{14}C$ as provided by Graven et al. (2017). The atmospheric

climate forcing differs from the ocean forcing set. For the land, required climate date go further back in time than for the ocean. The so-called GSWP3 (Global Soil Wetness Project) is a 0.5°, 3-hours resolution dataset specially designed to force land models. It is the forcing dataset recommended to be used for land-only model runs within the CMIP6. Data cover the period from 1901 to 2014. However, for the spin-up, we only use the years 1901-1920. With this inter-annual variability is captured, whereas clime trends are small compared to the second half of the 20th century.

5.3.2 Setup

Similar to the ocean spin-up, the land spin-up also starts from NCAR files(clmi.I1850Clm50Bgc Crop.1366-01-01.0.9x1.25 _gx1v6_simyr1850_c171213.nc). These files already contain the needed ^{14}C and ^{13}C, making it unnecessary for us to create initial fields for them as we did in the ocean only set-up. This eliminates one of the major problems in the set-up that was necessary for the ocean. The spin-up duration is shorter than for the ocean. We run the spin-up for 750 years instead of 1350 years. During this time no corrections were required, meaning the model was able to simply run consecutively.

5.4 Land control

The land control run is run for 165 years, the same length as the land industrial period simulations. The same boundary conditions as used for the spin-up continue to be used. This includes the 20 year forcing cycles, unlike the ocean-only control, the land control therefore keeps the atmospheric forcing from the spin-up. It starts at the end of the land spin-up at year 750.

5.5 Land industrial period

As the ocean-only industrial period simulation, the land-only industrial period simulation needs time-series of the relevant boundary conditions. The ocean and the land need time-series of atmospheric climate forcing, isotopic boundary condition and atmospheric CO_2. In addition to these data, the land industrial run also needs a series for the human land-use change as this greatly affects the capability of the land biosphere to store carbon.

The same atmospheric forcing series (GSWP3) as in the spin-up is continued to be used. From 1850 - 1901 cycles of the years, 1901-1920 are used as it was done in the spin-up. As the spin-up ended in 750 using forcing year 1910, the first year of the industrial period simulation uses 1911. Continuing to cycle afterwards leads to three cycles from 1850 - 1859 from 1860-1879 and from 1880-1899. 1900 uses forcing year 1901. From 1901 onward the forcing year matches the actual year.

The isotopic boundary conditions are the Graven et al. (2017) dataset, same used for the ocean industrial period simulation. Unlike the ocean, the land expects the input to be $\Delta^{14}C$ as the dataset provides. As a CO_2 time-series the previously discussed data from Meinshausen et al. (2016) is used.

The land use data set is based on the work of Lawrence et al. (2016). It prescribes for each plant functional type what fraction of each grid cell they occupy. This is done with a one-year resolution. So on each January 1st, the fraction of each cell covered by each PFT is adjusted (CLM).

This run starts at the end of the land spin-up, with its first year being named 1850. The values from the end of the spin-up year 750 are used as the start values at the beginning of the year 1850 of the industrial period simulation. The length of this simulation is 165 model years.

6 Model drift

Before analyzing the spin-up and comparing it to observational data, it is necessary to assess the trends in the spin-up. As stated before, at the end of the spin-up the model variables should be close to equilibrium with the given atmospheric conditions. Being in equilibrium should mean that these variables change very little in time, preferably they would be constant. Note that of course, even in equilibrium there could be some seasonal changes and some small inter-annual cycles.

Trends are generally to be avoided for the assessment of model responses to changes. Large trends would imply that the model results change a lot just from letting the model run longer. In our case, we do have a control run which allows us to separate model drift from forced changes. However, as it is very well possible that the trends in the system and the atmospheric induced changes combine in a non-linear way, it is still best to have trends as small as possible.

The drift present in our spin-up is illustrated in figure 13. The 100-year normalized trend from the period 1350 to 1300 was calculated by averaging the annual values from 1341-1350 and those from 1291 - 1300. These decadal averages are then subtracted and these results are multiplied by two. Not only the Δ^{14}C trend, the main focus of this thesis, but also trends in DIC, PO_4, δ^{13}C, ideal age, temperature, and salinity are presented.

The reason we analyze the 50 year period from 1300 to 1350 and not a 100yr period from 1250 to 1350 is the ^{14}C adjustment in 1250, discussed in section 5.1.3. The correction to the atmospheric δ^{14}C boundary leads to a slight readjustment afterwards which makes the surface trend immediately after 1250 very large. The trend from 1300 - 1250 shows larger changes of the surface values. For 1350 - 1300, the deep oceans changes in Δ^{14}C as well as for the other variables considered is almost the same as the 1250 - 1150 trend.

The Δ^{14}C trend in our model ranges between +1‰ to -4‰ per hundred years for globally horizontally averaged values (figure 13). On basin-wide averages, the Pacific shows even larger trends, from +3‰ to -5‰. Overall we see a positive trend in the upper ocean and a negative trend in the deep ocean. Although there are slight variations between the basins, at which depth the trend turns from positive to negative. Figure 14 provides trend for Δ^{14}C and δ^{13}C along a transect for the North Atlantic to the North Pacific. Trends are relatively independent of the latitude in the Atlantic. The Pacific on the other hand the trend is considerably larger at high northern latitudes than in the south. To assess whether or not a trend on the order of 0.01 ‰ year $^{-1}$ is large it is useful to discuss equilibrium criteria.

According to the OMIP equilibrium criteria, Orr et al. (2017) for Δ^{14}C, a drift of not more than 0.001‰ year^{-1} for 98% of the ocean volume should be achieved. The OMIP criteria is very strong. As mentioned before other simulations of the ocean with carbon isotopes enabled performed far longer spin-up. Even these simulations where not run long enough for the model to be in agreement with the OMIP criteria. Jahn et al. (2015), who implemented carbon isotopes in CESM, decided to weaken the equilibrium criteria by factor 10. Their model showed less than 0.01‰ year^{-1} for 98% of the ocean, Jahn et al. (2015) decided that this was satisfactory for their goals.

Our simulation is clearly not in equilibrium for Δ^{14}C according to the OMIP criteria and not even with the weakened criteria proposed by Jahn et al. (2015). Despite this we did not continue the spin-up, the main reason for this is that we lacked computational resources to run for an unknown number of additional years. Keep in mind, we were only able to run 13 model years in one calendar day, meaning that running the model for 1350 years already took over three months. We run a control simulation to mitigate the problems with the trend, further, the atmospheric Δ^{14}C change over the historical period is very large. This large atmospheric change likely induces such a large change in the ocean that the trend would be orders of magnitudes smaller than the induced change.

For five out of the other six variables (DIC,PO_4,δ^{13}C, temperature and salinity) the trends (figure 13) are relatively small. Although table 4 shows that there are in all variables single cells with very high trends. For instance, there is one cell that changes its temperature by 0.87 °C while the mean change was just 0.03 °C. However, since most of our analysis is not focused on single cells this should not matter.

The one variable which is likely not at all in equilibrium is the ideal age. The trend in the ideal age is very large. At a depth of 2000m, the Pacific basin average ideal age trend is roughly 60 years per 100 years. This is four times larger than the age trend inferred from the Δ^{14}C trend (2‰ means roughly 16 years). At singular grid cells, the trend is even larger, up to 137 years change of ideal age in the studied 50 year period. Such a large single-cell trend may come from

changed circulation. From this large trend, we conclude that it does not make any sense to study the ideal age distribution any further. This also means, we cannot investigate the complex carbon age to ideal age relationship, as discussed in section 2.6.

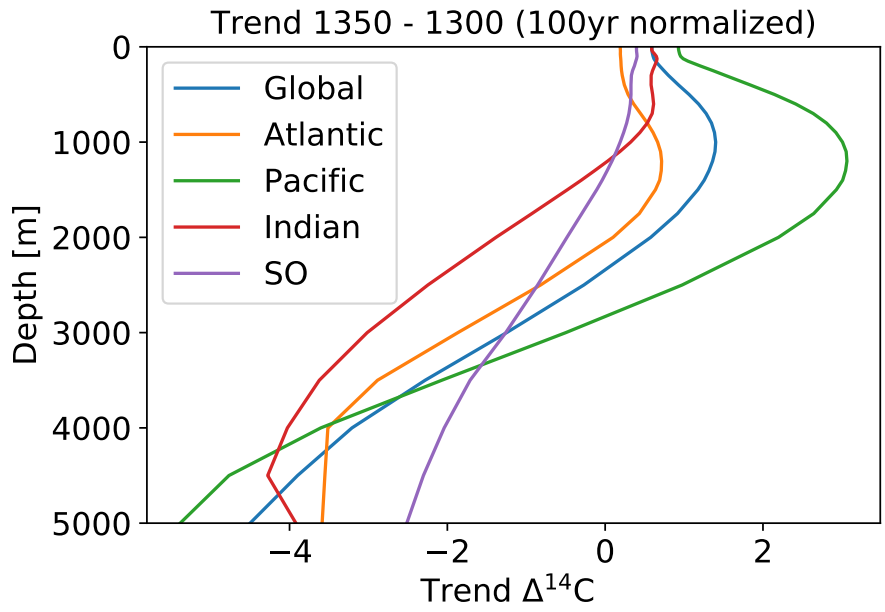

(a)

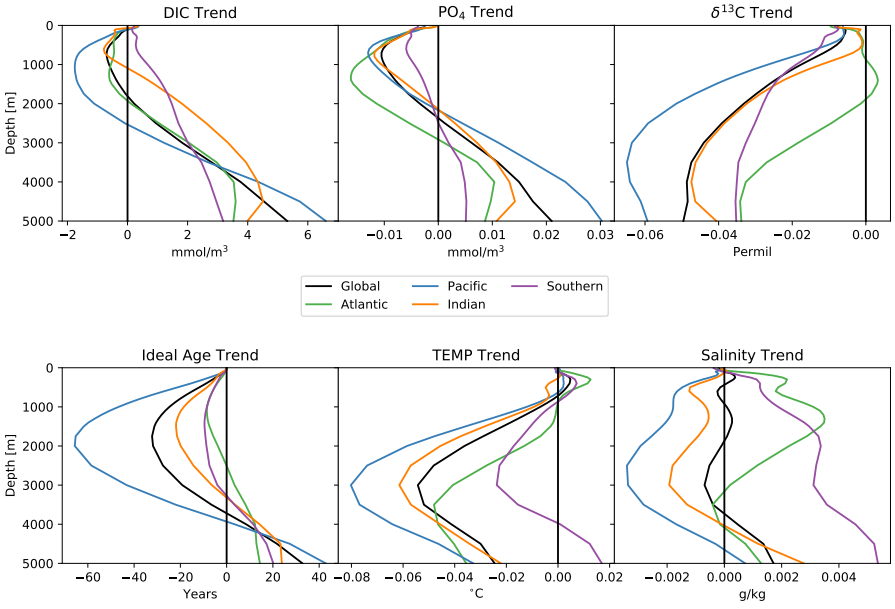

(b)

Figure 13: Trends between model years 1350 and 1300 for Δ^{14}C, DIC, PO4 given per hundred years. (e.g, ‰/100yr for Δ^{14}C)

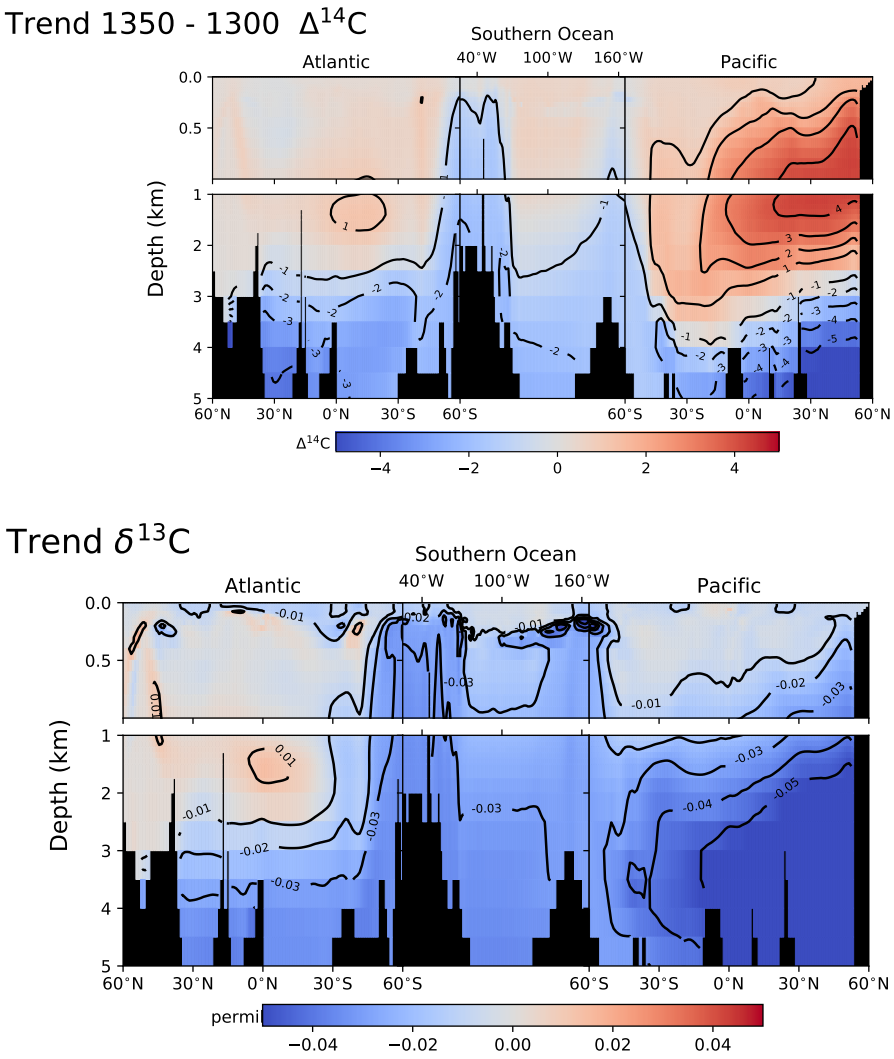

Figure 14: Trend between model year and 1350 - 1300 for Δ^{14}C,DIC,PO4 given in ‰ change per hundred years.

Variable	Flux	Mean Trend	Absolute Mean	MaxTrend
Δ^{14}C [‰]	382 kmol	-0.32	1.63	-13.1
DIC [mmol/m^3]	0.59 PgC/yr	0.93	1.88	33.9
PO_4 [mmol/m^3]	-	0.00019	0.009	0.16
δ^{13}C [‰]	13852 kmol	-0.028	0.028	-0.21
Ideal Age [years]	-	-13.7	20.9	-137
TEMP [°C]	-	-0.025	0.03	-0.87
Salinity [g/kg]	-	-0.00003	0.0025	0.6

Table 4: Global mean trend, absolute global mean trend and max trend. Absolute Mean trend is the average of the absolute values of the trend, while max trend gives the highest trend, in terms of absolute value, found in any grid cell. Multiplying the mean trend by the ocean volume gives the inventory change, where applicable

7 Preindustrial tracer distribution: model versus observations

In this section, the model results obtained from the ocean-only spin-up simulation are compared to observational data. DIC, PO_4, $\delta^{13}C$ and $\Delta^{14}C$ are compared with an emphasis on $\Delta^{14}C$. DIC and $\Delta^{14}C$ observational data are from GLODAP(Key et al. (2004)), $\delta^{13}C$ observational data are from Eide et al. (2017) and PO_4 is from the World Ocean Atlas (Garcia et al. (2013))

7.1 Basin average distribution

Figure 15 shows the basin-wide average model results compared to observational profiles. For all the variables, major differences and matches to the observational results are in similar locations. First, observed average surface distribution is represented fairly well. A notable exception is PO_4 in the Southern Ocean; surface concentrations are 1 mmol/m^3 in the model and 1.5 mmol/m^3 in the observations. PO_4 in the Southern Ocean is consistently too low in the model at all depths. Second, the gradient with typically highest $\Delta^{14}C$ values in the Atlantic, followed by intermediate $\Delta^{14}C$ values in the Southern Ocean, low values in the Indian Ocean and highly depleted $\Delta^{14}C$ in the Pacific is represented in the model. Third, the model does capture the distribution of all variables to some degree. For instance, all basin-wide DIC distributions are within ±10% of the observed values.

There are two general mismatches in the model results when compared to the observations. First, the model produces more pronounced minima/maxima. For example, in the Indian Ocean, the model reaches a minimum $\Delta^{14}C$ value at 3000 m depth with -208‰. Until the depth of 5000 m ^{14}C is getting enriched leading to a $\Delta^{14}C$ value of -187‰. Observations do not show such a clear minimum. According to the observation-based GLODAP product, $\Delta^{14}C$ in the Indian Ocean is -194‰ at 3000 m depth and -190‰ at 5000 m depth, meaning there is only a very small minimum in the observations.

The second mismatch is that the model reproduces the observational values poorly in the deep Pacific. Across all four variables, all of them show the largest observation-to-model differences in the deep Pacific. For example, the difference for $\Delta^{14}C$ between the model and the observations is more than 50‰ in the Pacific at depths between 2000 and 3000 m. At a depth of 5000 m the mismatch is smaller, but still, 25‰. The cause of this large mismatch is likely a too small influx of water into the Pacific ocean from the Southern ocean.

Regarding $\delta^{13}C$, the model shows similar behaviour for all basins in the top 200m. $\delta^{13}C$ increases by roughly 2 ‰ between 200m and the surface. This gradient is much larger than observed below 200m. Unfortunately Eide et al. (2017) dataset does not cover the top 200m.

The differences between the model $\delta^{13}C$ distribution and the observed data from Eide et al. (2017) are of particular interest. The $\delta^{13}C$ values of the model were initialized at the beginning of the spin-up with the Eide et al. (2017) dataset. During the spin-up, these values changed resulting in the differences, seen in figure 15. This means the dataset distribution was not in equilibrium for the model. Since the top 200m were missing it would have been surprising, if the model was in equilibrium. The assumption of no vertical gradient for the top 200m, as used in the initialization, is false. Therefore it would have been wiser to assume a different profile for the top 200m.

Temperature and salinity are represented by the model, especially when compared to the other four variables. Surface temperatures match observations nearly perfectly, while in the deeper ocean all profiles show a too low model temperature. Salinity shows deviations at around 1 km depth similar to the other variables albeit that these deviations are smaller than in other variables.

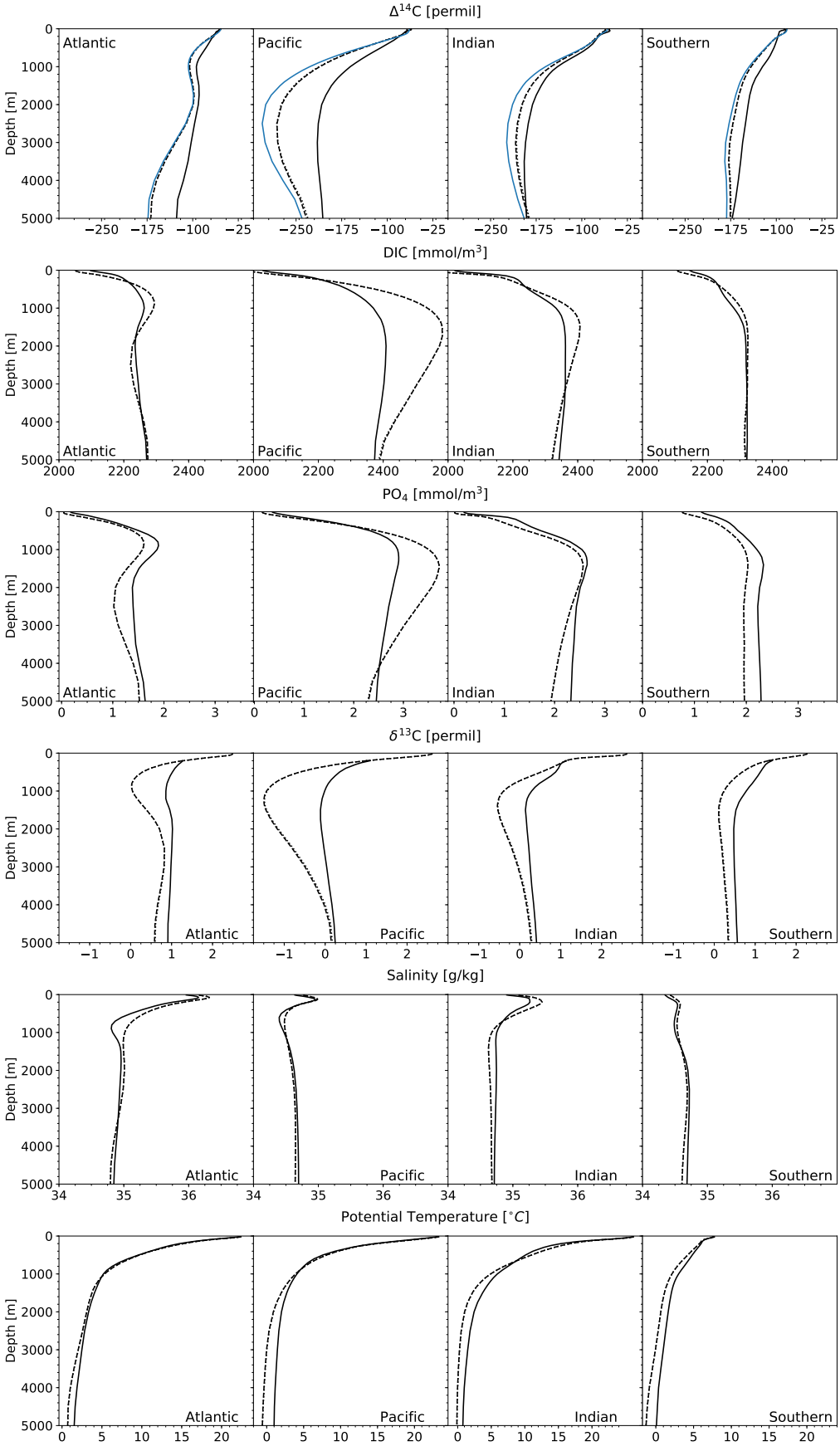

Figure 15: Basin average depth profiles for Δ^{14}C, DIC, PO_4, δ^{13}C, salinity and potential temperature. Regions are defined according to figure 11. Dotted line are model results, solid lines are observational data. Δ^{14}C and δ^{13}C are corrected to preindustrial values, all other variables are modern measurements. Blue line in Δ^{14}C shows abiotic Δ^{14}C values from the model.

7.2 Spatial distribution

The previously discussed basin average profiles showed the general mismatches between the observations and the model. Yet it obscures small scale mismatches within these basins. Leading us for example to believe that most variables are well matched on the surface, when in fact there are considerable differences to the observations. These basin plots also show us how similar the distribution patterns of these four variables are.

The model results for the surface ocean $\Delta^{14}C$ well represent the observed surface ocean $\Delta^{14}C$. In figure 16 one can see the modeled surface $\Delta^{14}C$ and in figure 17 the observed - modeled $\Delta^{14}C$ values are shown. Two-thirds of all surface grid cells show less than 10 ‰ difference to the observational values. These differences of 10‰ are small when compared to the overall surface $\Delta^{14}C$ gradient which is about 100‰ in both the model and the observed values. Additionally, the differences show no uniform sign, there are large regions too depleted in $\Delta^{14}C$ and regions too enriched in $\Delta^{14}C$ when comparing the model to the observations. Furthermore, for this comparison (figure 16,17) the measurements were corrected for the influence of excess radiocarbon. This adds uncertainty to the observation-based preindustrial $\Delta^{14}C$ distribution. In light of these factors, we conclude that the model represents the observed $\Delta^{14}C$ distribution pretty well.

With the observational data-sets we are using, it is not possible to make any discussion about the surface model to observation differences for both DIC and $\delta^{13}C$. DIC observations are not corrected for anthropogenic influence over the industrial period and $\delta^{13}C$ observations have no data for the top 200 m. However PO_4 can be evaluated. In both observations and model results, we see that most of the ocean is nearly completely depleted in PO_4. However, some regions where PO_4 is not depleted exist, namely the Southern Ocean, the eastern equatorial Pacific and northern Pacific. In these regions, PO_4 values from the model results are lower than observational values. These differences are substantial, with differences of up to 0.75 mmol/m^3. This leads to the model showing a smaller total surface PO_4 gradient than the observations.

The relatively well-matched surface $\Delta^{14}C$ is in contrast to the large mismatch in the deeper ocean (figure 16 - 19). $\Delta^{14}C$ is well represented by the model in the top 200 m whereas large differences between model and observations are found in the deep Atlantic below 3 km and the deeper Pacific. The Southern Ocean below one kilometer depth shows a consistent observation-to-model difference of about 20‰. On the other hand, both the deepest Atlantic (below 3km) and the deep Pacific (below 1 km) show a gradient in differences with larger differences further north. Deviations exceed 60‰ in many grid cells in the Pacific. Both of these areas are ventilated by Antarctic bottom water which itself is mismatched to the observations by about 20 ‰. These results suggest that the ventilation of the Pacific and Antarctic Bottom Water in the Atlantic is too sluggish

DIC and $\delta^{13}C$ show very similar mismatch patterns, albeit with of opposite sign. Modelled DIC is too high and modelled $\delta^{13}C$ too low in the entire Pacific (below 500m). Differences of up to -120 mmol/m^3 in DIC and +1.2‰ in $\delta^{13}C$ can be found. Deviations are largest around the equator. Deviations in the Atlantic are confined to the first km, the rest of the Atlantic is well matched. The entirety of the Southern ocean is well matched to observations in both $\delta^{13}C$ and DIC.

PO_4 differs from the other three variables, in that it is not exchanged with the atmosphere and therefore has a fixed inventory across the ocean. Like the other three variables, the largest mismatches between observational data and model results are found in the deep Pacific. Between 30°S and 60°N in 0.5 - 3 km depth the model results shown PO_4 values about 0.6 mmol/m^3 lower than observational data. Because of the fixed inventory, this too low modelled inventory has to be balanced, which leads to the rest of the ocean generally showing higher PO_4 values in the model results than in observational data.

To summarize the findings, $\Delta^{14}C$ and PO_4 in the surface ocean are in agreement with observational data. The observations in the deep Pacific, especially between 30° S - 60° N and 1-3 km depth, are poorly matched in all four variables. Likely this is linked to a too-small inflow of Southern Ocean water into the Pacific. If the Southern Ocean is mismatched this mismatch is fairly constant. The Atlantic shows no consistent picture for the four variable.

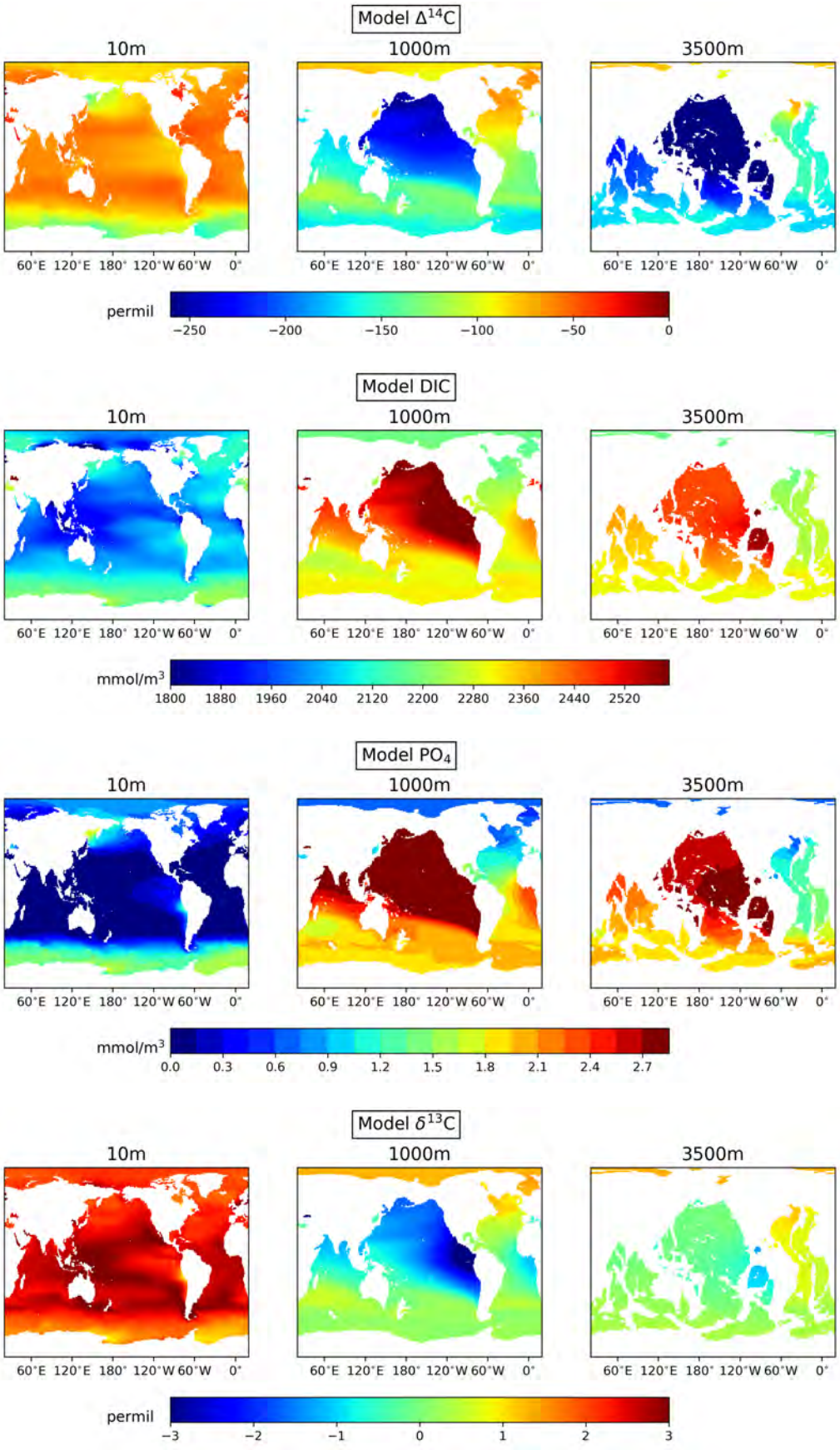

Figure 16: Maps of model results for DIC (GLODAP Key et al. (2004)), δ^{13}C (Eide et al. (2017)), Δ^{14}C (GLODAP Key et al. (2004)), PO_4 (World Ocean Atlas 2013), note that δ^{13}C and Δ^{14}C are corrected to pre-industrial values. Model data used are from the year 1350 of SPIN_OC.

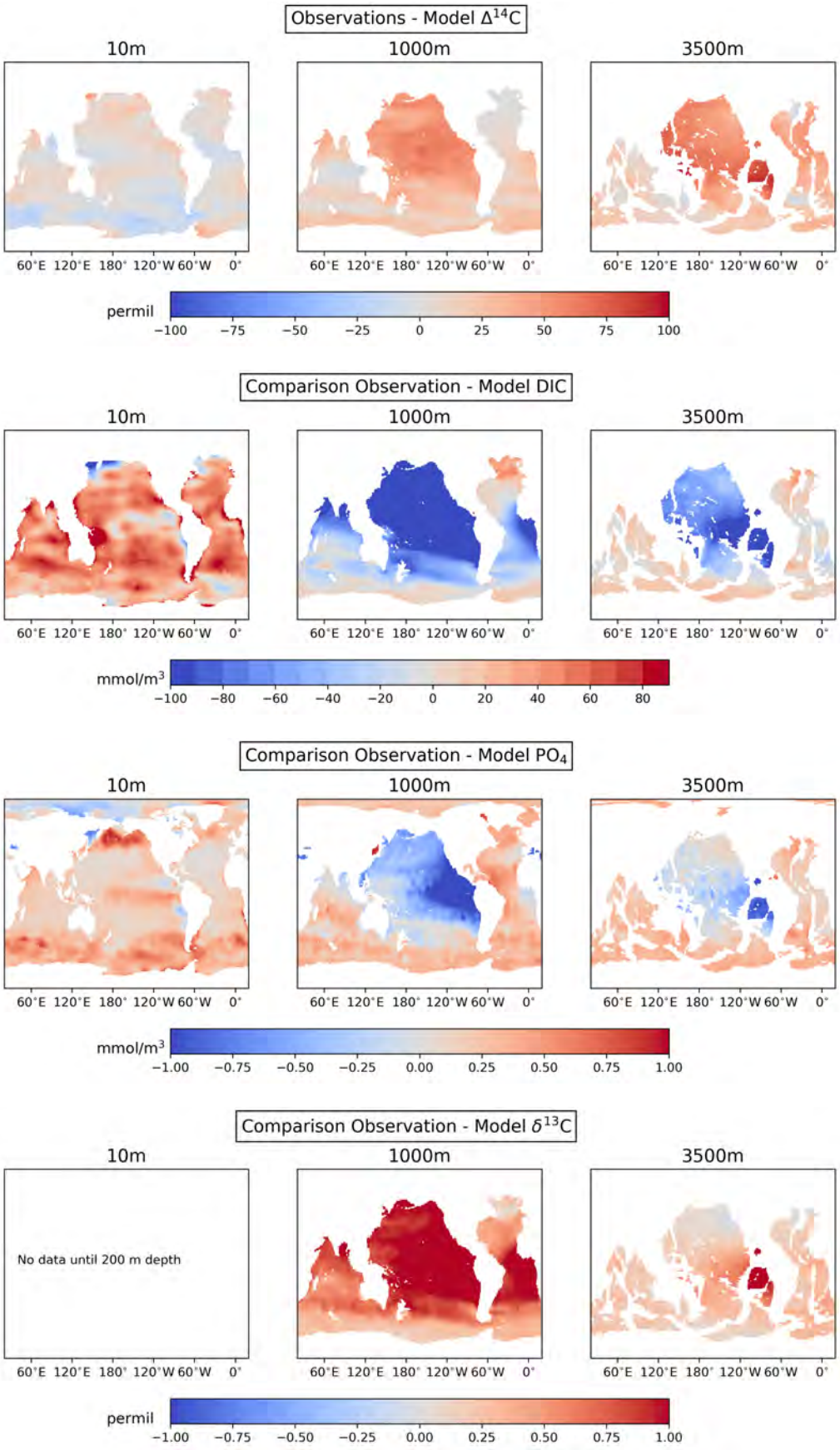

Figure 17: Maps of Observation - Model for DIC (GLODAP Key et al. (2004)), δ^{13}C (Eide et al. (2017)), Δ^{14}C (GLODAP Key et al. (2004)), PO_4 (World Ocean Atlas 2013), note that δ^{13}C and Δ^{14}C are corrected to pre-industrial values. Model data used are from the year 1350 of SPIN_OC.

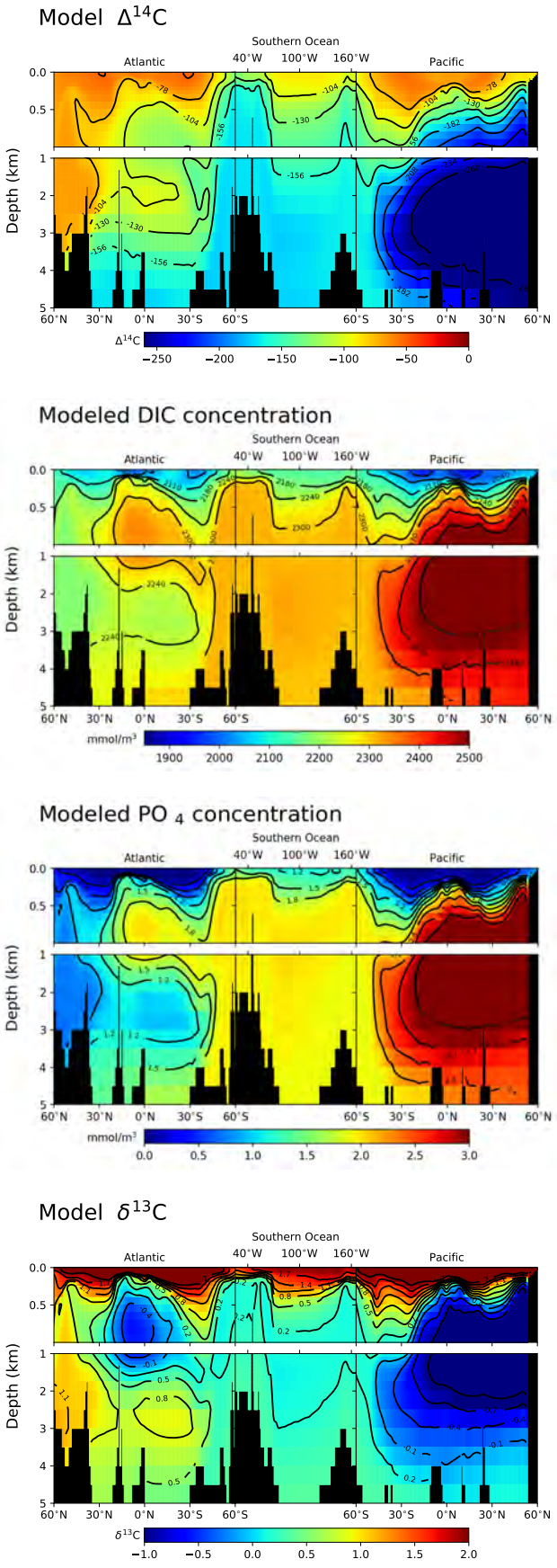

Figure 18: Modeled Sections of $\Delta^{14}C$ DIC, PO_4 and $\delta^{13}C$ following the path seen in figure 11

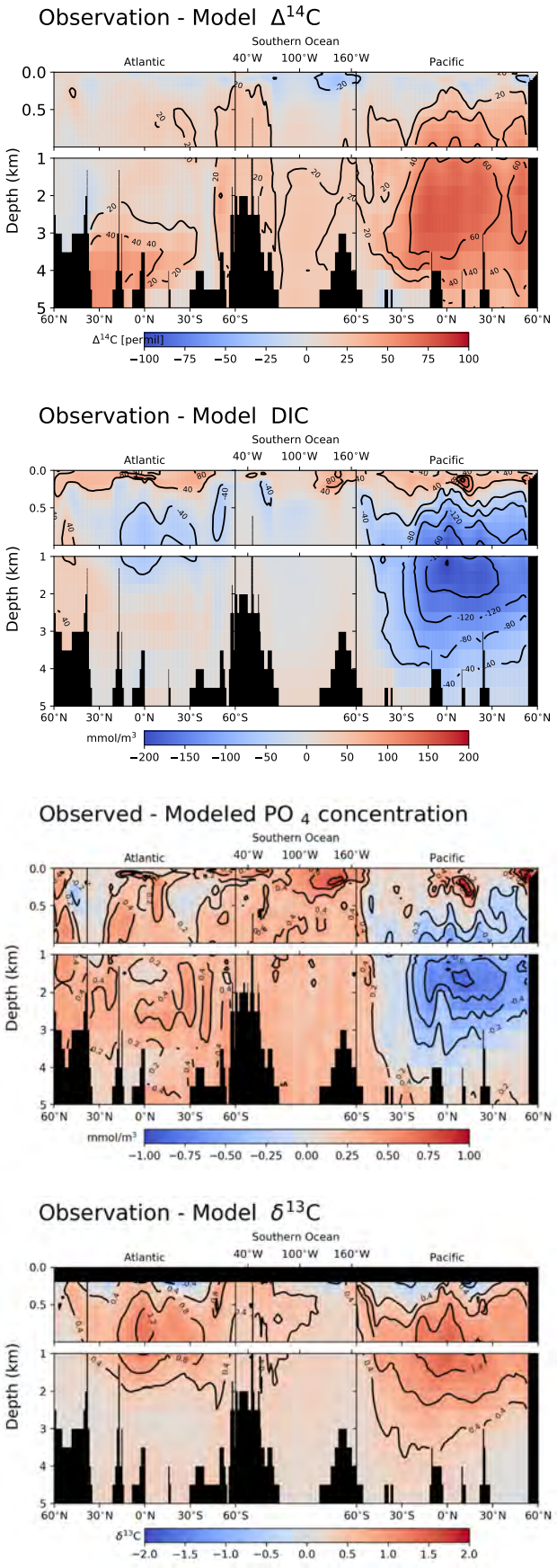

Figure 19: Observed - Modeled Sections of $\Delta^{14}C$ DIC, PO_4 and $\delta^{13}C$ following the path seen in figure 11

7.3 Property - property analysis

Mismatches between the observations and the model can be unrelated or not. With a property-property plot as shown in 20, one can see the correlation between these different observation to model differences. If mismatches are correlated, it is to be assumed that they are caused by the same problem.

The correlation of model to observation errors in different variables can be seen in figure 20. Differences are taken for each cell between the observational data and the regridded modelled data. The results from this comparison show that these differences show a widespread in all basins. Generally speaking, the Pacific shows both the largest error spread and the largest errors. The Indian ocean is omitted from the plot as it shows no new information compared to the other oceans.

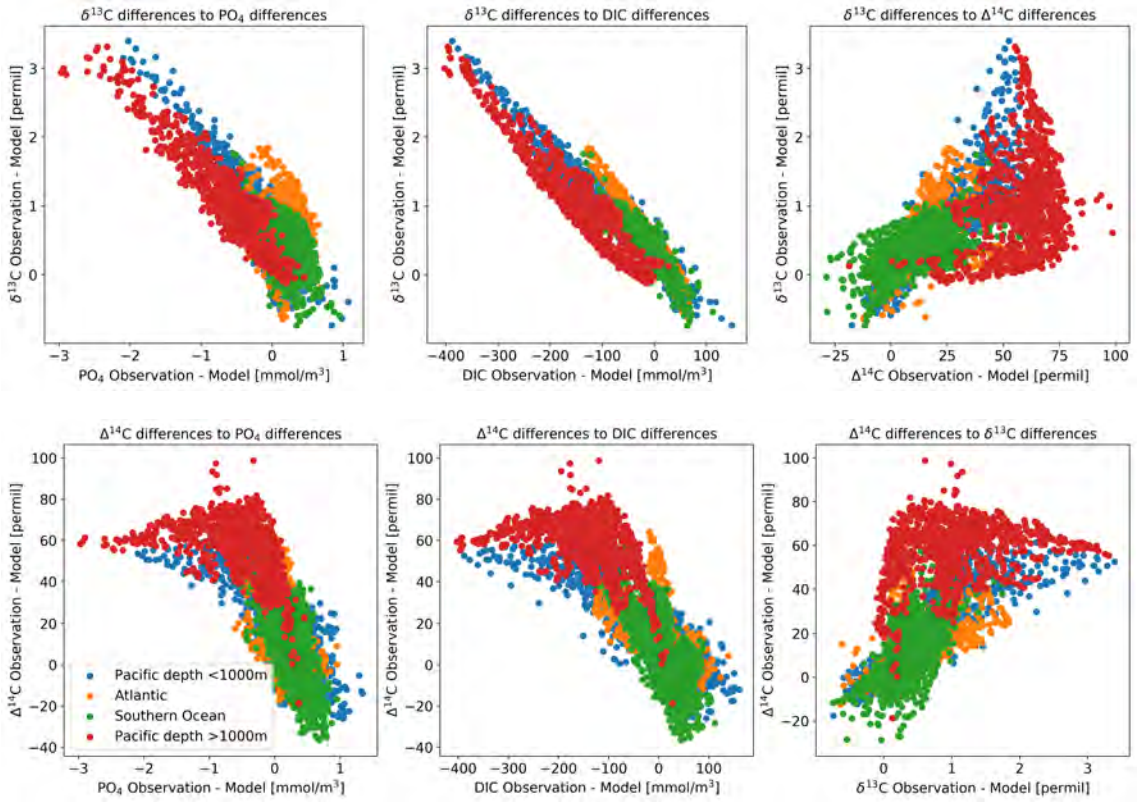

Figure 20: Observed - modeled property-property plot for cell differences.

The observational to model differences in δ^{13}C are closely correlated to the difference in DIC and PO_4. For example, DIC shows differences to the observations of up to -400 mmol/m^3, while ^{13}C shows differences from -1‰ to 3‰. The differences are roughly linearly related with -125mmol/m^3 DIC/1 ‰ δ^{13}C. This correlation holds true in all ocean basins, although the slope is slightly different in different basins. The correlation between DIC, PO_4 and ^{13}C can be explained by the fact that their distributions are influenced by the same factors. DIC and ^{13}C in particular, are correlated because of the fractionation occurring during the organic matter build-up, as the build-up of organic matter favours ^{12}C.

The correlation between DIC,δ^{13}C and PO_4 with Δ^{14}C is considerably weaker. The reason for this is most likely the additional control mechanism in the Δ^{14}C distribution, i.e. time or water age. While time also plays a role in the distribution of the other three variables, it is the dominant factor for Δ^{14}C. The correlation is the weakest in the Pacific. This weaker Pacific error correlation is evident both in the upper (<1000m) and deep (>1000m) Pacific.

The weak Pacific correlation is likely the result of the strong Pacific distribution maximum/ minimum seen in the four variables (figure 15). This maximum/minimum is located between 1000 and 2000 m for DIC,PO_4 and ^{13}C. In Δ^{14}C it is further down at a depth of 2000 to 3000 m.

The fact that Δ^{14}C mismatches are in some areas not correlated with DIC mismatches is a valuable result. As it shows us that looking at Δ^{14}C in addition to for example DIC can be

worthwhile. Because as the errors are sometimes uncorrelated, they are caused by something else and this variable can thereby be used to test additional model properties. The high correlation of δ^{13}C mismatches with DIC mismatches, on the other hand, could mean that they show the same thing. Meaning that if one is not directly interested in δ^{13}C it is likely less ideal as an additional model constraint as Δ^{14}C, at least for an ocean model.

8 Industrial period simulation

For the spin-up simulation, the main interest is the end of the spin-up since this is the state presumed to be in equilibrium. The industrial period simulation is a transient simulation where the focus is on the changes occurring over time.

8.1 Basin wide impact

Figure 21 shows the basin-averaged depth Δ^{14}C profiles for the major ocean, for the years 1975, 1995 of the historical run IND_OC and the year 1495 of the Ctrl_OC. On average the surface ocean is enriched by more than 100‰ when comparing 1995 to 1495. In general, this means that the surface to deep ocean gradient is much bigger in 1995 than in the corresponding control year 1495.

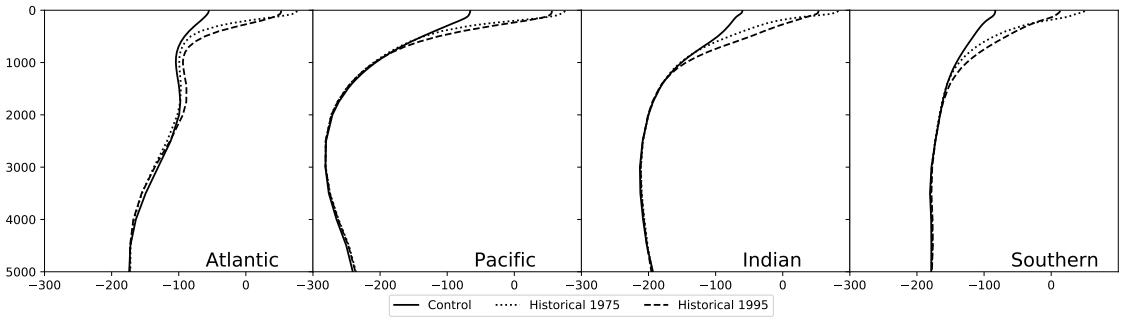

Figure 21: Depth Δ^{14}C profiles for the different ocean basins at the year 1995 in the historical period simulation IND_OC (dashed line) (1975,dotted line), and the respective year (1495) in the control run (solid line)

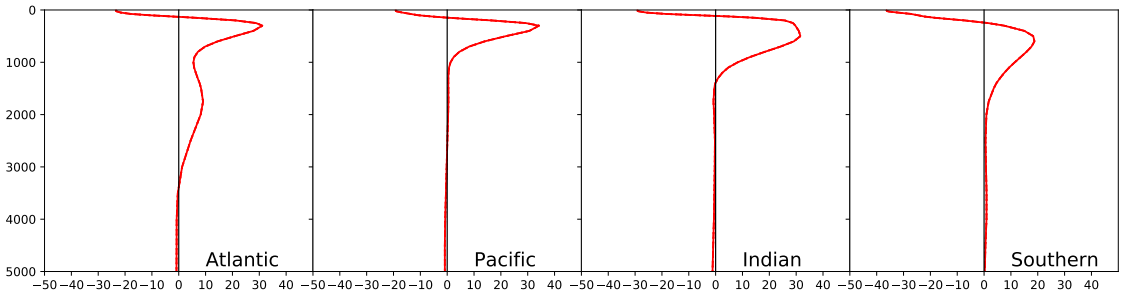

Figure 22: Basin wide average change in Δ^{14}C from 1995 - 1975, positive numbers meaning larger Δ^{14}C in 1995.

In section 2.4.2 it is stated that the bomb radiocarbon only affects the upper ocean. To determine how deep bomb radiocarbon penetrated the ocean within the model, the Δ^{14}C distribution of the control is compared to the Δ^{14}C distribution of the industrial period simulation. Globally the bomb radiocarbon has changed Δ^{14}C in the first 500 m to 1000 m of the surface ocean. The depth at which the effect of the bomb radiocarbon becomes 0 is basin dependent. In the Atlantic, this depth is more than 2000 m while it is only 800 m in the Pacific.

At depth between 3000 m and 4000 m, the Atlantic Δ^{14}C is enriched in the control run compared to the historical period simulation (see figure 21). There are two possible reasons for this. The trend still in the system at the end of the spin-up effected the Atlantic in the control and historical simulation differently. However, this seems unlikely as the other basins closely match the control run. The second reason might be the propagation of the Suess effect into these depths in the Atlantic.

While the change in basin-average Δ^{14}C in the Atlantic at depth of 3000m is very small as seen in figure 21, a transect (figure 23) shows a different picture. It becomes evident that the Atlantic north of 30° is strongly enriched in bomb radiocarbon with Δ^{14}C changes of over 30‰.

This strong change in this particular region is unsurprising as it is also the region with the highest $\Delta^{14}C$ levels in the deep ocean, indicating a rapid surface-to-deep surface.

Unlike the Atlantic, the other basins reveal no large change in depths greater than 1000m. Certain cells show slight changes, however, these are so small that it is more probable that they are linked to the drift rather than the bomb radiocarbon influence.

However, there are substantial differences in $\Delta^{14}C$ between the years 1975 and 1995. The 1975 profile shows larger $\Delta^{14}C$ values at the surface. Between 1975 and 1995 the radiocarbon is redistributed from the surface to deeper layers reducing the surface-to-deep ocean gradient.

$\Delta^{14}C$ decreases by up to -40‰ in the first 100 m of depth across all basins. This is a substantial change but is overall still much smaller than the total change during the industrial period. Below 100 m $\Delta^{14}C$ increased, with the change peaking around 500 m with a magnitude of roughly 30‰. Only the Atlantic shows changes deeper than 1000 m below surface.

Datasets such as GLODAP need to separate the bomb radiocarbon from the natural radiocarbon. In the GLODAP dataset bomb-radiocarbon was only calculated for the top 1500 m. This means below 1500 m the measured signal was assumed to be natural. Key et al. (2004) decided that the method used was unreliable for depths greater than 1500 m. For the model, the bomb radiocarbon is found deeper than 1500 m in the Atlantic, as stated before. Not calculating radiocarbon to sufficient depth can explain some of the offset in the deep Atlantic in the spin-up to observation comparison.

The bomb radiocarbon distribution calculated with the GLODAP method is substantially different from the one calculated by the model (figure 23). GLODAP only calculates bomb radiocarbon for the top 1500m. The uptake according to GLODAP in the top first 1500 m seems to be considerably larger than in the model run. In the Southern Ocean, GLODAP and simulated values match each other. In the rest, of the ocean GLODAP suggests the rise in radiocarbon to be up to 40‰ $\Delta^{14}C$ higher than the model.

While this could mean that the model has errors, it can also be an error in the GLODAP dataset. GLODAP data was collected over a long period of time and at the end, no correction was applied to normalize the data to a reference year. In the bomb radiocarbon distribution, this might have affected the quality of the product. Considering how much the surface radiocarbon changes from 1975 to 1995, temporal sampling could have a huge impact. This error does not influence the natural radiocarbon calculation, as the method used to separate bomb and natural $\Delta^{14}C$ is applicable to samples from different time periods.

The 1500 m cutoff seems to have no large effect. Our model results also do not show any bomb radiocarbon below 1500 m. However, there is one notable exception which is in the deep North Atlantic. Interestingly, in comparison to the spin-up results to the observations (section 7.2), we saw that observed $\Delta^{14}C$ values in this particular area of the North Atlantic are well-matched by the model. Reducing the observed natural $\Delta^{14}C$ by 30‰ would mean our model shows a too high $\Delta^{14}C$ there. This is interesting as throughout the deep ocean our model is too low in $\Delta^{14}C$. With this proposed reduction the north Atlantic would become the only region where the model shows too high $\Delta^{14}C$ values.

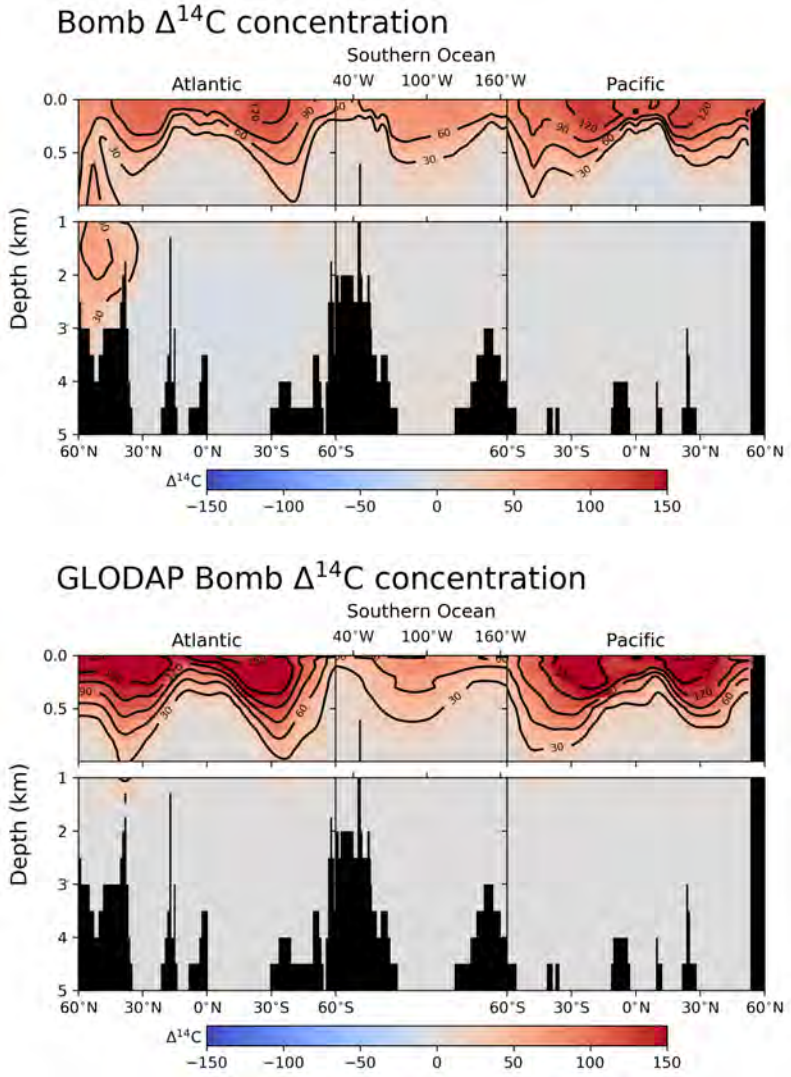

Figure 23: Top: The difference in $\Delta^{14}C$ between the industrial period simulation (IND_OC) year 1995 and the control run (Ctrl_OC) year 1495. Note that the $\Delta^{14}C$ distribution in 1495 at the control run is very similar to the end of the spin-up. Section along the red line in figure 11 Bottom: Bomb radiocarbon distribution from the GLODAP dataset

8.2 Comparison of model results with $\Delta^{14}C$ measurements in corals

With the previous analysis of the 1995 state, the temporal evolution of the oceanic $\Delta^{14}C$ change is missing. The raise in ^{14}C content in the surface ocean was not happening simultaneously across the global ocean. This can be seen in coral records, which show the year to year evolution of the $\Delta^{14}C$ of their surrounding water. Coral records collected in the North Atlantic show that depending on the exact location the oceanic response to the rise in atmospheric radiocarbon content differs in magnitude and timing.

Dentith et al. (2019) compiled data from corals samples from twelve locations and different original sources. In figure 24, those samples are compared to the industrial period ocean only results. These twelve $\Delta^{14}C$ time series differ in amplitude and timing of their respective response to the atmospheric $\Delta^{14}C$ peak. Most of the samples are from the top 100 m but two of them also provide corals from deeper layers at the same location. All series start around the 1950s with $\Delta^{14}C$ at -60‰. However, while some samples cover the 1990s or early 2000s, other series end in the 1980s.

German Bight and Oyster Ground (corals 5 and 6 in figure 24) are locations in the North Sea. Located at shallow waters near the coast of Europe (Dentith et al. (2019)). The radiocarbon content there is highly influenced by air-sea gas exchange with a smaller role of surface-to-deep

mixing. This leads to a fast increase of Δ^{14}C in the 1960s and a decrease afterwards. The model is able to reproduce this evolution. However, especially noticeable in the German Bight record, the model underestimates the amplitude of the signal. The Δ^{14}C changed from -60‰ to 213‰ according to observations. In the model the change is from -60‰ to 140‰. The timing of the Δ^{14}C increase in both the model and the observations seems to be similar.

Other coral locations, such as Grimsey (coral 2), show a different response to the atmospheric signal. The fast enrichment in the 1950s and 1960s (from -68 to +40‰) is followed by a levelling off of the Δ^{14}C. Only a small reduction is visible, -10‰ in 40 years. This behaviour is caused by these corals being part of the NADW formation zone which is better mixed. The model does capture this behaviour well. However, the modelled increase is much more confined in time than the data suggest. While the observations show an increase throughout the 1950s and 1960s the model results show an increase mainly between 1965 and 1968.

There are corals where data from both the surface and deeper in the ocean are available. In the Bermuda corals (coral 12) at the surface, for instance, we see similar behaviour to that of the German Bight coral. Meanwhile, deeper in the ocean, the increase comes much later, is of smaller magnitude and continues till the end of the record. The model shows some issues representing the surface corals at Bermuda, with an underestimation of the amplitude of the signal and some lag. However, the deep ocean behaviour is captured relatively well. The increase in radiocarbon starts in 1975 and continues to the end of the record.

Generally, overall corals, the model mostly underestimates the increase of Δ^{14}C. Especially in Tromso, Georges Bank and the surface Bermuda Coral, where the amplitude is up to 50‰ smaller in the model than the observations. But, one thing that needs to be pointed out is that the observational data seems to show a large spread, noticeable in Oyster Ground and Northeast Channel. Note that some of the spread comes from the fact that these samples where not all taken from the same coral. This spread makes it difficult to assess properly how well the model does represent Δ^{14}C of these corals.

A general problem, that did not seem to affect this comparison, was the lack of small scale data from the model. The model is run at a resolution of roughly 1° while these corals are found on one specific location. The same is true for the depth resolution, the model has 10m layers at the beginning with coarser resolution further down. To compare with the coral data, we, therefore, chose for each coral the grid cell and depth layer that best represented the depth and location. Luckily for us, these coral seem to originate from locations which are not highly influenced by small scale local phenomenon, so they seem to be able to represent their surrounding area quite nicely.

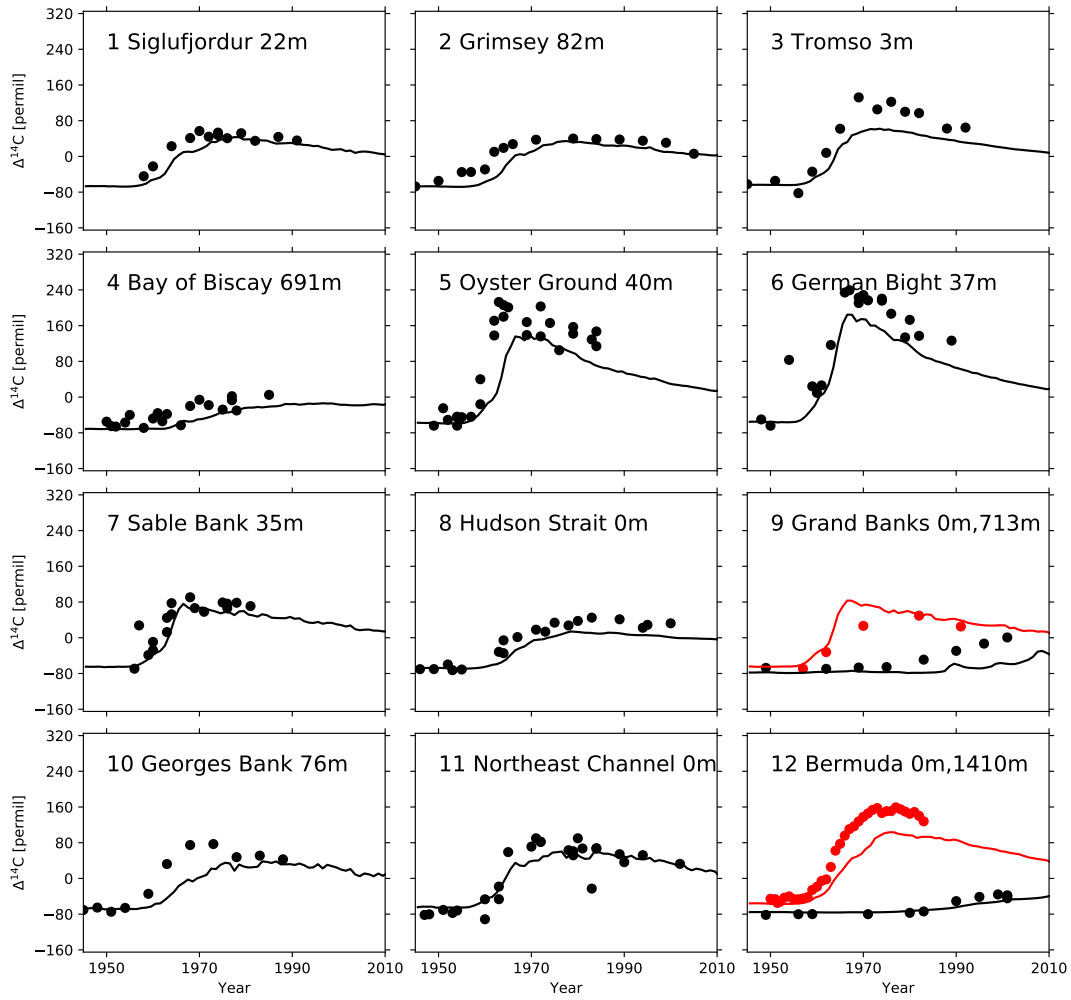

Figure 24: Different coral records (Black and red dots) compared to the CESM model industrial run (Black and red line). The numbers behind the name indicate the depth at which the coral record was collected. If two lines are present, the red line indicates the record from shallower water. Model data is retrieved from the grid cell containing the location of the coral sample

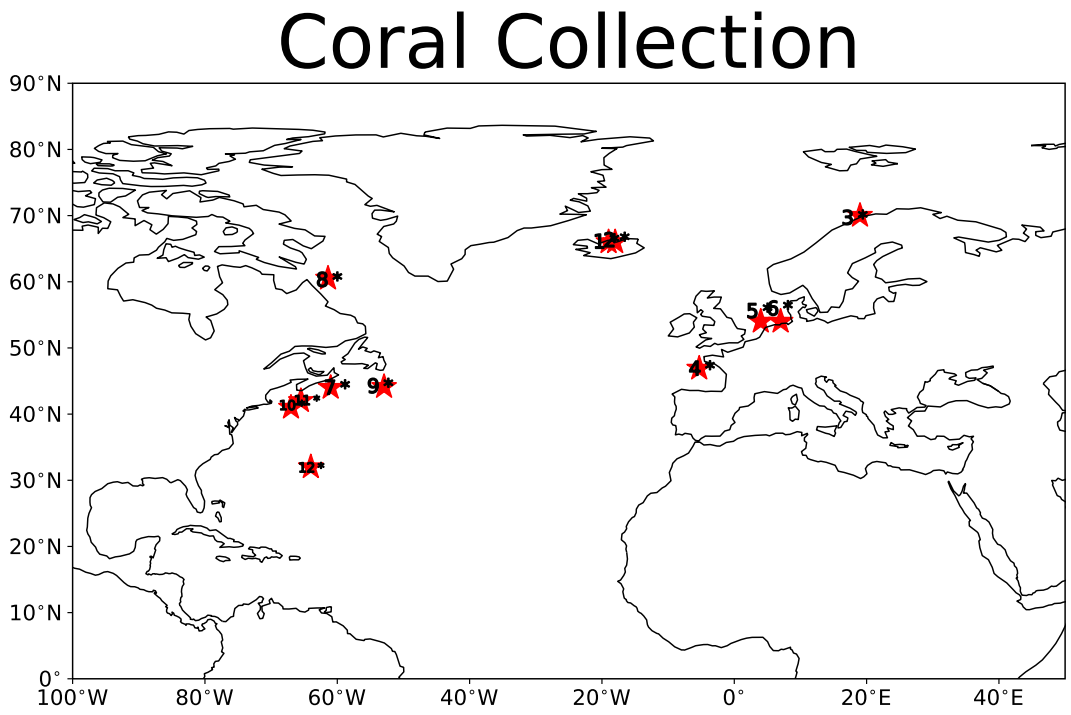

Figure 25: Sampling locations of the coral $\Delta^{14}C$ data shown in figure 24. Every number represents the coral profile with the same number on the left corner.

All previously discussed coral records are from the North Atlantic. A record from a coral of the shore of the Pacific island of Guam (collected by Andrews et al. (2016)), is seen in figure 26. There are two difference in this record compared to the previously discussed ones. Firstly, it is sampled at a higher frequency, multiple times a year instead of roughly once. Secondly, the record shows multiple peaks in $\Delta^{14}C$. For example, in 1955 the $\Delta^{14}C$ values increase from -50‰ to almost +1000‰ and after one year decrease again to -50‰. The width of this peak makes it clear that the higher sampling frequency is needed to capture this feature of the record. These peaks are the result of nuclear bomb test nearby and are not visible in Atlantic corals (Andrews et al. (2016)).

This coral record can be used to show one of the limitations of the current approach to simulating radiocarbon in the ocean. The atmospheric $\Delta^{14}C$ input used by the model is only given for three different latitudinal bands. Singular bomb tests which cause spikes in the coral record have no similar effect on the global atmospheric radiocarbon content. The model is able to recreate the general profile of the Guam coral record, again underestimating the amplitude slightly, but reproducing the peaks proves impossible. For this to be possible the ^{14}C production by nearby nuclear bomb tests would have to be modelled directly.

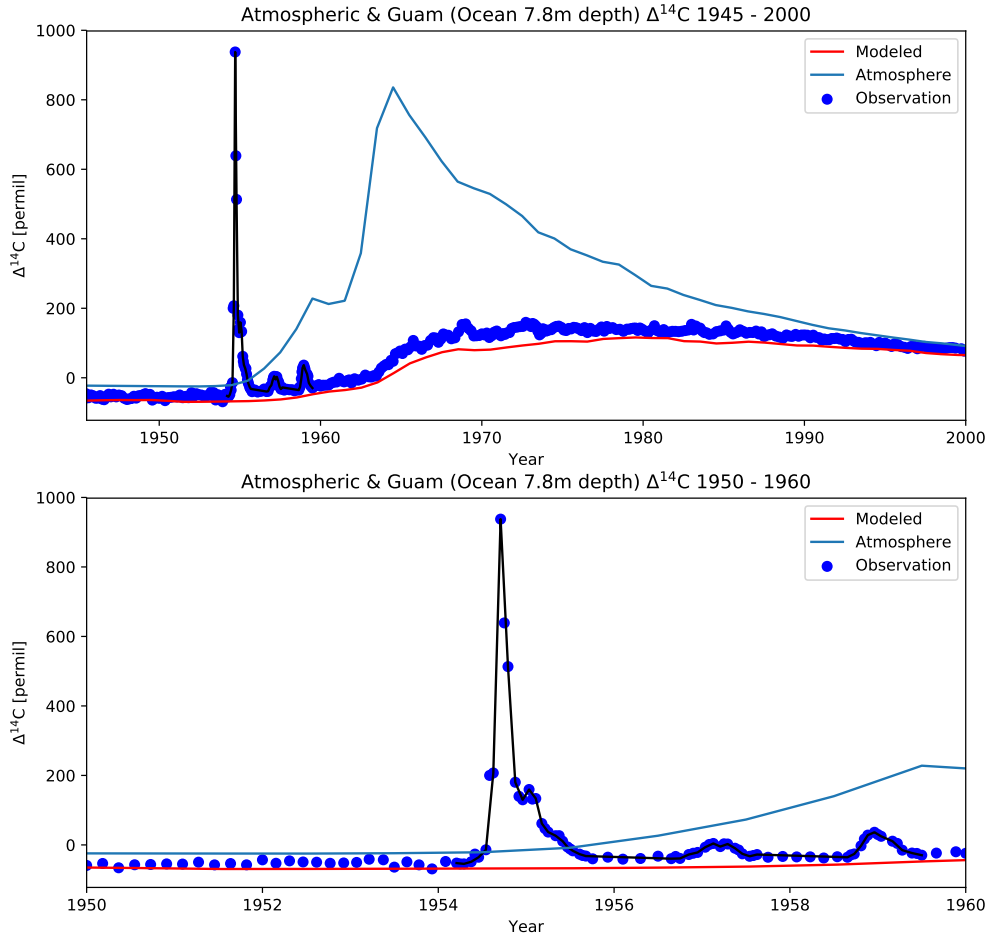

Figure 26: Coral record from the Pacific island Guam by Andrews et al. (2016). The three peaks in 1955, 1957 and 1959 are the result of nuclear bomb tests. The model misses to capture this feature.

8.3 The bomb inventory of the ocean

The bomb inventory, as defined in 2.4.2, is the additional radiocarbon stored in the ocean since 1945. For this analysis, this means the radiocarbon content of a specific year in the industrial period simulation is compared to the radiocarbon content of the year 1945 in the industrial period simulation. The radiocarbon content is solely calculated from the DIC - pool the other six-carbon pools are ignored in this assessment. Observational methods also only cover DIC, and other carbon pools are comparatively small.

Calculating the difference to any year in the control run instead of using 1945 in the industrial period simulation, leads to a lower bomb inventory by about 8 kmol. From 1850 - 1945 the ocean lost radiocarbon due to the Suess effect and radioactive decay. Taking a control run year as a reference year as oppose to 1945 of the industrial simulation adds this loss to the bomb inventory.

In figure 27 the bomb inventory calculated from our industrial period simulation (IND_OC) is shown. The bomb budget is negative until 1957. Each year until 1954 the ocean takes up less radiocarbon than it loses. The minimum value in 1954 is -0.7 kmol of excess radiocarbon. This is likely linked to the reduced $\Delta^{14}C$ in the atmosphere due to the Suess effect.

After the minimum is reached in 1954, the ocean starts to take up more radiocarbon. The increase starts small with 0.1 kmol in 1955, but by 1960 and throughout the 1960s and 1970s the

increase is larger than 1 kmol per year. In 1965 when atmospheric Δ^{14}C values are at its highest the ocean excess radiocarbon has increased by 3.4 kmol. This increase is caused by an increase in atmospheric values. These increases sum to 37.2 kmol of excess ^{14}C in 1975. Compared to the estimations collected by Naegler and Levin (2006), with their estimates ranging from 35.7-58.0 kmol, this is on the lower end of the estimates.

The increase slows down after the peak in 1965, being about 0.3 kmol/year in 1995. The total excess radiocarbon in 1995 is 52.7kmol. This falls outside the range of Naegler and Levin (2006) (54 - 59kmol). But when additionally considering the error of each of these estimates which is up 5 kmol, our results fall into the range. The uptake slows down likely due to two different reasons, one the atmospheric Δ^{14}C decreases and the previous uptake increases the surface ocean Δ^{14}C. Both of these two results in a lower ocean to atmosphere Δ^{14}C gradient, which reduces the uptake.

According to the model results, the ocean continues to take up radiocarbon throughout the entire of the simulation. Meaning it remains a sink until at least 2010. Although from 2009 to 2010 just 0.11 mol of radiocarbon, so about a thirtieth of the 1965 uptake, are taken up by the ocean. This means the ocean bomb inventory has reached a plateau. Continuing for some additional years the ocean, may or may not turn to a source for radiocarbon.

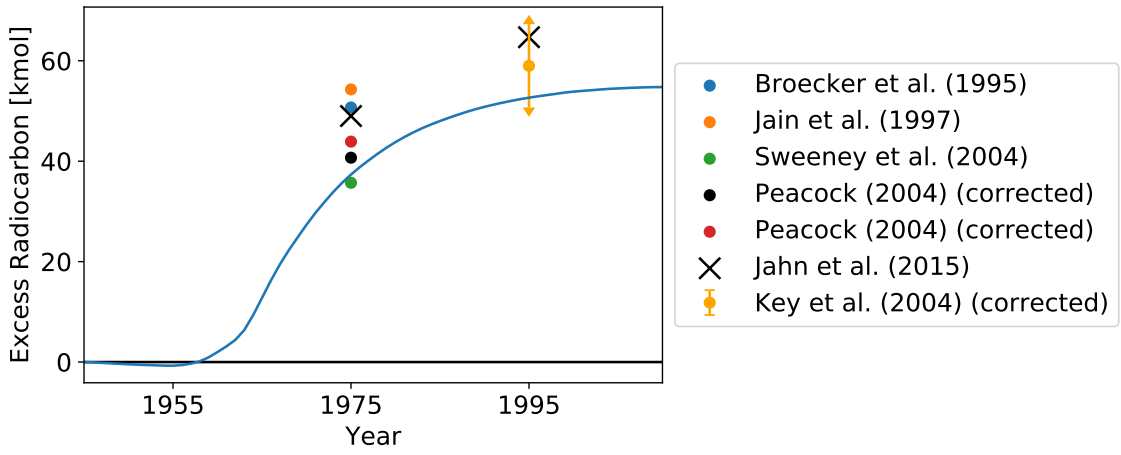

Figure 27: Blue line shows the industrial period simulation while the different colored dots represent estimates compiled by Naegler and Levin (2006). Not all estimates originally encompassed the entire ocean. Naegler and Levin (2006) corrected these estimates for the missing ocean sections.

To calculate the inventory of bomb radiocarbon (figure 27), we corrected for the model drift using the control simulation. To calculate the excess radiocarbon at any given time t the following formula is used.

$$^{14}\mathrm{I}_{bomb}(t) = \left(^{14}\mathrm{I}_{IND}(t) - ^{14}\mathrm{I}_{IND}(t = 1945)\right) - \left(^{14}\mathrm{I}_{CTRL}(t) - ^{14}\mathrm{I}_{CTRL}(t = 1945)\right) \tag{24}$$

^{14}I is the inventory of radiocarbon in the ocean at time t as simulated by the model. Superscripts IND and CTRL refer to the simulations IND_OC _and Ctrl _OC The correction by the trend, the last two terms in the equation, is relatively small, about -0.4 kmol.

Comparing our results with those of Jahn et al. (2015), provides insight into the effects of recent changes in CESM. Jahn et al. (2015) calculated an ocean bomb ^{14}C inventory of 49 kmol in 1975 and 64.7 kmol in 1995. Both of these values are at the high end of estimates. Jahn et al. (2015) suggested a too-high gas exchange rate caused this high bomb inventory.

We are not fully aware of all changes made to CESM since Jahn et al. (2015) implemented the carbon isotopes and calculate the bomb inventory. However, the gas exchange rate has been altered. The coefficient a used in equation 2 to calculate the gas transfer velocity, was changed from 0.31 cm h^{-1} (Wanninkhof (1992)) to 0.251 cm h^{-1} (Wanninkhof (2014). Such a considerably lower coefficient means much less uptake, which in turn, especially during the phase of high atmospheric Δ^{14}C, leads to a low bomb inventory. Note that already the old value was lower than what is recommended to use in the OMIP.

8.4 Control run

The control run and the spin-up differ in one major way: The climate series used the CORE2-NYF is used for the spinup(SPIN_OC). The climate data for the period 1958 to 1977 to the JRA55 data set is used to control run (CTRL_OC). This impacts the ocean circulation and therefore the distribution of certain tracers in the ocean. In figure 28, the depth profiles of DIC and $DI^{14}C$ for the control run, the spin-up and the industrial run are compared. The control and spin-up profile would even differ without any changes to the forcing conditions. The reason for this is that the control run continues the spin-up, which changes the results slightly due to the drift in the system.

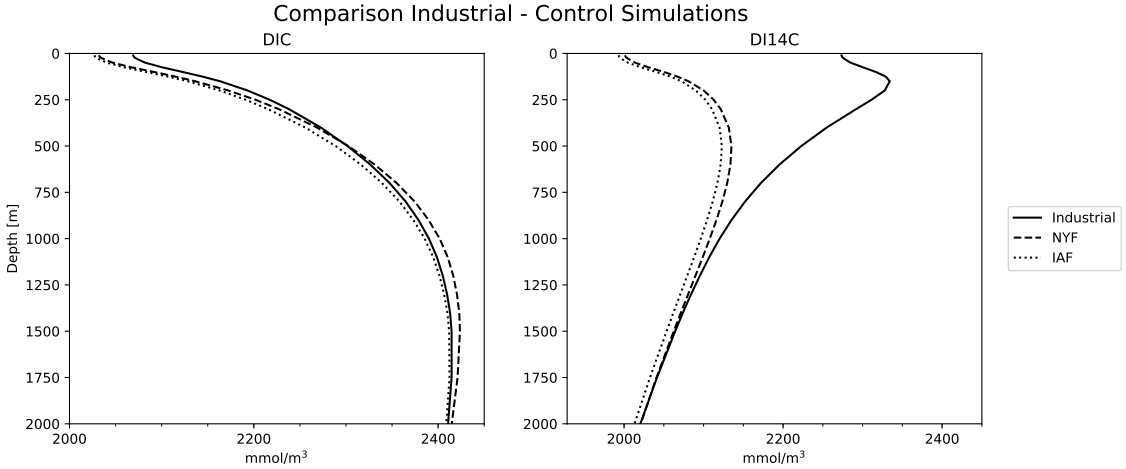

Figure 28: Comparison of results from the end of the spin-up (SPIN_OC,NYF, year 1350), the control simulation(CTRL_OC, IAF, year 1495) and the industrial period simulation (year 1995). Only the top 2000 m are shown.

Between 600 and 2000 m depth slightly higher DIC values are simulated at the end spin-up than both for the control simulation and the industrial period simulations. These differences are large enough that the total DIC content is less at the end of the industrial period simulation than the content at the end of the spin-up. This implies that the results from SPIN_OC should not be used as a reference to compute the ocean uptake and inventory of anthropogenic carbon. The amount of dissolved inorganic radiocarbon is consistently slightly higher in SPIN_OC with NYF than in CTRL_OC with JRA55. These differences are small compared to the $DI^{14}C$ changes in IND_OC that they play no role. The bomb radiocarbon inventory calculations are not affected by the $DI^{14}C$ differences between the control run and the spin-up. This is because all inventory calculations are done as differences between two points in the industrial period simulation.

These differences DIC + $DI^{14}C$ are very small when compared to the observation to model differences. We conclude that the results of this section are not impacted by the control to spin-up differences. However, anthropogenic carbon is highly affected by the choice of forcing. It might have been preferable to also run the spin-up with JRA forcing or to run all three runs with CORE2-NYF.

9 Land run analysis

In this section, the land runs are analysed. We are interested in how much radiocarbon is taken up by the land biosphere over the industrial period. We will start with a discussion of the drift in the spin-up system. Afterwards, the total uptake of carbon and radiocarbon is addressed, and we finish this section by discussing where this additional carbon and radiocarbon accumulates in the land.

9.1 Drift

Similarly to the ocean model, the land model is also expected to still drift at the end of the 750 year spin-up period. The drift needs to be taken into account for making a meaningful analysis of the land model results. To be able to take the trend into account, the control run CTRL_LN was performed.

Unlike the ocean only spin-up, which was forced by normal year forcing, so repeated forcing cycles of a single year, the land model was forced by a 20 yr forcing cycle. Most variables show a considerable dependence on this forcing cycles. Therefore, comparisons between two decadal averages, as was done for the ocean model, might not be ideal. If the decadal averages are placed differently within the 20-year forcing cycles, differences between the two might be related to the placement and not the trend of the model. Therefore, 20 year running means are calculated and evaluated. Figure 29 shows the evolution of the 20 year running mean of soil carbon and total ecosystem carbon, as well as soil Δ^{14}C and total ecosystem Δ^{14}C in CTRL_LN.

The trend in most carbon reservoirs on land is small. In the vegetation, the carbon content increases by 0.01% during the 200 year (figure 29). This means these variables are largely in equilibrium. Of larger concern is the trend in the soil carbon and radiocarbon. This signal dominates the total ecosystem trend, as can be seen in figure 29. The carbon content increases steadily by more than 0.1 PgC every 20 years, increasing by more than one PgC over the 200 years.

In Δ^{14}C the trend is large, about 10‰ in the soil organic carbon, and in the total ecosystem carbon, it is about 6 ‰. There is no noticeable slowdown in the soil carbon trend within the 200 years. This shows that the model is likely far away from equilibrium for the soil carbon.

The trends are far from uniform as can be seen in figure 30. Especially high northern latitudes show a large absolute change in both carbon and radiocarbon. In Δ^{14}C there are changes of multiple ‰ in large regions of the world. There are both regions of large positive and negative Δ^{14}C. High northern latitudes and the middle east show more than -10‰ change, while regions in southern Africa, south-east Asia and others show positive changes of up to 5‰.

We accept this as roughly in equilibrium for our purposes. There are multiple reasons, first of all, we expect the response to the bomb radiocarbon to be much bigger so that the trend is not that important. Second, we have a control simulation to at least partially deal with the trend. Third, the fact that the trend is showing no signs of slowing down means we would have to run for much longer to reach equilibrium. We do not have the computational resources to do so.

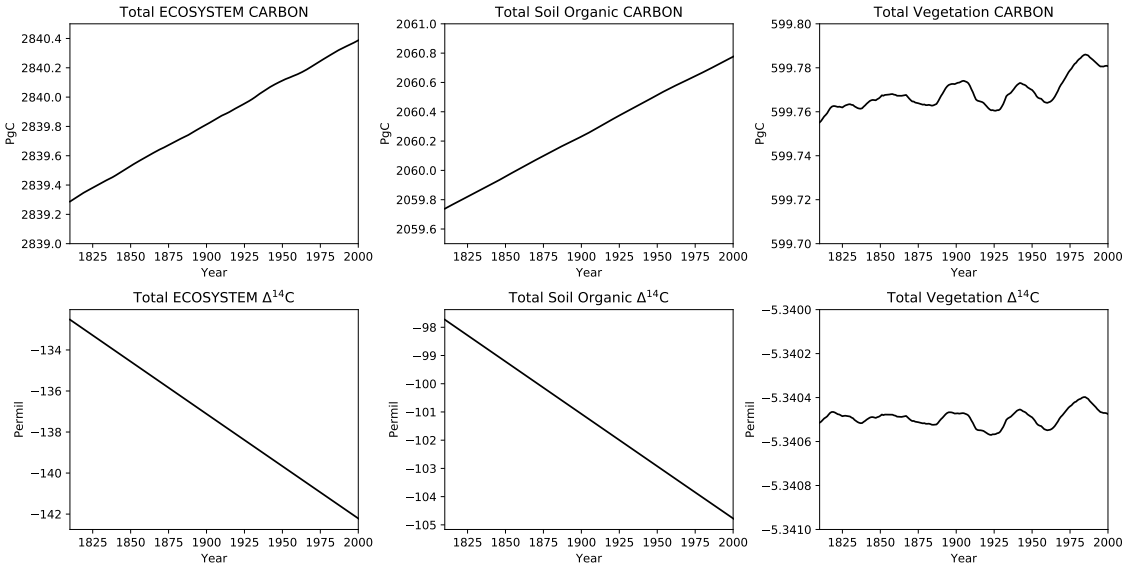

Figure 29: 20-year trend, for the end of the land spin-up and the control run. The year 1800 refers to the year 700 of the spin-up. By 1850 the control run starts. With help of the running mean, there is no visible dependence on the 20-year cycle.

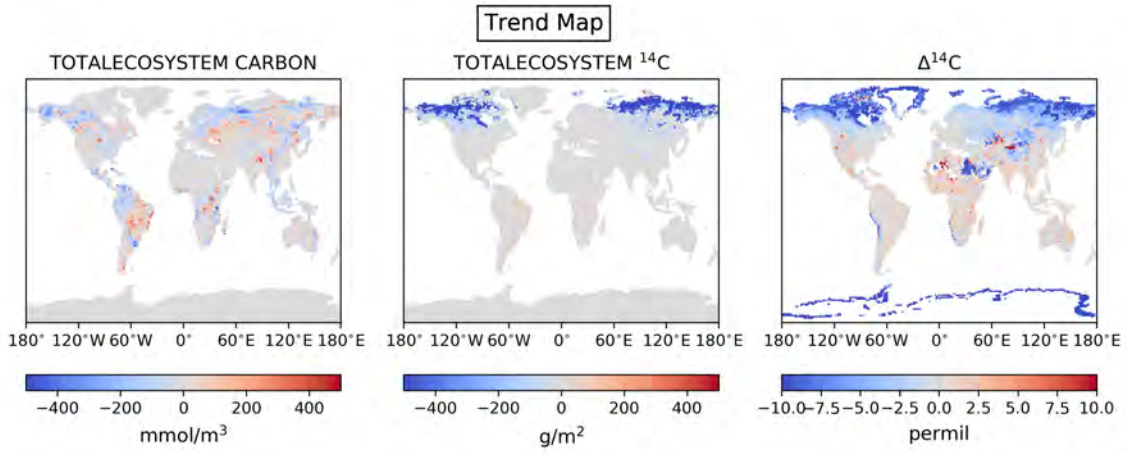

Figure 30: 100 year trend from the last 100 years of the control simulation. Presenting three variables TOTALECOSYSTEM CARBON,^{14}C, Δ^{14}C. TOTALECOSYSTEM ^{14}C simply adjusted by 10^{12}.

9.2 Bomb inventory

In figure 31 the total carbon and ^{14}C stored on land and the average Δ^{14}C are presented for both the control run and the historical simulation. A first observation is the clearly visible dependence of these variables on the twenty-year forcing cycles used. A second is a continuing trend seen in the control and spin-up simulations.

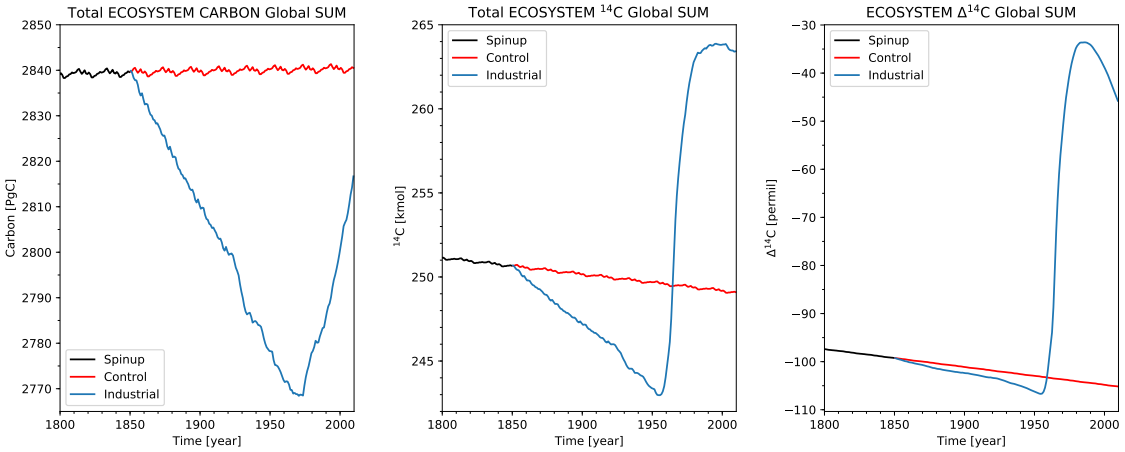

Figure 31: The year 1800 refers to the year 700 of the spin-up. By 1850 the control and industrial runs start. Industrial simulation results are trend corrected

All three variables, total carbon, total ^{14}C and total Δ^{14}C, experience a similar development during the industrial run, they start decreasing at the beginning of the simulation before starting to increase in the mid 20th century. However, there are key differences. Firstly the timing of the minima differs. For ^{14}C and Δ^{14}C the minima are reached in 1954 while for carbon content it is reached in 1966. Secondly, ^{14}C and Δ^{14}C reach a maxima in the 1990s and begin to drop afterwards. What is nicely visible in figure 31 is the influence of the 20 year forcing cycle on these variables. Especially in the total ecosystem carbon, an influence of a few PgC is visible.

The factors that contribute to the observed evolution of these variables are: land-use change, the Suess effect, increasing atmospheric CO_2, and nuclear bomb tests. In addition to these four effects the model shows a trend (red line figure 31). Land-use change affects the Δ^{14}C of the total land ecosystem, by typically removing or adding comparatively radiocarbon rich vegetation. Therefore, such actions change the composition of the land ecosystem and in turn effect Δ^{14}C.

The decrease in Δ^{14}C from 1850 to 1954 can be attributed to three effects: model trend, Suess effect and deforestation. While it is easily possible to separate the trend from the other two effects, separating the other two effects is not easily possible. All three effects combined to decrease the Δ^{14}C by 15‰ in the period from 1850 to 1954. 5‰ are caused by the trend. Total ecosystem carbon is unaffected by Suess effect and only slightly by the trend however deforestation causes a considerable loss of carbon. Between 1850 and 1966, the year of minimum total ecosystem carbon, a total of 70 PgC are lost from 2840 to 2770.

The relatively slow Δ^{14}C decrease from 1850 to 1954 is followed by a massive increase in the 30 years from 1954 to 1984. The bomb effect leads to an increase by Δ^{14}C from -108‰ to -34‰. During this time the Suess effect still impacts Δ^{14}C, however, compared to the bomb effect it is insignificant. Ecosystem carbon starts to increase in 1966 and continues to the end of the simulation. By 2010 the ecosystem carbon content has increased by 60 PgC, which means by the end of the simulation preindustrial carbon levels are not yet reached. Ecosystem carbon uptake during the time of very high atmospheric Δ^{14}C leads to additional acceleration of the land Δ^{14}C change.

In 1984, the highest land Δ^{14}C is reached. From -34‰ in 1984, land Δ^{14}C starts to decline, reaching -50‰ by 2010. The reason for this mostly stems from the reduced atmospheric Δ^{14}C. Newly taken up carbon is no longer as positive in Δ^{14}C as before. This even leads to the land turning from a radiocarbon sink to source. After 1994, the total ecosystem ^{14}C starts to slowly decrease. The reduction is very small with only 1.3 kmol in 16 years until the end of the simulation. However, it is large enough to clearly not be caused by the trend as according to the trend total ecosystem ^{14}C only decreases by 0.2kmol. The reason for this switch from a sink to a source is likely that the vegetation Δ^{14}C slower than in atmospheric Δ^{14}C.

9.3 Spatial distribution

In the last section, figure 31, four important points 1850, 1954, 1981 and 2014 in the evolution of the land Δ^{14}C can be identified: 1850 as the start, 1954 as the year of minimum radiocarbon,

1980 as the highest point in $\Delta^{14}C$ and 2010 as the end of the simulation. Figure 32 portrays the total carbon level in those specific years. 1850 is directly shown, while for the rest the difference to the previous date is presented. The trend, so the changes in the control simulation, have been subtracted. Figure 33 does the same for total carbon, except 1966 is presented instead of 1954 as this is the year of minimum carbon.

In the 1850 end of the spin-up starting point, neither radiocarbon nor $\Delta^{14}C$ are distributed uniformly. In $\Delta^{14}C$ especially the northern latitudes are highly negative with over -100‰, while tropical regions are close to zero. In carbon, the tropics and the northern high latitudes have high content, although the high northern latitudes have far higher content. The main difference between high northern latitudes and the tropics land carbon storage is where most carbon is stored, in the tropics it is in the vegetation, in the high northern latitudes it is in the soil.

The land-use change from 1850 to 1954 results in large changes in the carbon stock on the land. Certain regions in North and South America lose up to 10'000 gC/m^2. In light of a carbon stock of roughly 20'000 gC/m^2, 10'000 gC/m^2 is about half the total carbon stored. The $\Delta^{14}C$ drop is caused by both Suess effect and deforestation almost globally, except some small regions in the middle east and North America. The regions with limited or no deforestation show roughly a $\Delta^{14}C$ decrease of 5‰. Regions with large deforestation have 20‰ $\Delta^{14}C$ decrease, showing that deforestation leads to a $\Delta^{14}C$ decrease.

Within the relatively short span of 30 years between 1954 to 1984, $\Delta^{14}C$ changes drastically. Compared to 1954 $\Delta^{14}C$ is up to 100‰ higher in most regions of the world in 1984. This change affects all the same regions previously affected by the Suess effect. While there were both large regions with positive and negative $\Delta^{14}C$ change from 1850 to 1954, in the 1954 to 1984 period there are only positive regions. This shows how dominant the bomb effect is compared to the other effects. While the $\Delta^{14}C$ increase is massive and affects the whole globe, the increase in carbon content from 1966 to 1984 is more spatially different. Most regions gained carbon between 1966 and 1984, with some gaining up to 2000 g/m^2 in those 18 years. Regions with high losses between 1850 and 1966, such as North America and Europe gained, while other regions such as the southeastern South America continued to lose carbon.

From the highest land $\Delta^{14}C$ in 1984 to the end of the simulation in 2010 almost all regions depleted in ^{14}C. The spatial pattern of this decrease echos the pattern of the previous increase albeit much weaker in amplitude. From this, we can conclude that both likely had the same cause. This cause is the uptake of carbon from the atmosphere with a different $\Delta^{14}C$ signal than the vegetation already has. While the atmosphere was strongly enriched in $\Delta^{14}C$ from 1954 to 1984 compared to the land biosphere, it was slightly depleted between 1984 to 2010. The spatial pattern of the land carbon increase does remain roughly the same between 1984 and 2010 as it was between 1966 and 1984.

Across all four points in time, the high northern regions of Siberia and North America do not show changes. This is despite the fact that these regions contain the most amount of carbon/m^2 and are also the most negative in $\Delta^{14}C$. Although a slight increase in carbon content is visible. The reason is most likely that these regions have high soil carbon content but limited vegetation carbon. Vegetation is far quicker in reacting to outside changes.

Some singular cells show huge changes in either a positive or negative direction, not following their surrounding cells. While there are possible explanations such as this cell containing different plant functional types than its neighbouring cells, we do not think that these cells cause large global impacts. Since their impact is assumed to be small, we ignore them.

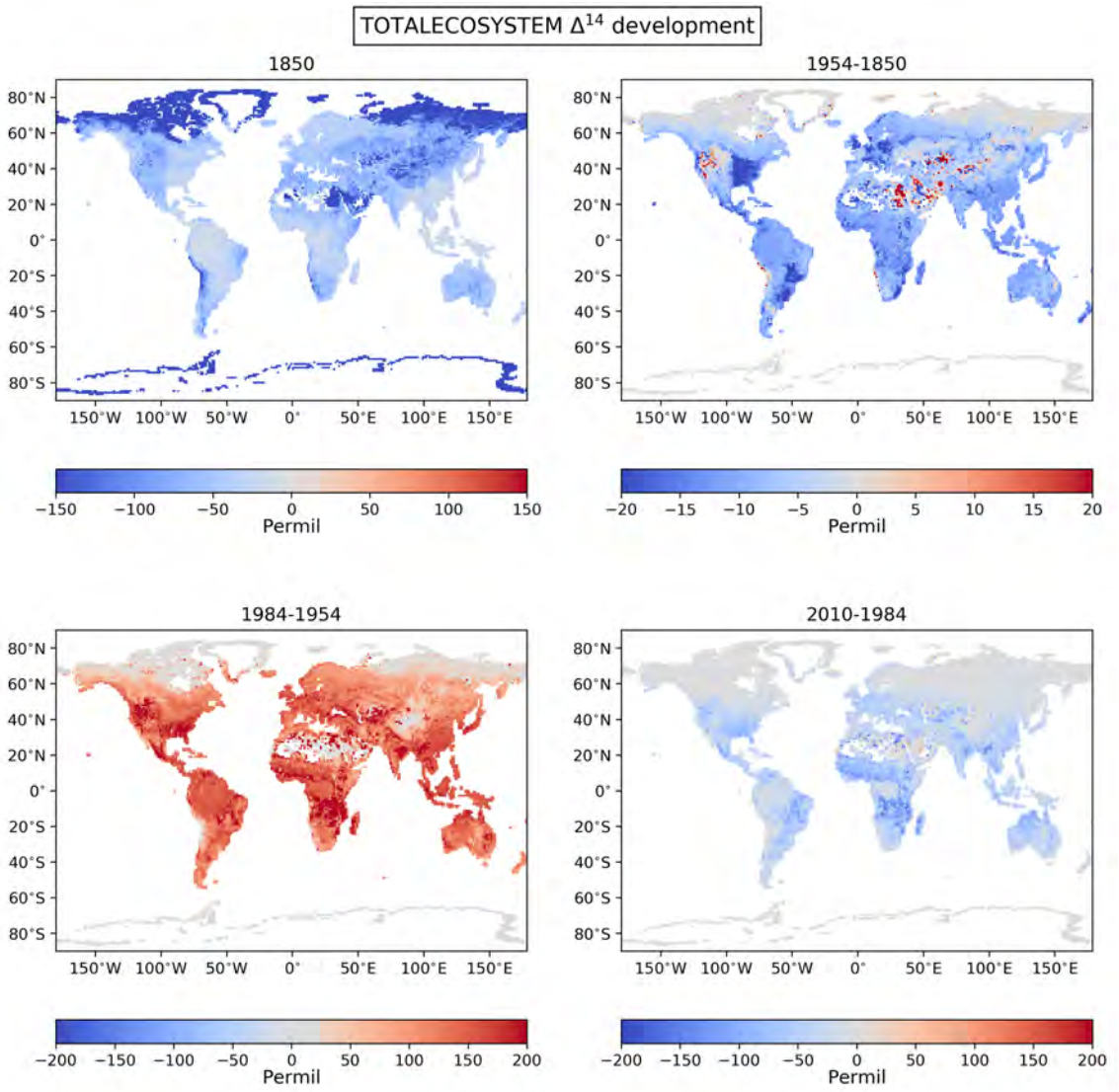

Figure 32: Evolution of Δ^{14}C in the land biosphere over the industrial period. Average Δ^{14}C of carbon stored in ecosystems as modelled for year 1850 (upper right) and changes in Δ^{14}C over the pre-bomb time (upper left), the time of the bomb peak (lower left) and recent decades (lower right). Note differences in color bars between panels.

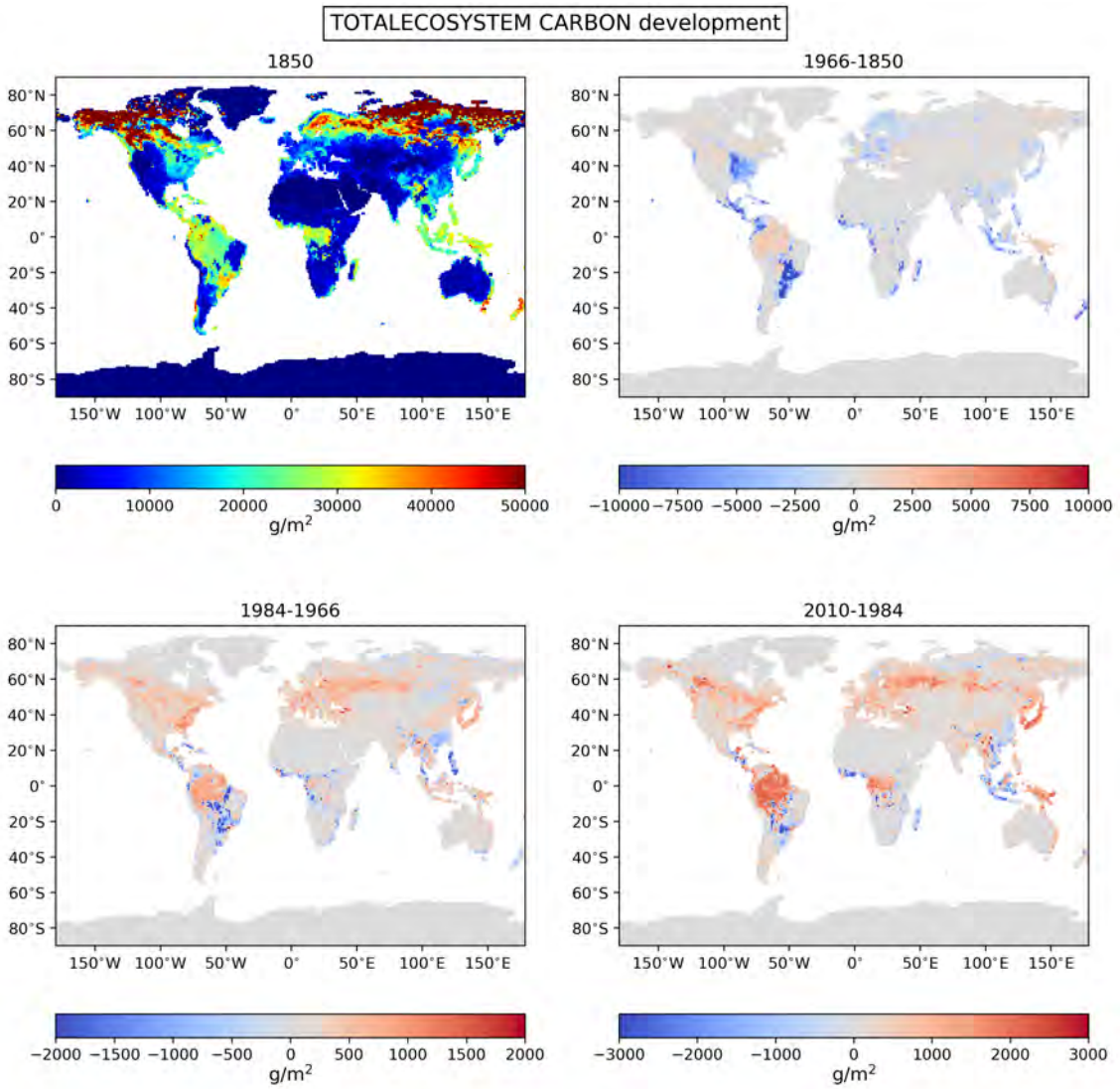

Figure 33: Evolution of total carbon in the land biosphere over the industrial period. Total carbon stored in ecosystems as modelled for year 1850 (upper right) and changes in $\Delta^{14}C$ over the pre-bomb time (upper left), the time of the bomb peak (lower left) and recent decades (lower right). Note differences in color bars between panels.

10 Total bomb budget

The total bomb budget as calculated with the results from the industrial period land and ocean transient simulations is shown in figure 34. The results sum the ocean inventory, land inventory from our model runs, and troposphere and stratosphere inventories extracted from Naegler and Levin (2009). The data from Naegler and Levin (2009) end in 2005. We extended them to 2010 by assuming they remain constant after 2005. They change little in the 2000s so this should not cause a large uncertainty. The results are compared to the results from the Naegler and Levin (2006) simulation, unlike previously where results were compared to observational estimates.

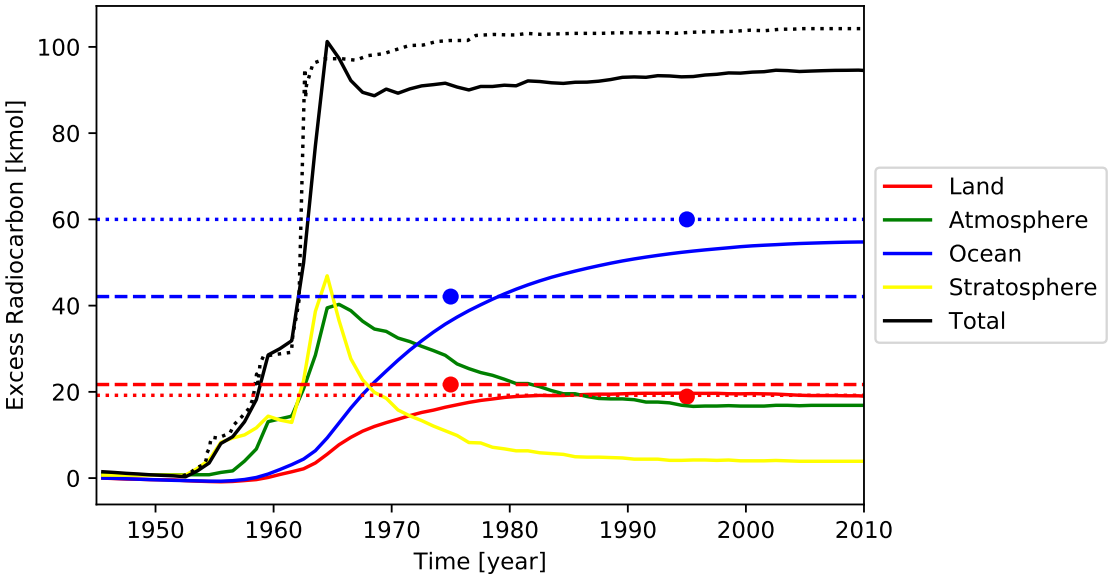

Figure 34: The bomb radiocarbon budget of the land model, ocean model and atmospheric data from Naegler and Levin (2009). For 1975 and 1995, the total (black line), land (red dots) and ocean ^{14}C (blue dots) bomb inventory estimated by Naegler and Levin (2006) are shown for comparison. Dashed and dotted red and blue lines extend the 1975 and 1995 Naegler and Levin (2006) inventories through time. Naegler and Levin (2009) results shown refer to their results in the case the YANG bomb set is used. The black dotted line represents the bomb produced ^{14}C according to Naegler and Levin (2009)

In general, it is clearly visible that all four reservoirs have taken up some of the extra carbon produced by the bomb tests. However, the distribution of the extra radiocarbon, and in our results even the exact amount of bomb radiocarbon changes throughout the years. In the first few years after 1945, land and ocean have negative bomb radiocarbon inventory, this is the result of the Suess effect. The bomb radiocarbon produced can be first found in stratosphere and troposphere. Shortly after the bomb tests, the stratosphere contains the most bomb radiocarbon. Afterwards, both of the troposphere and stratosphere quickly lose bomb radiocarbon while land and ocean take it up. By 1977, the ocean overtakes the troposphere as the reservoir containing the most bomb radiocarbon. In 2010, the ocean contains by far the most, followed by the land and the troposphere, which both contain roughly the same amount, the stratosphere contains the least.

In the following, we look at the four reservoirs in more detail. The ocean budget is not only consistently at the low end of observational estimates but also compared to the Naegler and Levin (2006) model results. 37.2 kmol versus 42.1 in 1975 and 52.7 kmol versus 60 kmol in 1995. We concluded that this is caused by the low air-sea gas exchange rate. One can also see that the ocean is still a sink for radiocarbon at the end of the simulation period. Note again that this estimate only includes DIC.

In the land biosphere, the CESM bomb budget increases slower than in the Naegler and Levin (2006) model. By 1975, the CESM model run has taken up 17 kmol compared to the 21.7kmol from Naegler and Levin (2006). Additionally, Naegler and Levin (2006) shows the radiocarbon content of 1995 on land to be lower than that of the year 1975. Meaning that at some point the land turned from a sink to a source. This switch is also visible in our results but does not lead to

the 1995 ^{14}C inventory being lower than the 1975 inventory. Even the 2010 inventory is still higher than in 1975. By 2010, our land estimated carbon levels are very close to the 1995 results from Naegler and Levin (2006). Meaning the land took up roughly 1/5 of the total bomb radiocarbon.

The troposphere bomb radiocarbon inventory shows a slightly different response as the tropospheric $\Delta^{14}C$, which we discussed in section 2. While tropospheric$\Delta^{14}C$ declines to roughly 0‰ after peaking at almost +800‰ in the north in 1968, the bomb radiocarbon inventory behaves differently. The bomb inventory in the troposphere increases from 0kmol in 1945 to 40 kmol in 1968, from the peak in 1968 the inventory decreases to 20 kmol in 2010. The reason the inventory does not decrease to 0 despite $\Delta^{14}C$ decreasing to 0‰ is that $\Delta^{14}C$ describes the ratio and the inventory describes the absolute amount of radiocarbon in the troposphere. While the ratio between ^{14}C and ^{12}C might be roughly the same in 2010 as it was in 1945, the amount of ^{12}C in the atmospheric is not. It increased by about 1/3. With more ^{12}C and the same $\Delta^{14}C$ this naturally means there is also more ^{14}C in the troposphere.

The stratosphere, according to Naegler and Levin (2009), takes up nearly as much radiocarbon as the troposphere in the 1960s, but by 2005 it only contains 5kmol. The spike in the stratosphere is both higher and declines faster than the one observed in the tropospheric inventory. More than half of the excess radiocarbon stored in the stratosphere in 1963 is distributed elsewhere by 1965. This means the stratosphere loses its bomb radiocarbon much faster than the troposphere. The reason for this is likely the comparatively small total carbon stored in the stratosphere.

The total bomb budget spikes in 1965 to over 100 kmol. A sharp drop to 90 kmol in 1968 is computed, followed by a slow increase during the rest of the simulated period. Our method of calculating the total bomb radiocarbon allows it to increase or decrease without sources or sinks in nature. The reason for this is that we simulate ocean and land separately with fixed atmospheric radiocarbon levels. The spike in total bomb radiocarbon in 1965 is expected as the result of the 60's bomb tests. However, there is no explanation as to why the total bomb radiocarbon should decrease afterwards. Radioactive decay is two small as only 0.6 kmol of these additional 100 kmol decay between 1965 and 2010. This leaves us with the conclusion that this is caused by the way we simulate the budget. A decrease means that the simulated reservoirs, land and ocean, take up less radiocarbon than the prescribed one's, atmosphere and stratosphere, lose. This finding fits with the previously discussed low radiocarbon content in 1975 in both the land and the ocean.

The slow increase of the total radiocarbon budget after the sharp drop means ocean and land take up more radiocarbon than the stratosphere and troposphere lose. One possible explanation is that due to the earlier slow uptake, the gradient between ocean and land remained larger than in for example the Naegler and Levin (2006) model. This would then lead to faster uptake, potentially 'too' fast uptake, leading to the creation of model radiocarbon out of nowhere. This creation of radiocarbon however does not balance out the sharp loss after the spike.

The total calculated by our approach is 95 kmol, which is lower than the 104 kmol estimated by Naegler and Levin (2009). These roughly 9 kmol difference stems primarily from the CESM ocean, which has taken up less than suggested by Naegler and Levin (2006). It is unlikely that the land should have taken up 9 additional kmol of radiocarbon given its current inventory. The low total oceanic bomb radiocarbon budget in combination with the too slow uptake leads us to believe that the piston velocity is too low.

The Naegler and Levin (2006) results are slightly dependent on the so-called bomb compilation used. These compilations include all nuclear bomb test and attribute to each of them an amount of radiocarbon produced. However, the dependence on these is small when compared to the difference, between our model and the Naegler and Levin (2009) results. Therefore, it is likely irrelevant to this comparison.

11 Conclusion

To recap, what was done, to find out how well the different carbon isotope implementations in the land and ocean components of CESM work, we ran several simulations with the model. Six simulations were performed, three for both the land and the ocean component. These three runs were: A spin-up to create initial conditions which are in equilibrium with preindustrial atmospheric forcing, an industrial period simulation in which the atmospheric forcing was changed to reflect the changes in the last 165 years and a control simulation, which ran the same length as the industrial period simulation but with spin-up atmospheric conditions. With the help of the results of these runs, we can now give answers to three questions posed in section 1.4.

How well can the CESM model represent the distribution of carbon isotopes at preindustrial? In section 7.2, I showed that the model results closely match the observed ^{14}C data in the surface ocean. However, the model predicts too low $\Delta^{14}C$ levels across nearly the entire subsurface ocean. The largest deviations between model and observational $\Delta^{14}C$ data are found in the deep Pacific, where differences exceeded 100‰. ^{13}C distributions also matched the observations relatively poorly. The model does relatively well represent the spatial $\Delta^{14}C$ patterns. So, in conclusion, the model does not capture the preindustrial carbon isotopes distribution especially well, but it gets the patterns well and observed $\Delta^{14}C$ values are quite nicely matched at the surface.

Can the CESM model faithfully represents the radiocarbon uptake by the ocean during the industrial period?. In section 8.2, I compare the model results against the same coral data as were used by Dentith et al. (2019). The model represents these measured coral profiles very well. This shows that the model can represent the different evolution in $\Delta^{14}C$ as recorded by these corals for the second half of the 20th century. However, the model slightly underestimated the amplitude of the atmospheric impact consistently across the different coral sampling locations. The comparison with the record from the Guam island in the Pacific revealed a further limitation of the modelling approach. With the current modelling approach, it is impossible to correctly simulate short term, regional impacts of the $\Delta^{14}C$ increase caused by individual nuclear bomb tests.

Can separately run ocean and land-only simulations be combined to reasonably represent the evolution of the total radiocarbon budget? In section 10, I discussed that the model ocean takes up less ^{14}C than suggested in other observational and model studies. Especially noticeable is how much less extra radiocarbon the model ocean takes up when compared to the results by Jahn et al. (2015), who used an earlier version of the same model. The major difference between the two model versions is the larger gas exchange coefficient used in the earlier version. From these results, I concluded that the model has a slightly too low gas exchange coefficient. This conclusion is also supported by the underestimation of the coral data.

Figure 34 suggests that, besides the fact that the ocean takes up too little radiocarbon, also the land is too slow in taking up radiocarbon, since in 1975 our results underestimate the results from Naegler and Levin (2006). This leads to the total radiocarbon budget, calculated as the sum of atmosphere + ocean + land inventory, not being constant after the bomb tests, it decreases first and then slowly increases afterwards. This means combining the two separate runs leads to an effect that had to be expected, the total ^{14}C in the system changes even without sources or sinks. That being said this effect was relatively small and the total budget reached at the end is close to that predicted by others. So combining the two separate runs to one total budget gives relatively good results.

From the three answers to these questions, we get the following outcome. The model is currently not too good in representing deep-sea distributions of isotopes, but that does not stop one from getting relatively good results for the industrial period. To improve the results it would probably make sense to slightly increase the gas exchange. Also, the way atmospheric $\Delta^{14}C$ input is handled has some limitations. Finally, the fact that separately run ocean and land models give good results shows that even without a fully-coupled carbon isotope model one can reach some conclusions about the radiocarbon distribution.

References

CLM Documentation, http://www.cesm.ucar.edu/models/cesm2/land/CLM50_Tech_Note.pdf.

Marbl Documentation, https://marbl.readthedocs.io/en/latest/sci-guide/index.html.

Andres, R. J., Marland, G., Boden, T., and Bischof, S.: Carbon Dioxide Emissions from Fossil Fuel Consumption and Cement Manufacture, 1751–1991, and an Estimate of Their Isotopic Composition and Latitudinal Distribution, p. 53–62, Cambridge University Press, https://doi.org/10.1017/CBO9780511573095.005, 2000.

Andrews, A. H., Asami, R., Iryu, Y., Kobayashi, D. R., and Camacho, F.: Bomb-produced radiocarbon in the western tropical Pacific Ocean: Guam coral reveals operation-specific signals from the Pacific Proving Grounds, Journal of Geophysical Research: Oceans, 121, 6351–6366, https://doi.org/10.1002/2016JC012043, URL https://agupubs.onlinelibrary.wiley.com/doi/abs/10.1002/2016JC012043, 2016.

Audi, G., Bersillon, O., Blachot, J., and Wapstra, A.: The NUBASE evaluation of nuclear and decay properties, Nuclear Physics A, 729, 3–128, https://doi.org/10.1016/j.nuclphysa.2003.11.001, 2003.

Broecker, W., Peng, T., Beng, Z., and Observatory, L.-D. G.: Tracers in the sea, Lamont-Doherty Geological Observatory, Columbia University, 1982.

Broecker, W. S., Sutherland, S., Smethie, W., Peng, T.-H., and Ostlund, G.: Oceanic radiocarbon: Separation of the natural and bomb components, Global Biogeochemical Cycles, 9, 263–288, https://doi.org/10.1029/95GB00208, URL https://agupubs.onlinelibrary.wiley.com/doi/abs/10.1029/95GB00208, 1995.

Broecker, W. S., Peacock, S. L., Walker, S., Weiss, R., Fahrbach, E., Schroeder, M., Mikolajewicz, U., Heinze, C., Key, R., Peng, T., and Rubin, S.: How much deep water is formed in the Southern Ocean?, Journal of Geophysical Research: Oceans, 103, 15 833–15 843, https://doi.org/10.1029/98JC00248, URL https://doi.org/10.1029/98JC00248, 1998.

Castagnoli, G. and Lal, D.: Solar Modulation Effects in Terrestrial Production of Carbon-14, Radiocarbon, 22, 133–158, https://doi.org/10.1017/S0033822200009413, 1980.

Choppin, G. R., LILJENZIN, J.-O., and RYDBERG, J.: CHAPTER 5 - Radionuclides in Nature, in: Radiochemistry and Nuclear Chemistry (Third Edition), edited by Choppin, G. R., LILJENZIN, J.-O., and RYDBERG, J., pp. 94 – 122, Butterworth-Heinemann, Woburn, third edition edn., https://doi.org/https://doi.org/10.1016/B978-075067463-8/50005-4, URL http://www.sciencedirect.com/science/article/pii/B9780750674638500054, 2002.

Ciais, P., Sabine, C., G. Bala, L. B., Brovkin, V., J. Canadell, A. C., DeFries, R., Galloway, J., Heimann, M., Jones, C., Quéré, C. L., Myneni, R., Piao, S., and Thornton, P.: Global Carbon Budget 2019, Climate Change 2013: The Physical Science Basis. Contribution of Working Group I to the Fifth Assessment Report of the Intergovernmental Panel on Climate Change [Stocker, T.F., D. Qin, G.-K. Plattner, M. Tignor, S.K. Allen, J. Boschung, A. Nauels, Y. Xia, V. Bex and P.M. Midgley (eds.)] Cambridge University Press, Cambridge, United Kingdom and New York, NY, USA, 2013.

Danabasoglu, G., Lamarque, J.-F., Bacmeister, J., Bailey, D. A., DuVivier, A. K., Edwards, J., Emmons, L. K., Fasullo, J., Garcia, R., Gettelman, A., Hannay, C., Holland, M. M., Large, W. G., Lauritzen, P. H., Lawrence, D. M., Lenaerts, J. T. M., Lindsay, K., Lipscomb, W. H., Mills, M. J., Neale, R., Oleson, K. W., Otto-Bliesner, B., Phillips, A. S., Sacks, W., Tilmes, S., van Kampenhout, L., Vertenstein, M., Bertini, A., Dennis, J., Deser, C., Fischer, C., Fox-Kemper, B., Kay, J. E., Kinnison, D., Kushner, P. J., Larson, V. E., Long, M. C., Mickelson, S., Moore, J. K., Nienhouse, E., Polvani, L., Rasch, P. J., and Strand, W. G.: The Community Earth System Model Version 2 (CESM2), Journal of Advances in Modeling Earth Systems, 12, e2019MS001916, https://doi.org/10.1029/2019MS001916, URL https://agupubs.onlinelibrary.wiley.com/doi/abs/10.1029/2019MS001916, e2019MS001916 2019MS001916, 2020.

Dauphas, N. and Schauble, E. A.: Mass Fractionation Laws, Mass-Independent Effects, and Isotopic Anomalies, Annual Review of Earth and Planetary Sciences, 44, 709–783, https://doi.org/10.1146/annurev-earth-060115-012157, URL https://doi.org/10.1146/annurev-earth-060115-012157, 2016.

Dentith, J. E., Ivanovic, R. F., Gregoire, L. J., Tindall, J. C., Robinson, L. F., and Valdes, P. J.: Simulating oceanic radiocarbon with the FAMOUS GCM: implications for its use as a proxy for ventilation and carbon uptake, Biogeosciences Discussions, 2019, 1–46, https://doi.org/10.5194/bg-2019-365, URL https://www.biogeosciences-discuss.net/bg-2019-365/, 2019.

Eide, M., Olsen, A., Ninnemann, U. S., and Johannessen, T.: A global ocean climatology of preindustrial and modern ocean δ13C, Global Biogeochemical Cycles, 31, 515–534, https://doi.org/10.1002/2016GB005473, URL https://agupubs.onlinelibrary.wiley.com/doi/abs/10.1002/2016GB005473, 2017.

Friedlingstein, P., Jones, M. W., O'Sullivan, M., Andrew, R. M., Hauck, J., Peters, G. P., Peters, W., Pongratz, J., Sitch, S., Le Quéré, C., Bakker, D. C. E., Canadell, J. G., Ciais, P., Jackson, R. B., Anthoni, P., Barbero, L., Bastos, A., Bastrikov, V., Becker, M., Bopp, L., Buitenhuis, E., Chandra, N., Chevallier, F., Chini, L. P., Currie, K. I., Feely, R. A., Gehlen, M., Gilfillan, D., Gkritzalis, T., Goll, D. S., Gruber, N., Gutekunst, S., Harris, I., Haverd, V., Houghton, R. A., Hurtt, G., Ilyina, T., Jain, A. K., Joetzjer, E., Kaplan, J. O., Kato, E., Klein Goldewijk, K., Korsbakken, J. I., Landschützer, P., Lauvset, S. K., Lefèvre, N., Lenton, A., Lienert, S., Lombardozzi, D., Marland, G., McGuire, P. C., Melton, J. R., Metzl, N., Munro, D. R., Nabel, J. E. M. S., Nakaoka, S.-I., Neill, C., Omar, A. M., Ono, T., Peregon, A., Pierrot, D., Poulter, B., Rehder, G., Resplandy, L., Robertson, E., Rödenbeck, C., Séférian, R., Schwinger, J., Smith, N., Tans, P. P., Tian, H., Tilbrook, B., Tubiello, F. N., van der Werf, G. R., Wiltshire, A. J., and Zaehle, S.: Global Carbon Budget 2019, Earth System Science Data, 11, 1783–1838, https://doi.org/10.5194/essd-11-1783-2019, URL https://www.earth-syst-sci-data.net/11/1783/2019/, 2019.

Garcia, H. E., Locarnini, R. A., Boyer, T. P., Antonov, J. I., Baranova, O. K., Zweng, M. M., Reagan, J., and Johnson, D. R.: World Ocean Atlas 2013. Vol. 4: Dissolved Inorganic Nutrients (phosphate, nitrate, silicate), S. Levitus, Ed.; A. Mishonov, Technical Ed. NOAA Atlas NESDIS, 76, 25, 2013.

Gloor, M., Gruber, N., Sarmiento, J., Sabine, C. L., Feely, R. A., and Rödenbeck, C.: A first estimate of present and preindustrial air-sea CO2 flux patterns based on ocean interior carbon measurements and models, Geophysical Research Letters, 30, 10–1–10–4, https://doi.org/10.1029/2002GL015594, URL https://agupubs.onlinelibrary.wiley.com/doi/abs/10.1029/2002GL015594, 2003.

Godwin, H.: Half-life of Radiocarbon, Nature, 195, https://doi.org/10.1038/195984a0, 1962.

Graven, H., Allison, C. E., Etheridge, D. M., Hammer, S., Keeling, R. F., Levin, I., Meijer, H. A. J., Rubino, M., Tans, P. P., Trudinger, C. M., Vaughn, B. H., and White, J. W. C.: Compiled records of carbon isotopes in atmospheric CO_2 for historical simulations in CMIP6, Geoscientific Model Development, 10, 4405–4417, https://doi.org/10.5194/gmd-10-4405-2017, URL https://www.geosci-model-dev.net/10/4405/2017/, 2017.

Hall, T. and Haine, T.: On Ocean Transport Diagnostics: The Idealized Age Tracer and the Age Spectrum, Journal of Physical Oceanography - J PHYS OCEANOGR, 32, 1987–1991, https://doi.org/10.1175/1520-0485(2002)032<1987:OOTDTI>2.0.CO;2, 2002.

Hayes, J.: An Introduction to Isotopic Calculations, At. Energy, 2004.

Jahn, A., Lindsay, K., Giraud, X., Gruber, N., Otto-Bliesner, B. L., Liu, Z., and Brady, E. C.: Carbon isotopes in the ocean model of the Community Earth System Model (CESM1), Geoscientific Model Development, 8, 2419–2434, https://doi.org/10.5194/gmd-8-2419-2015, URL https://www.geosci-model-dev.net/8/2419/2015/, 2015.

Keeling, C. D.: The Suess effect: 13Carbon-14Carbon interrelations, Environment International, 2, 229 – 300, https://doi.org/https://doi.org/10.1016/0160-4120(79)90005-9, URL http://www.sciencedirect.com/science/article/pii/0160412079900059, 1979.

Keller, K., Ois, F., and Morel, M.: A model of carbon isotopic fractionation and active carbon uptake in phytoplankton, Marine Ecology-progress Series - MAR ECOL-PROGR SER, 182, https://doi.org/10.3354/meps182295, 1999.

Kerbyson, D. and Jones, P.: A Performance Model of the Parallel Ocean Program, IJHPCA, 19, 261–276, https://doi.org/10.1177/1094342005056114, 2005.

Key, R. M., Kozyr, A., Sabine, C. L., Lee, K., Wanninkhof, R., Bullister, J. L., Feely, R. A., Millero, F. J., Mordy, C., and Peng, T.-H.: A global ocean carbon climatology: Results from Global Data Analysis Project (GLODAP), Global Biogeochemical Cycles, 18, https://doi.org/10.1029/2004GB002247, URL https://agupubs.onlinelibrary.wiley.com/doi/abs/10.1029/2004GB002247, 2004.

Kobayashi, S., Ota, Y., Harada, Y., Ebita, A., Moriya, M., Onoda, H., Onogi, K., Kamahori, H., Kobayashi, C., Endo, H., Miyaoka, K., and Takahashi, K.: The JRA-55 Reanalysis: General Specifications and Basic Characteristics, Journal of the Meteorological Society of Japan, 93, 5–48, https://doi.org/10.2151/jmsj.2015-001, 2015.

Lawrence, D. M., Hurtt, G. C., Arneth, A., Brovkin, V., Calvin, K. V., Jones, A. D., Jones, C. D., Lawrence, P. J., de Noblet-Ducoudré, N., Pongratz, J., Seneviratne, S. I., and Shevliakova, E.: The Land Use Model Intercomparison Project (LUMIP) contribution to CMIP6: rationale and experimental design, Geoscientific Model Development, 9, 2973–2998, https://doi.org/10.5194/gmd-9-2973-2016, URL https://www.geosci-model-dev.net/9/2973/2016/, 2016.

Laws, E. A., Popp, B. N., Bidigare, R. R., Kennicutt, M. C., and Macko, S. A.: Dependence of phytoplankton carbon isotopic composition on growth rate and [CO2)aq: Theoretical considerations and experimental results, Geochimica et Cosmochimica Acta, 59, 1131 – 1138, https://doi.org/https://doi.org/10.1016/0016-7037(95)00030-4, URL http://www.sciencedirect.com/science/article/pii/0016703795000304, 1995.

Liss, P. and Merlivat, L.: Air-sea gas exchange rates: Introduction and synthesis, The Role of Air-Sea Exchange in Geochemical Cycling, 1986.

Madec, G. and Imbard, M.: A global ocean mesh to overcome the North Pole singularity, Climate Dynamics, 12, 381–388, https://doi.org/10.1007/BF00211684, 1996.

Matsumoto, K.: Radiocarbon-based circulation age of the world oceans, Journal of Geophysical Research: Oceans, 112, https://doi.org/10.1029/2007JC004095, URL https://agupubs.onlinelibrary.wiley.com/doi/abs/10.1029/2007JC004095, 2007.

Meinshausen, M., Vogel, E., Nauels, A., Lorbacher, K., Meinshausen, N., Etheridge, D., Fraser, P., Montzka, S., Rayner, P., Trudinger, C., Krummel, P., Beyerle, U., Cannadell, J., Daniel, J., Enting, I., Law, R., Oapos;Doherty, S., Prinn, R., Reimann, S., and Weiss, R.: Historical greenhouse gas concentrations, Geoscientific Model Development Discussions, pp. 1–122, https://doi.org/10.5194/gmd-2016-169, 2016.

Melzer, E. and OLeary, M. H.: Anapleurotic CO2 Fixation by Phosphoenolpyruvate Carboxylase in C3 Plants, Plant Physiology, 84, 58–60, URL http://www.jstor.org/stable/4270577, 1987.

Murray, R. J.: Explicit Generation of Orthogonal Grids for Ocean Models, Journal of Computational Physics, 126, 251 – 273, https://doi.org/https://doi.org/10.1006/jcph.1996.0136, URL http://www.sciencedirect.com/science/article/pii/S0021999196901369, 1996.

Naegler, T. and Levin, I.: Closing the global radiocarbon budget 1945–2005, Journal of Geophysical Research: Atmospheres, 111, https://doi.org/10.1029/2005JD006758, URL https://agupubs.onlinelibrary.wiley.com/doi/abs/10.1029/2005JD006758, 2006.

Naegler, T. and Levin, I.: Observation-based global biospheric excess radiocarbon inventory 1963–2005, Journal of Geophysical Research: Atmospheres, 114, https://doi.org/10.1029/2008JD011100, URL https://agupubs.onlinelibrary.wiley.com/doi/abs/10.1029/2008JD011100, 2009.

Orr, J. C., Najjar, R. G., Aumont, O., Bopp, L., Bullister, J. L., Danabasoglu, G., Doney, S. C., Dunne, J. P., Dutay, J.-C., Graven, H., Griffies, S. M., John, J. G., Joos, F., Levin, I., Lindsay, K., Matear, R. J., McKinley, G. A., Mouchet, A., Oschlies, A., Romanou, A., Schlitzer, R., Tagliabue, A., Tanhua, T., and Yool, A.: Biogeochemical protocols and diagnostics for the CMIP6 Ocean Model Intercomparison Project (OMIP), Geoscientific Model Development, 10, 2169–2199, https://doi.org/10.5194/gmd-10-2169-2017, URL https://www.geosci-model-dev.net/10/2169/2017/, 2017.

Rubin, S. I. and Key, R. M.: Separating natural and bomb-produced radiocarbon in the ocean: The potential alkalinity method, Global Biogeochemical Cycles, 16, 52–1–52–19, https://doi.org/10.1029/2001GB001432, URL https://agupubs.onlinelibrary.wiley.com/doi/abs/10.1029/2001GB001432, 2002.

Sarmiento, J. L. and Gruber, N.: Ocean biogeochemical dynamics, Princeton University Press, 2006.

Schulte, P., van Geldern, R., Freitag, H., Karim, A., Négrel, P., Petelet-Giraud, E., Probst, A., Probst, J.-L., Telmer, K., Veizer, J., and Barth, J.: Applications of stable water and carbon isotopes in watershed research: Weathering, carbon cycling, and water balances, Earth-Science Reviews, 109, https://doi.org/10.1016/j.earscirev.2011.07.003, 2011.

Smith, R. and Gent, P.: Reference manual for the Parallel Ocean Program (POP), ocean component of the Community Climate System Model (CCSM2.0), Los Alamos National Laboratory Technical Report, 2002.

Stuiver, M. and Polach, H. A.: Discussion Reporting of 14C Data, Radiocarbon, 19, 355–363, https://doi.org/10.1017/S0033822200003672, 1977.

Suess, H.: Radiocarbon concentration in modern wood, Science, 3166, 415–417, 1955.

Tiwari, M., Singh, A. K., and Sinha, D. K.: Chapter 3 - Stable Isotopes: Tools for Understanding Past Climatic Conditions and Their Applications in Chemostratigraphy, in: Chemostratigraphy, edited by Ramkumar, M., pp. 65 – 92, Elsevier, Oxford, https://doi.org/https://doi.org/10.1016/B978-0-12-419968-2.00003-0, URL http://www.sciencedirect.com/science/article/pii/B9780124199682000030, 2015.

Wanninkhof, R.: Relationship between wind speed and gas exchange over the ocean, Journal of Geophysical Research: Oceans, 97, 7373–7382, https://doi.org/10.1029/92JC00188, URL https://agupubs.onlinelibrary.wiley.com/doi/abs/10.1029/92JC00188, 1992.

Wanninkhof, R.: Relationship between wind speed and gas exchange over the ocean revisited, Limnology and Oceanography: Methods, 12, 351–362, https://doi.org/10.4319/lom.2014.12.351, URL https://aslopubs.onlinelibrary.wiley.com/doi/abs/10.4319/lom.2014.12.351, 2014.

Yeager, S. and Large, W.: Diurnal to decadal global forcing for ocean and sea-ice models: The data sets and flux climatologies, NCAR Technical Note: NCAR/TN- 460+STR. CGD Division of the National Center for Atmospheric Research, 2004.

Zhang, J., Quay, P., and Wilbur, D.: Carbon isotope fractionation during gas-water exchange and dissolution of CO2, Geochimica et Cosmochimica Acta, 59, 107 – 114, https://doi.org/https://doi.org/10.1016/0016-7037(95)91550-D, URL http://www.sciencedirect.com/science/article/pii/001670379591550D, 1995.

Ziveri, P., Stoll, H., Probert, I., Klaas, C., Geisen, M., Ganssen, G., and Young, J.: Stable isotope 'vital effects' in coccolith calcite, Earth and Planetary Science Letters, 210, 137 – 149, https://doi.org/https://doi.org/10.1016/S0012-821X(03)00101-8, URL http://www.sciencedirect.com/science/article/pii/S0012821X03001018, 2003.

Declaration of consent

Text
on the basis of Article 30 of the RSL Phil.-nat. 18

Name/First Name: Frischknecht Tobias Rolf

Registration Number: 15-127-889

Study program: Master of Science in Climate Sciences with special qualification in Climate and Earth System Science

Bachelor ☐ Master ☑ Dissertation ☐

Title of the thesis: Radiocarbon in an Earth System Model (CESM 2)

Supervisor: Prof. Dr. Fortunat Joos

I declare herewith that this thesis is my own work and that I have not used any sources other than those stated. I have indicated the adoption of quotations as well as thoughts taken from other authors as such in the thesis. I am aware that the Senate pursuant to Article 36 paragraph 1 litera r of the University Act of 5 September, 1996 is authorized to revoke the title awarded on the basis of this thesis.
For the purposes of evaluation and verification of compliance with the declaration of originality and the regulations governing plagiarism, I hereby grant the University of Bern the right to process my personal data and to perform the acts of use this requires, in particular, to reproduce the written thesis and to store it permanently in a database, and to use said database, or to make said database available, to enable comparison with future theses submitted by others.

Laupen 4.8.2020

Place/Date

T. Frischknecht

Signature